

Investigation of Exotic Spin Textures in Chiral Magnetic Silicide Nanowires
for Spintronics Applications

By

John P. DeGrave

A dissertation submitted in partial fulfillment of
the requirements for the degree of

Doctor of Philosophy
(Chemistry)

at the

UNIVERSITY OF WISCONSIN-MADISON

2013

Date of final oral examination: 08/30/13

The dissertation is approved by the following members of the Final Oral Committee:

Song Jin, Associate Professor, Chemistry

Daniel C. Fredrickson, Assistant Professor, Chemistry

Trisha L. Andrew, Assistant Professor, Chemistry

Franz J. Himpsel, Professor, Physics

Paul G. Evans, Associate Professor, Materials Science and Engineering

Dane Morgan, Associate Professor, Materials Science and Engineering

Preface

Investigation of Exotic Spin Textures in Chiral Magnetic Silicide Nanowires

John P. DeGrave

The recent surge of interest in nanoscience and nanomaterials has helped push our understanding of the fundamental physical processes that are involved at the nanoscale versus those that dominate at much larger scales. The nanoscience revolution was sparked by the notion and general trends of computing science and information storage technology to push the length scales to smaller and smaller values to achieve high density devices. Many sub-fields of nanomaterials synthesis have developed around the desire to reduce the dimensions of semiconductor and other technologically relevant materials with applications ranging from thermoelectrics, solar energy conversion, optoelectronics, and spintronics among others. However, reducing the physical dimensions of the system is no longer about “miniaturizing” the physical components of a well-known system to compress it into a smaller package, but is now largely motivated by observations of fundamentally new phenomena that occur at the nanometer length scale.

Many physical processes have an associated fundamental length scale, consider the quantum mechanical phenomena of tunneling. It can be shown that an electron that impinges upon an energy barrier has a finite probability to penetrate physically into the energy barrier, and if the energy barrier has a small enough physical dimensions the electron can pass completely through the barrier to the other side. The analogy at the macroscopic scale would be kicking a soccer ball at a brick wall with great force then suddenly finding that soccer ball had not bounced back at the

kicker, but had suddenly passed through to the other side of the brick wall, completely in-tact. For an electron, this tunneling process can occur with a fairly high probability when the physical dimensions of the insulating barrier are typically on the order of a few nanometers or less. In fact, this type of process is what dominates the fundamental operating mechanism of the so called magnetic tunnel junction which is the primary operating component of modern scanning disk hard-drives.

Such interesting quantum mechanical phenomena are prevalent at the nanoscale, and have driven the continued interest in the synthesis of new materials at these length scales. One such morphology of nanomaterial that has shown interesting possibilities is the nanowire. A nanowire is characterized by a diameter or width of less than about 500 nm (although many would put this limit below 100 nm there are certain systems in which the characteristic length scale approaches 100 nm or more, and therefore, the 500 nm limit is still considered “nano”), any larger than this and the fundamental characteristics of the material do not differ significantly than what would be observed for a bulk material. The typical length of a nanowire can vary from as small as 1 micron up to tens or hundreds of microns.

We shall be primarily concerned with understanding how several different chiral magnetic materials can be affected by reducing the size of the system to the nanoscale, and specifically by using the nanowire morphology. In order to develop the understanding of nano-confinement, we have developed several new characterization techniques for nanowires that include superconducting heterostructures to measure spin polarization electrically, a new Hall effect measurement method to electrically detect magnetic domains, and electron microscopy to image magnetic domains in real-space. The focus will be on $\text{Fe}_{1-x}\text{Co}_x\text{Si}$ and MnSi nanowires, and in

these materials the magnetic domains take on characteristic length scales ranging from 18 nm up to 75 nm. Therefore, even nanowires on the larger end of what is considered “nanoscale” can be used to observe and understand the effects of geometrical confinement on these nanoscale magnetic domains.

The introduction (Chapter 1) provides a common set of language and concepts that will be used throughout the remaining chapters, and focuses on understanding the formation of chiral magnetic domains and what is so far known about the dynamics of a particular domain configuration known as a “skyrmion.” Chapter 2 will begin the investigation of silicide nanowires by introducing a complete characterization of $\text{Fe}_{1-x}\text{Co}_x\text{Si}$ nanowires, which belong to the class of chiral magnetic compounds. Several specialized spectroscopic techniques will be introduced that have been used to demonstrate that this nanomaterial is homogeneously doped and that the magnetism originates from the Co atoms. Furthermore, the technique of Andreev reflection spectroscopy will be demonstrated for nanowires so that the spin polarization of the material can be extracted. The spin polarization of conduction electrons has several important implications for the magnitude of the topological Hall effect that will be re-visited and explored in-depth in the final chapter.

Chapter 3 will then turn to the first real-space observations of magnetic domains in MnSi nanowires. This nanoscopic investigation began with a collaboration initiated by this author’s three month trip to Japan in the summer of 2011 under a jointly funded National Science Foundation (NSF) and Japanese Society for the Promotion of Science (JSPS) where I was able to undertake collaborative research efforts at RIKEN (Wako, Japan), National Institute for Materials Science (Tsukuba, Japan), and the University of Tokyo (Tokyo, Japan). During this initial research period we developed the techniques and foundational ideas for properly

observing magnetic domains in nanowire materials. The work was then completed by Japanese researchers after I returned to the United States to continue work on electrical measurements. These observations by Lorentz microscopy have provided the definitive evidence of the magnetic domain structure in MnSi nanowires and have helped to guide the electrical and magnetotransport studies carried out in the remaining two chapters.

Chapter 4 turns to the development and successful implementation of a new Hall effect measurement methodology for the nanowire morphology. This chapter includes work on two different materials, namely, FeS₂ nanostructures and MnSi nanowires. The slight detour away from chiral magnetic materials to FeS₂ was motivated by the desire to demonstrate the effectiveness of the Hall measurement methodology on a classical semiconductor material in a well-known regime so that the measurement method could then be extended to nanowires of chiral magnetic materials with confidence. This chapter also provides the first evidence that we can successfully make Hall effect measurements on MnSi nanowires which provides the foundation of the electrical transport measurement provided in Chapter 5.

Finally, Chapter 5 provides the first electrical measurements of MnSi nanowires that definitively identify the transport signature of magnetic skyrmion domains. It is shown that the orientation of the nanowire with respect to the external magnetic field can have a significant impact on the magnetotransport properties. We also provide preliminary insights regarding the emergent electrodynamics associated with translating skyrmion domains which is the most relevant regime for future implementations of these magnetic domains in spintronics devices.

-JPD, August 21, 2013

Acknowledgements

The pursuit of a PhD has always been about seeking out some fundamental truth in this world. Too often we are confronted by deception and misdirection in modern times. The work I have performed over the past 5 years across the fields of chemistry, materials science, and physics may have, at times, seemed difficult and trying, but it has truly been a luxury and a privilege to search out the True in this world. I would not have been able to embark on, nor complete this journey if it were not for the numerous individuals who have helped to encourage and motivate me in the darkest of times and have been there to congratulate me at the peaks and milestones. For this reason, I should very much like to thank the following group of people who make up the totality of my Ph.D.

My parents Sue and Paul DeGrave have always been there to support and lift me up. They never questioned my pursuit, and have always encouraged me wholeheartedly no matter what fork in the road I happened down whether or not they really understood what I was working on (only to my own fault). A son could truly never ask for greater loving support. My brother, Robert, and sister, Karen, have been staples throughout my life and sources of life lessons. They have taught me how to compete, how to be grateful, and how to truly be thankful for family. Here, I would also like to thank two dear personal friends and companions, Alison Schweda and Lucille Schweda, who have kept me grounded in the real world and who have provided me with far too generous praise throughout my life's pursuits.

Next I would like to thank those who have helped me get to this point in my academic career. I suppose my interest and love of science really took hold in my junior and senior years of high school education at Green Bay Southwest High School. Who knew that chemistry could turn acoustic, before I met Mr. Abbott and his fine tune “Phase Change? Of course I should not forget Mr. Nedobek who woke up early mornings to help us eager and scientifically inclined students study for the advanced placement physics courses that would later inspire me to study solid state physics and spin based electronics. With this solid fundamental knowledge in chemistry and physics, I went on to major in chemistry at my undergraduate *alma mater* Hillsdale College. My adviser, Dr. Cynthia Woodbridge, who I worked with on a computational project, constantly encouraged me and saw in me an ability to pursue the pinnacle of academic degree and ultimately saw to it that I had the phenomenal opportunity to attend the nuclear chemistry summer school at Brookhaven National Laboratory. She then supported me and strongly encouraged my decision to attend graduate school at the University of Wisconsin-Madison. I should also mention, that it was ultimately my undergraduate research on the molecule cobaltocene, guided by Dr. Cynthia Woodbridge that led me into the field of spintronics where I sought out the energetic and passionate adviser to my Ph.D. research, Professor Song Jin.

Prof. Song Jin has been an endless source of encouragement and wisdom for this academic research pursuit. He has pushed me and set high goals that have made my Ph.D. research something I will always look back on with great pride. I should also like to thank the numerous other faculty at the University of Wisconsin-Madison who have served on my committees, who have offered their teaching and mentoring experience, and who have provided advice to help me

throughout this journey. Song Jin was also the initiator of collaboration with Japanese researchers who ultimately took me in for a summer and helped me push this Ph.D. thesis towards completion. I would like to specifically thank Prof. Yoshinori Tokura, Prof. Naoto Nagaosa, Prof. Yoshinori Onose who acted as advisors for my research efforts in Japan, and Dr. Xiuzhen Yu and Masashi Kubota who worked with me on daily basis to complete research efforts.

I would also like to thank those personal friends of mine who have put up with grumpy days and who have been there to take me out for a drink (or two) when times were rough. Especially, Audrey Forticaux, Ankit Pokrhel, Michelle Benson, Katie Whittaker, Ken Barnes, Mark Lukowski, as well as those elder graduate students who taught me how to enjoy graduate student life and ultimately how to be a successful researcher such as Jeremy Higgins, Andrew Schmitt, Steven Morin, and Matthew Bierman. I unfortunately do not have the space to thank everyone by name that I have come across in my graduate career, but there are many others who have given me amazing memories that I shall look back fondly on, especially some of the bright young students in the Jin group.

Table of Contents

<i>Preface</i>	i
<i>Acknowledgements</i>	v
<i>Table of Contents</i>	viii
<i>List of Tables</i>	ix
<i>List of Figures</i>	x
<i>Chapter 1: Introduction to Chiral Magnetism and Exotic Spin Textures for Future Spintronics Applications</i>	1
<i>Chapter 2: Spin Polarization Measurement of Homogeneously Doped Fe_{1-x}Co_xSi Nanowires by Andreev Reflection Spectroscopy</i>	43
<i>Chapter 3: Observation of the Magnetic Skyrmion Lattice in a MnSi Nanowire by Lorentz TEM</i>	66
<i>Chapter 4: A General Method to Measure the Hall Effect in Nanowires: Examples of FeS₂ and MnSi</i>	84
<i>Chapter 5: Topological Hall Effect from Skyrmion Domains in MnSi Nanowires at Large Current Densities</i>	106
<i>Appendix 1: Supporting information for Chapter 2</i>	133
<i>Appendix 2: Supporting Information for Chapter 4</i>	143
<i>Appendix 3: Supporting Information for Chapter 5</i>	156

List of Tables

<i>Table 4.1</i>	<i>Morphology and measured dimensions, calculated Hall coefficient (R_H), resistivity (ρ_{xx}) and Hall mobility (μ_H) at 295 K for ten FeS₂ Hall Devices</i>	
		96

List of Figures

Figure 1.1 <i>Magnetic domain configurations of B20 chiral magnets</i>	3
Figure 1.2 <i>Magnetic racetrack memory concept for nanowires</i>	6
Figure 1.3 <i>Calculated phase diagrams using mean-field approaches</i>	10
Figure 1.4 <i>Experimentally observed phase diagrams for chiral magnets</i>	13
Figure 1.5 <i>LTEM imaging and phase analysis</i>	16
Figure 1.6 <i>Experimental LTEM observation of thin slab of MnSi nanowire</i>	19
Figure 1.7 <i>Electron-skyrmion interactions</i>	22
Figure 1.8 <i>Schematic band diagram of Andreev reflection process</i>	26
Figure 1.9 <i>Current-driven motion of helimagnetic and skyrmion domains by simulation</i>	29
Figure 1.10 <i>Homebuilt chemical vapor deposition (CVD) setup for nanowire synthesis</i>	34
Figure 2.1 <i>SEM and EDS analyses of typical $Fe_{1-x}Co_xSi$ nanowires</i>	47
Figure 2.2 <i>Atom probe tomography (APT) experiments of $Fe_{1-x}Co_xSi$ nanowires</i>	50
Figure 2.3 <i>X-ray magnetic circular dichroism (XMCD) of $Fe_{1-x}Co_xSi$ nanowires</i>	53
Figure 2.4 <i>Andreev reflection spectroscopy of $Fe_{1-x}Co_xSi$ nanowires</i>	56
Figure 3.1 <i>MnSi NW sample thinned by SEM-FIB</i>	71
Figure 3.2 <i>Spontaneous magnetic configuration of thinned MnSi NW observed using LTEM</i>	73
Figure 3.3 <i>Magnetic configurations of MnSi NW in a normal magnetic field of 210 mT</i>	76
Figure 3.4 <i>Magnetic field versus temperature phase diagrams for various MnSi morphologies</i>	78
Figure 4.1 <i>Fabrication of Hall effect devices using NWs</i>	89

Figure 4.2 Measurement and extraction of the Hall voltage for an FeS ₂ device	93
Figure 4.3 A scattered plot of calculated Hall coefficient (R_H) versus Hall mobility (μ_H) at 295 K for 23 Hall devices of FeS ₂ NWs, nanorods, and nanoplates	97
Figure 4.4 Hall resistivity (ρ_{xy}) versus applied magnetic field at several temperatures for a MnSi NW Hall device	100
Figure 5.1 Extraction of the topological Hall effect voltage (V_{THE}) with external magnetic field perpendicular to the electrical current	113
Figure 5.2 Topological Hall resistivity of two MnSi NW devices	117
Figure 5.3 Comparison of the magnitude of topological Hall resistivities in two MnSi nanowire devices and with bulk MnSi	121
Figure 5.4 Symmetric magnetoresistance and topological Hall effect of MnSi NW Device 2 with the applied magnetic field preferentially applied parallel to the long axis of the NW (26° misalignment)	125
Figure A1.1 Schematic AC lock-in measurement setup and typical data for Fe _{1-x} Co _x Si NW	137
Figure A1.2 Additional Andreev reflection measurement data sets fit with BTK model	139
Figure A1.3 Andreev reflection signal at various temperatures for a Fe _{1-x} Co _x Si nanowire device not successfully fit with BTK model, and resistance versus temperature data	141
Figure A2.1 FeS ₂ nanowire hall devices without the insulating Al ₂ O ₃ layer.	146
Figure A2.2 Cylindrical nanowire Hall device example	148
Figure A2.3 Additional data plots for 23 FeS ₂ Hall devices showing the (lack of) correlation of Hall coefficient and Hall mobility	150

Figure A2.4 <i>Hall resistivity versus applied magnetic field at several temperatures for a MnSi NW Hall device with a rhombohedra cross-section measuring 420 nm</i>	152
Figure A2.5 <i>Reported Hall resistivity for bulk MnSi versus applied magnetic field</i>	154
Figure A3.1 <i>Effects of various values of applied DC current in MnSi NW devices</i>	158
Figure A3.2 <i>Topological Hall resistivity extracted for MnSi NW Device 3 at $T = 26.0$ K</i>	160

CHAPTER 1

Introduction to Chiral Magnetism and Exotic Spin Textures for Future Spintronics Applications

1.1 An Overview of Chiral Magnetism and Skyrmion Magnetic Domains

When thinking about non-magnetic versus magnetic materials there are generally two competing interactions that govern the observed magnetic behavior, namely dipole interactions that tend to anti-align electron spins and direct-exchange interactions that tend to align electron spins parallel to each other. Non-magnetic materials such as copper, silver, and gold are dominated by dipole interactions leading to so called diamagnetism whereby all the electron spins are paired and there is no net magnetic moment. Ferromagnetic materials such as iron, nickel and cobalt have magnetic properties that result from the dominating direct-exchange interactions that align unpaired electron spins along a single direction across a large spatial region that we call a magnetic domain, and this produces a net magnetic moment in the material. Chiral magnets are closely related to these strictly ferromagnetic materials with the exception that their crystal structures lack a center of inversion symmetry which introduces an additional energetic term known as the Dzyaloshinskii-Moriya (DM) interaction.¹⁻³ The ferromagnetic exchange interactions cause the spins to align nearly parallel over very short distances (a single unit cell of the crystal lattice), however, over many unit cells of the crystal lattice, the spins smoothly rotate with respect to each other to produce incommensurate spin configurations. The DM interaction can result in a wide array of exotic spin configurations depending on the precise

details of the crystal lattice,⁴ but a great deal of recent interest has been focused on materials having the B20 crystal structure including the metals MnSi,⁵⁻⁹ Fe_{1-x}Co_xSi,¹⁰⁻¹⁵ FeGe,^{16, 17} MnGe,¹⁸⁻²⁰ and the multiferroic insulator that shares the same P2₁3 space group as the B20 materials, Cu₂OSeO₃.²¹⁻²⁵

The ground magnetic state of the B20 chiral magnets, below the critical ordering temperature, is a helix of spins (Figure 1.1a) in which the spin direction in successive crystallographic planes smoothly rotates by a small angle, so that over a short distance the ordering looks to be ferromagnetic, but forms a helix over many unit cells of the crystal lattice. Governed by weak crystallographic anisotropy, the helix propagates along a preferred crystallographic direction, characterized by the q-vector (\vec{q}) and is observed to be the [111] direction for MnSi and [110] direction for Fe_{1-x}Co_xSi.^{9, 14} Furthermore, if a small magnetic field is applied along \vec{q} the spins will cant along the magnetic field direction to form a conical spin configuration (Figure 1.1b). If, however, the magnetic field is applied perpendicular to \vec{q} , the spins configure into skyrmion magnetic domains (Figure 1.1c). The skyrmion is most simply imagined as a vortex of spins, but is topologically non-trivial in the sense that the peripheral spins of the skyrmion configuration are aligned with the external magnetic field, but the central spin is anti-aligned. Skyrmion size varies based upon the strengths of the ferromagnetic exchange interaction and the DM interaction, typically having dimensions of a few nanometers in MnGe¹⁸ up to nearly one hundred nanometers in FeGe.^{16, 17, 26}

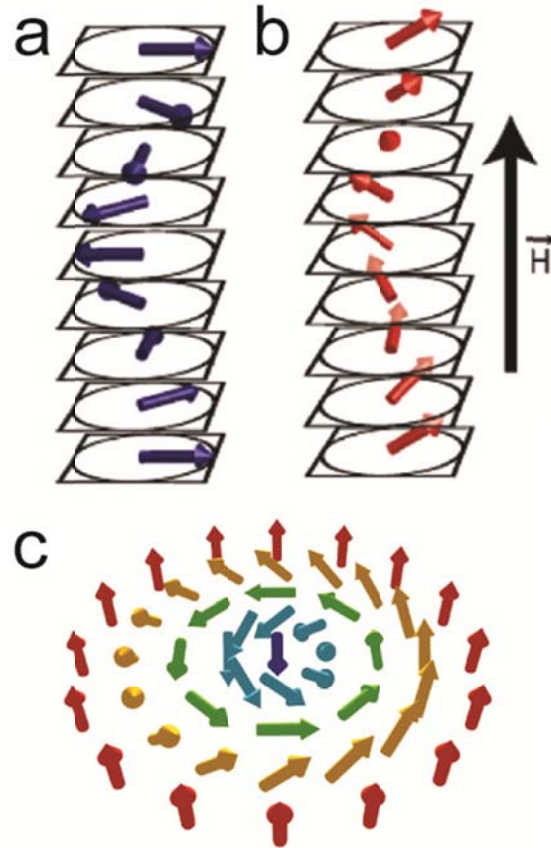


Figure 1.1 Magnetic domain configurations of B20 chiral magnets. a) The magnetic ground state spin configuration termed a spin helix or helical domain, b) under the effects of a 0magnetic field applied along the helimagnetic direction a conical magnet is formed, and c) shows the skyrmion magnetic domain spin configuration when the magnetic field is applied perpendicular to the helical propagation direction.

The magnetic ordering we now call a skyrmion was a concept originally developed by Tony Skyrme in the field of nuclear physics to describe the formation of baryons as stable localized particle-like excitations in a continuous field.²⁷ Theoretical solid state physicists later adopted this idea from nuclear physics when they realized that this concept could be properly extended to describe stable spin configurations in a continuous crystal field with chiral interactions. These mean-field calculations performed by Bogdanov and collaborators showed that skyrmion magnetic domains could form in solid state materials where the chiral spin-orbit coupling term (Dzyaloshinskii-Moriya interaction) exists from symmetry considerations.^{1, 3, 28-30} Furthermore, by invoking an additional phenomenological term in the magnetic free energy that describes some generic anisotropic energy they were later able to show that the skyrmion magnetic state could be stabilized in the absence of a magnetic field.^{31, 32} It should be noted that a theoretical debate is still ongoing about the validity of this phenomenological term, and whether or not it creates some unnecessary complications in the theoretical understanding of the skyrmion magnetic phase formation. Rosch et al. have instead suggested that including Gaussian thermal fluctuations in the mean-field model calculations is sufficient to stabilize the skyrmion crystal formation over the conical state when approaching T_c .^{9, 33} Both theories have been successfully used to describe experimental results in varying regimes of morphology and effective forces, such as crystal strain.

1.2 Potential Applications for Skyrmion Magnetic Domains

Furthermore, the skyrmion magnetic domain has captured the interest of the spintronics and quantum computing communities for their anticipated applications in next generation non-volatile computing technology.³⁴⁻³⁷ One such device that has been the subject of a great deal of

academic and industrial interest is the so-called magnetic “racetrack” memory that was an idea originally introduced by Parkin et al. from IBM.³⁸ Conceptually, magnetic domain walls are generated using Oersted fields from current pulses and patterned into a magnetic material that makes up the “racetrack.” Spin polarized current pulses then push the magnetic domains along the racetrack via the spin-transfer torque mechanism until they reach a magnetic domain sensing element which could take the form of a magnetic tunnel junction (as shown in Figure 1.2).³⁹ This memory concept can be utilized to pattern a high density of information that can be accessed quickly with smaller power consumption compared to current technologies such as FLASH and HDD.^{34, 38} So far the vast majority of research on these magnetic racetrack memory concepts has been on nanowire (NW) systems that are ferromagnetic at room-temperature such as permalloy.^{34, 40} The magnetic domain walls in these ferromagnetic systems pin very strongly to defects and often require current densities in excess of 10^{10} A/m² to manipulate the domain-walls which causes excessive Joule heating, ultimately leading to device failure.⁴¹ The skyrmion magnetic domains, however, have been demonstrably manipulated at much lower current densities, typically on the order of 10^5 - 10^6 A/m² which avoids the problems of Joule heating, but the highest temperature observations of skyrmion magnetic domains in such systems is limited to roughly 260 K.^{16, 17, 36, 42-44}

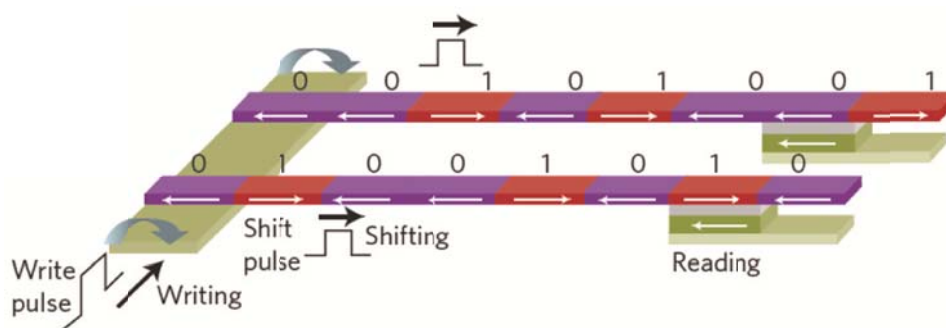


Figure 1.2 A schematic drawing of the racetrack memory concept. A write pulse is used to control the creation and orientation of the magnetic domain in the nanowire (NW) racetrack. A shift pulse is applied along the direction of the racetrack to translate the magnetic domains through the spin-transfer torque mechanism. The magnetic domain walls are then read using a magnetic tunneling junction device.⁴⁵ Adapted by permission from Macmillan Publishers Ltd: Nature Materials Ref. 45, © 2012.

Although we have so far focused on skyrmions that appear in the B20 chiral magnets, brief mention should also be made about tangential developments of these topologically stable spin configurations recently observed in very thin films of ferromagnetic materials such as a monolayer of Fe on Ir(111).⁴⁶ Since the skyrmion domains in these systems are the smallest yet observed (1-2 nm) it has been suggested that very high density information could be stored in the central spin of the skyrmion domain configuration. In fact, simple mathematical operations have been demonstrated by manipulating magnetically coupled spin spirals in self-assembled Fe atom chains on Ir(001),⁴⁷ and researchers have also demonstrated the controlled creation and annihilation of skyrmion domains by spin-polarized current injection using a spin-polarized scanning tunneling microscope (SP-STM) tip.⁴⁸ Although the creation and control of skyrmions in B20 materials has been proposed theoretically, it has not yet been demonstrated experimentally.^{49, 50} Therefore, these atomically thin metal systems offer another potential implementation of skyrmion magnetic domains in magnetic storage applications.

These first indications of the remarkable qualities of skyrmion magnetic domains show that there is a great deal of promise for such chiral magnetic materials in the future of magnetic information storage and quantum computing. Before these applications can be realized several questions still persist about the skyrmion magnetic phase: (1) How do these topologically non-trivial domains arise from the precursor magnetic states? (2) What happens as the size of the system is reduced to the dimension of a few or a single skyrmion domain? (3) Can we effectively control and manipulate the skyrmion domains so that we can utilize them in actual computing applications? Below I will outline the current theoretical and experimental work that constitutes the major body of work governing our knowledge about these magnetic domains, and

how the work within this doctoral thesis furthers that understanding towards the development of nanoscale spintronics devices.

1.3 Theoretical Understanding of Magnetic Skyrmion Domain Formation

The magnetic free energy density for a chiral magnetic system can be written

$$w = J/2(\nabla \cdot \vec{M})^2 - \vec{M} \cdot H + \alpha \vec{M} \cdot (\nabla \times \vec{M}) + U\vec{M}^4 - KM_z^2 \quad (1.1)$$

where the first term represents ferromagnetic exchange and $J/2$ is the exchange stiffness, the second term is the Zeeman energy with external magnetic field H , the third term is the chiral Dzyaloshinskii-Moriya (DM) interaction characterized by the constant α , U is the cubic anisotropy, and the last term characterizes generic uniaxial distortions with the constant K .^{32, 51} The ground magnetic state of such a system is characterized by a spin helix with period $q_0 = D/J$. If we neglect the anisotropy term, we can write the magnetization of such a crystal system as

$$\vec{M}(r) \approx M_f + \sum_{i=1}^3 \vec{M}_{\vec{q}_i}^h(\vec{r} + \Delta\vec{r}_i) \quad (1.2)$$

where $\vec{M}_{\vec{q}_i}^h(\vec{r}) = A[\vec{n}_{i1} \cos(\vec{q}_i \vec{r}) + \vec{n}_{i2} \sin(\vec{q}_i \vec{r})]$ is the magnetization of single chiral helix having amplitude A and wave-vector \vec{q} , and the two unit vectors \vec{n}_{i1} and \vec{n}_{i2} are orthogonal to both \vec{q} and each other. Moreover, under the effects of an intermediate magnetic field the conical state is energetically favored. The insight here is that the skyrmion magnetic phase results from the superposition of three helices, however it exists only as a metastable phase since the \vec{q} -vectors prefer to lie parallel to the external magnetic field.⁹ Next, we will briefly address the two competing models that attempt to explain how the skyrmion magnetic phase becomes

energetically favored over the conical state.^{9, 32} Both competing models seem to properly reproduce the magnetic phase diagrams of the chiral B20 magnets, but they provide slightly different insights into possible stabilization mechanisms for the skyrmion phase over the conical phase.

The first theoretical model we consider makes use of the phenomenological uniaxial anisotropy parameter (KM_z^2) which should become important in systems characterized by a significant amount of strain.³² Examples of such systems might include thin films grown by molecular beam epitaxy (MBE) on lattice mismatched growth substrates, or intrinsically strained systems caused by the nanoscale dimensions of a material and larger surface area to volume ratio, such as the case of a NW. Figure 1.3a shows the phase diagram calculated by including the uniaxial anisotropy term³² (plotted as K/K_0) and is able to reproduce the major experimentally observed features of the chiral magnetic phase diagram of the B20 materials. Namely, the helicoid is the global ground state in the absence of an applied magnetic field (purple shading in Figure 1.3a), the conical phase is then favored for small applied magnetic fields and zero uniaxial anisotropy (green shading), the skyrmion lattice is energetically favored for intermediate magnetic fields and when there is non-zero uniaxial anisotropy in the system (yellow shading), and finally the region of isolated skyrmions is characterized by large applied magnetic fields or large uniaxial anisotropy (blue shading). Interestingly, this calculated phase diagram suggests that *if a system has a large enough uniaxial anisotropy, isolated skyrmions should be the ground magnetic state of the system, and a one-dimensional NW system may approach this high uniaxial anisotropy limit when the dimensions of the NW are sufficiently small compared to the skyrmion domain size.*

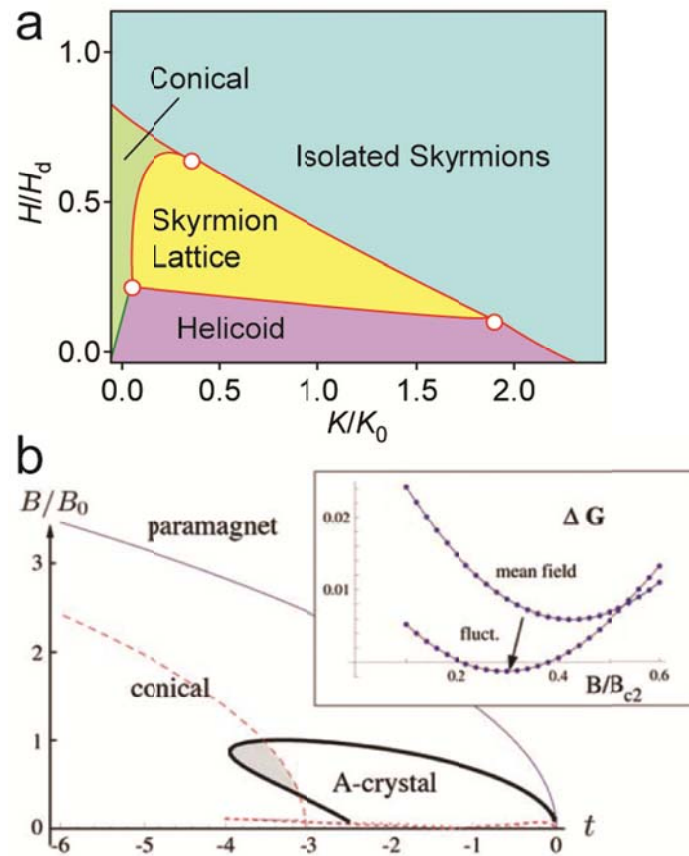


Figure 1.3. Calculated phase diagrams using mean-field approaches. a) Phase diagram of the reduced magnetic field (H/H_d) versus the reduced anisotropy (K/K_0) adopted from Butenko et al.³² b) Phase diagram of reduced magnetic field (B/B_0) versus temperature ($t \sim [T - T_c]$) calculated by Muhlbauer et al.⁹ for MnSi with the phenomenological uniaxial anisotropy term omitted, but instead including thermal fluctuations. The inset shows a plot of the free energy difference between the skyrmion phase and the conical phase, and demonstrates that if fluctuations are included in the calculations, the skyrmion phase becomes energetically favored. From Muhlbauer, S.; et al. *Science* **2009**, 323, 915-919. Reprinted with permission from AAAS.

In the second theoretical model, the phenomenological uniaxial anisotropy parameter is not used. Instead, thermal fluctuations are included in the calculation of the magnetic free energy to produce the phase diagram shown in Figure 1.3b.⁹ The effect of including thermal fluctuations in the mean-field calculations are shown in the inset of Figure 1.3b which plots the energy difference between the skyrmion and conical phases as a function of magnetic field, and it is clear that the skyrmion phase is not just a metastable phase, but becomes energetically favored by the inclusion of these thermal fluctuations. This model accurately reproduces the magnetic phase diagram for a bulk crystal of MnSi, and has been used to correctly identify the first order phase transition from the high temperature paramagnetic state into the helimagnetic phase as a Brazovskii transition, putting to rest some speculation about precursor “liquid skyrmion” phases.³³ One additional insight is that the helimagnetic and conical phases are destabilized simply by confining the helimagnetic vector to a dimension smaller than its wavelength which then causes the skyrmion phase to become energetically favored (as opposed to introducing an energetic uniaxial distortion in the previous model). With these two models of skyrmion magnetic domain formation established, we will next take a look at the experimental exploration of these spin configurations.

1.4 Observations of Exotic Spin Textures

1.4.1 Small Angle Neutron Scattering Experiments

The monosilicide MnSi is perhaps the most well studied of the chiral magnetic compounds. A large body of work was developed in understanding the origins of magnetism and electrical behavior of this compound due to its well-behaved classical itinerant electron ferromagnetism.⁶ In these early studies, the magnetic phase diagram was explored extensively and an anomalous

magnetic phase transition was identified between the conical to field polarized ferromagnetic phases in a small temperature window around 29.5 K and under small applied magnetic fields (Figure 1.4a).^{52, 53} The yet unexplained pocket in the magnetic phase diagram was termed the A-phase, and the first indications that it might be the skyrmion magnetic domain was through reciprocal space mapping via small-angle neutron scattering (SANS) experiments that revealed a remarkable six-fold diffraction pattern (Figure 1.4a inset) when the applied magnetic field was oriented along the incident neutron beam.⁹ It was hypothesized that the six-fold diffraction pattern was the result of the hexagonal packing of skyrmion magnetic domains, or alternatively viewed as the superposition of three helices along the three energetically equivalent crystallographic directions each giving rise to a Bragg diffraction spot at $+\bar{q}$ and $-\bar{q}$.⁹

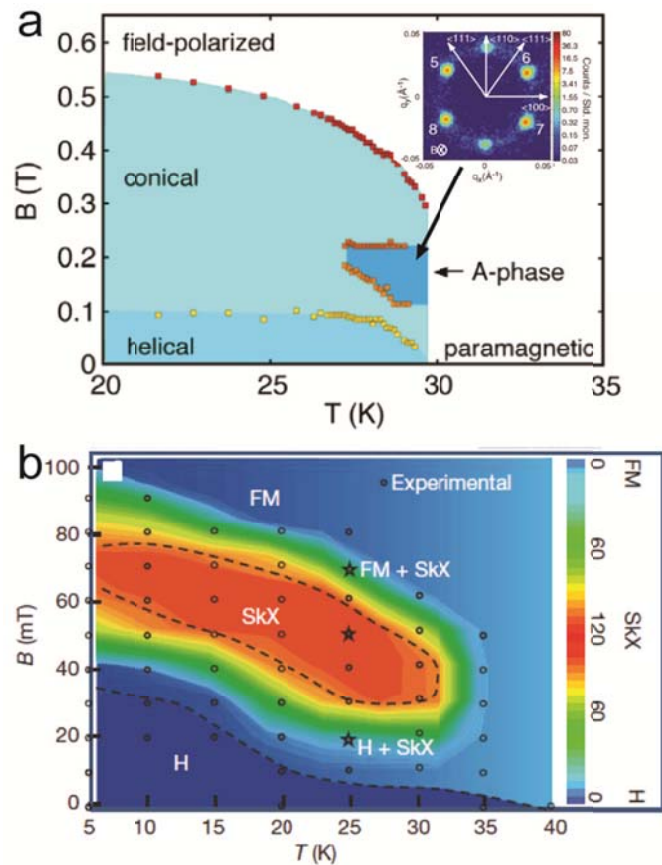


Figure 1.4. Experimentally observed magnetic field versus temperature phase diagrams for chiral magnets. a) Phase diagram derived from magnetic susceptibility measurements and SANS experiments on bulk crystals of MnSi, From Muhlbauer, S.; et al. *Science* **2009**, 323, 915-919. Reprinted with permission from AAAS. Inset shows the characteristic six-fold diffraction pattern of the triple- \vec{q} structure associated with the skyrmion phase. b) External magnetic field versus temperature phase diagram obtained for a $\text{Fe}_{1-x}\text{Co}_x\text{Si}$ ($x = 0.5$) thin film observed by LTEM.¹² Adapted by permission from Macmillan Publishers Ltd: Nature Ref. 12, © 2010.

Since the initial observation of skyrmion lines in MnSi by SANS,⁹ these scattering experiments have been further extended to other materials with the B20 crystal structure including alloys of the monosilicides such as $\text{Mn}_{1-x}\text{Fe}_x\text{Si}$,¹⁴ $\text{Mn}_{1-x}\text{Co}_x\text{Si}$,¹⁴ $\text{Fe}_{1-x}\text{Co}_x\text{Si}$,¹⁴ and the germanium analogues MnGe ^{19, 20} and FeGe ,²⁶ and most recently, the multiferroic insulator Cu_2OSeO_3 ⁵⁴ that also shares the B20 crystal structure. SANS experiments have provided excellent experimental evidence for the existence of the skyrmion magnetic phase as a general phenomenon for B20 crystal structures, but the most convincing evidence that has so far been provided is through Lorentz transmission electron microscopy (LTEM) observations.

1.4.2 Lorentz Transmission Electron Microscopy of Chiral Magnetic Thin Films

While SANS allows us to see the magnetic structure through the lens of reciprocal space, Lorentz transmission electron microscopy (LTEM) provides a way to image the magnetic domain structure of these chiral magnets in real-space, and therefore, the first truly definitive evidence for the existence of the skyrmion magnetic domains. State-of-the-art Lorentz microscopes can resolve magnetic domains on the order of 20 nm, and therefore can provide information about magnetic defects as well as the transition dynamics between magnetic phases.^{16, 55} Differing from a typical TEM, a Lorentz microscope has an additional set of magnetic lenses that are activated when the microscope is operated in “Lorentz mode.” This allows the objective lens to be turned off which removes the large magnetic field that would typically saturate the sample. Instead, the objective lens is used to controllably apply a magnetic field by adjusting the applied current. Since the sample in LTEM is not magnetically saturated by the strong magnetic field of the objective lens, the magnetic domain structure of the sample causes the deflection of the incident electron beam through the usual Lorentz force ($q\vec{v} \times \vec{B}$).

Experimentally, over-focused and under-focused images are obtained (with equivalent defocusing lengths) and contrast that is magnetic in origin will be observed to go from bright contrast to dark contrast in the two images. The in-plane magnetic component can be calculated using the magnetic transport-of-intensity equation (implemented with the QPt image analysis software),^{56, 57}

$$\frac{2\pi}{\lambda} \frac{\partial I(xyz)}{\partial z} = \nabla_{xy} [I(xyz) \nabla_{xy} \phi(xyz)] \quad (1.3)$$

where $I(xyz)$ and $\phi(xyz)$ are the intensity and phase of a propagating optical wave, and then recognizing that the phase can be related to the magnetization (\vec{M})

$$\nabla_{xy} \phi(xyz) = -\frac{e}{\hbar} (\vec{M} \times \vec{n}) t \quad (1.4)$$

where t is the thickness of the sample under observation, and \vec{n} is the unit vector perpendicular to the thin film sample. Finally, the change in intensity between the over and under-focused images provides $\partial I / \partial z$, and $\phi(xyz)$ can then be calculated and related back to the in-plane magnetization direction (an example of the resulting colorized image is shown in Figure 1.5a).

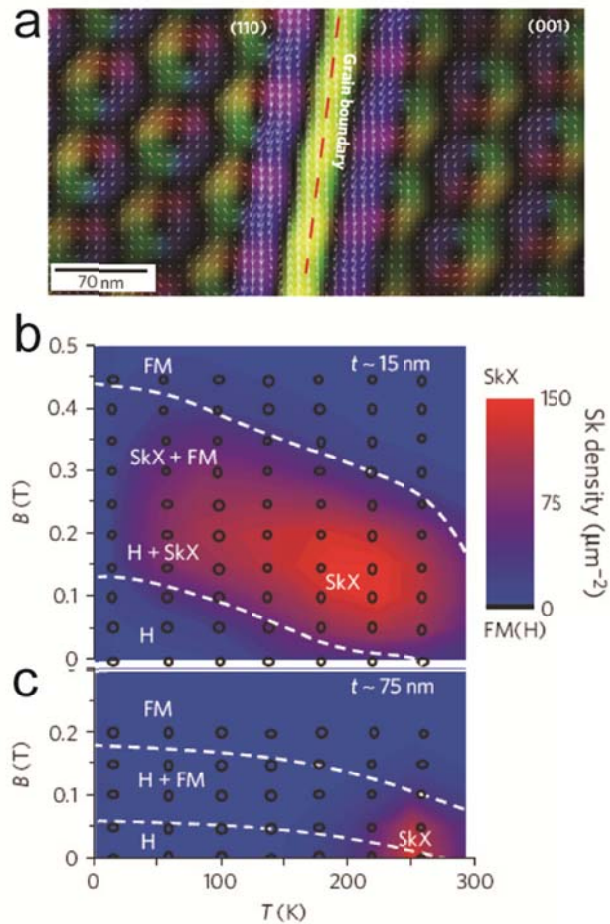


Figure 1.5. LTEM imaging and phase analysis.¹⁶ a) Colorized LTEM image showing the in-plane magnetic component of a FeGe thin film obtained using the transport-of-intensity equation analysis when in the skyrmion lattice phase ($B = 0.1$ T; $T = 260$ K). b,c) Phase diagrams inferred from LTEM observations of an FeGe thin film having a helical wavelength of roughly 70 nm, and with thin film thickness of 15 nm (b) and 75 nm (c). Black dots indicate the temperature and magnetic field of actual observations, and the white dotted lines show the estimated magnetic phase boundaries. Adapted by permission from Macmillan Publishers Ltd: Nature Materials Ref. 16, © 2011.

This LTEM technique was first used to image skyrmion magnetic domains in a thin film of $\text{Fe}_{0.5}\text{Co}_{0.5}\text{Si}$,¹² and has provided further evidence for skyrmion magnetic domains in thin films of MnSi ,^{58, 59} FeGe ,^{16, 42} Cu_2OSeO_3 ,²³ and most recently in a thinned slab of MnSi NW.⁶⁰ Not only has LTEM been able to provide definitive evidence of skyrmion magnetic domains for the first time, but it has also provided several general insights regarding the chirality of the skyrmion domain in relation to the underlying crystal lattice, and most importantly, the stabilization of the skyrmion magnetic phase over the conical phase in thin-film samples and 1D nanostructures. In LTEM experiments, the magnetic field is aligned perpendicular to the 2D thin film which suppresses the conical phase and favors the skyrmion magnetic phase. Figure 1.5b,c show the magnetic phase diagram obtained from LTEM observations of a FeGe thin film with thickness of 75 nm and 15 nm, respectively. Clearly, the skyrmion phase appears over a much wider magnetic field-temperature window in the thinner film due to the stronger suppression of the conical phase by the physical dimensions. *Such experimental evidence provides a strong motivation to extend these observations to the NW morphology which can be considered to be confined in two dimensions.* Most recently, the skyrmion phase was observed in a MnSi NW that was shaped into a thin slab using a focused-ion beam (a non-trivial sample preparation method, shown in Figure 1.6a) and the skyrmion phase was observed between 6 K and 35 K (as shown in Figures 1.6b,c) which is a much larger temperature window than the skyrmion lattice phase in bulk MnSi (27- 29.5 K, c.f. Figure 1.4a) and will be further discussed in Chapter 3. However, the small size of NWs presents major obstacles for observations by both LTEM and SANS which can be summarized as follows: (1) the small dimensions of NW samples make observation by SANS nearly impossible due to the weak signal levels from such a small crystal and the random orientations associated with the large ensemble of bottom up synthesized NWs,

and (2) LTEM observations will be complicated by the cross-section geometry of NWs namely, a circular cross-section will create obstructive Fresnel fringes which is further elaborated on in Chapter 3. Therefore, we must seek an alternative experimental probe which lies in the electrical transport signatures of skyrmion magnetic domains that will be discussed further in Chapters 4 and 5.

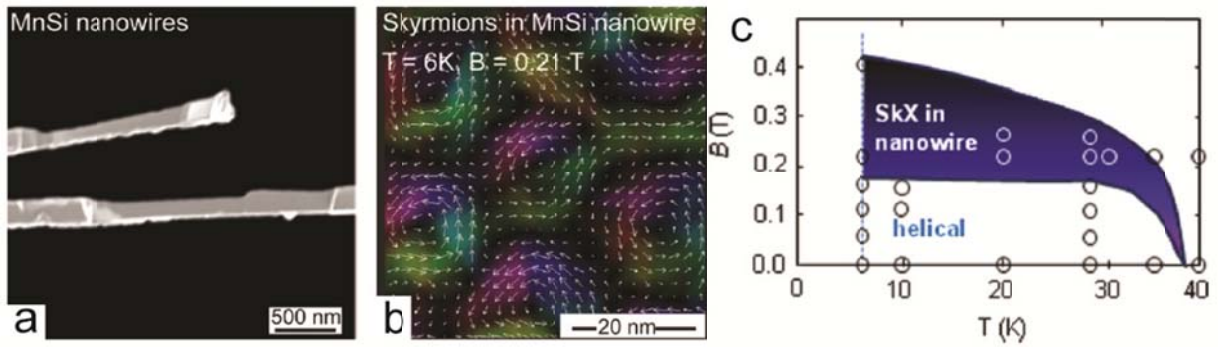


Figure 1.6. LTEM observation of a thin slab of MnSi NW.⁶⁰ a) A scanning electron micrograph of the final MnSi NW sample thinned with a focused ion-beam. b) Colorized image showing the in-plane magnetization direction with the characteristic hexagonal packing of the skyrmion lattice phase. c) Phase diagram constructed using the temperature and magnetic field points indicated by open circles, with the black boundary lines indicating the approximate phase boundaries between magnetic phases.

1.5 Origin of Electrical Transport Signature of Skyrmion Magnetic Domains

As has been mentioned previously, the magnetic skyrmion domain is a topologically non-trivial object that has certain particle-like properties. The topology of a given spin configuration is characterized by the winding number

$$\phi = \frac{1}{4\pi} \bar{n} \cdot \frac{\partial \bar{n}}{\partial x} \times \frac{\partial \bar{n}}{\partial y} \quad (1.5)$$

where $\bar{n} = \frac{\vec{M}_s}{|M_s|}$ is the local magnetization direction, and x and y are the coordinates perpendicular to the applied magnetic field. The skyrmion number, $\Phi = \int \phi(\vec{r}) d^2 r$, per 2D unit cell is quantized and adds up to -1 in the case of MnSi.⁹ As a short aside, one intriguing aspect of research pertaining to skyrmion domains is how such a non-trivial topological object can form from the topologically trivial helical precursor state. One study so far has attempted to answer this question using evidence from magnetic force microscopy (MFM) measurements and classical Monte Carlo (MC) simulations of an $\text{Fe}_{1-x}\text{Co}_x\text{Si}$ ($x = 0.5$) crystal.⁶¹ It was suggested the skyrmion lines can merge if and only if there is the presence of a point-like topological defect known as a hedgehog which can be interpreted as an emergent magnetic (anti)monopole.⁶¹

To understand the electrical transport signature of the skyrmion spin configuration, consider a conduction electron that passes through a skyrmion lattice (schematically depicted in Figure 1.7a). The conduction electron spin adiabatically couples to the local magnetization direction causing the conduction electron to pick up an additional Berry phase. This Berry phase can be re-interpreted as an Aharonov-Bohm phase with the associated emergent magnetic field^{44, 62, 63}

$$\vec{B}_i^e = \frac{\hbar}{2} \epsilon_{ijk} \hat{n} \cdot (\partial_j \hat{n} \times \partial_k \hat{n}) \quad (1.6)$$

where $\partial_i = \partial/\partial r_i$, and ε_{ijk} is the totally antisymmetric tensor. Essentially, the conduction electron will act as if it sees an additional magnetic field and the electron will be deflected transverse to its incident direction. This effective magnetic field causes an additional contribution to the measured Hall effect, and has thus been termed the “topological” Hall effect to differentiate it from the Berry phase an electron obtains in reciprocal space which has been well described as a mechanism leading to the anomalous Hall effect.⁶⁴ The topological Hall effect has become one of the definitive experimental signatures for identifying the skyrmion magnetic phase in chiral magnets.^{17, 18, 59, 65, 66}

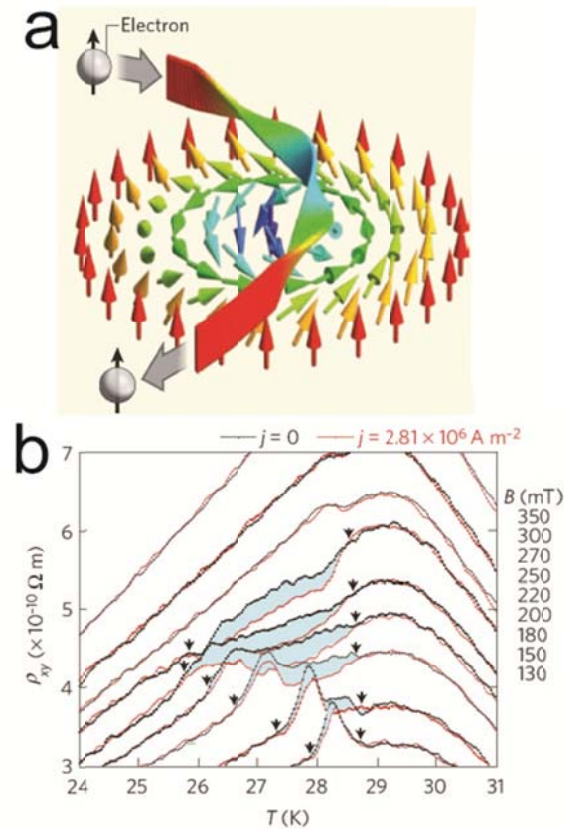


Figure 1.7. Electron-skyrmion interactions. a) Schematic depiction of a conduction electron moving adiabatically across a skyrmion magnetic domain (depicted with colored arrows indicating the local magnetization direction). Adapted by permission from Macmillan Publishers Ltd: Nature Ref. 15, © 2010. b) Data reproduced from Ref 44, demonstrating the effects of a large current density on the measured Hall resistivity. Above some threshold current value (shown as red lines) the measured Hall resistivity suddenly drops compared to the zero-current value indicating that the skyrmion lattice has begun to translate causing the appearance of the emergent electric field as discussed in the main text. Adapted by permission from Macmillan Publishers Ltd: Nature Physics Ref. 44, © 2012.

If we consider a chiral magnetic material, the measured Hall resistivity in the region of the skyrmion lattice is expected to have three additive components, $\rho_{xy} = \rho_{xy}^N + \rho_{xy}^A + \rho_{xy}^T$, where $\rho_{xy}^N = R_0 H$ is the normal Hall effect with Hall coefficient R_0 , ρ_{xy}^A is the anomalous Hall effect contribution, and ρ_{xy}^T is the topological Hall effect contribution.^{59, 66} The generic anomalous Hall resistivity can be written^{59, 67}

$$\rho_{xy}^A = \alpha M \rho_{xx0} + \beta M \rho_{xx0}^2 + b M \rho_{xx}^2 \quad (1.7)$$

where α , β , and b correspond to the skew scattering, side jump, and intrinsic contributions to the anomalous Hall resistivity, ρ_{xx0} is the residual resistivity, and M is the magnetization. Finally, the magnitude of the topological Hall effect for a static skyrmion lattice takes the form⁶⁶

$$\rho_{xy}^T \approx P R_0 B_z^e \quad (1.8)$$

where R_0 is the normal Hall coefficient, B_z^e is the effective field associated with a single unit cell of the skyrmion lattice, and P is the spin polarization of conduction electrons. Therefore, materials with large spin polarization of conduction electrons and smaller skyrmion domain sizes (and thus higher effective magnetic fields) are expected to produce the largest topological Hall effect signals. When the magnetization of the system can be measured, the topological Hall effect can be quantitatively extracted by subtracting the normal and anomalous Hall components, and therefore, has been used as a method to characterize the onset of the skyrmion lattice in several materials such as thin films of MnGe and FeGe.^{17, 18} For bulk and thin film MnSi, this topological Hall resistivity is roughly 10 nΩ·cm, but can be up to 50 nΩ·cm in bulk crystals when a large external pressure is exerted on the system.^{65, 68} The largest reported topological hall resistivities are for MnGe bulk crystals having small skyrmion domains (3-6 nm) and $\rho_{xy}^T \approx$

$-160 \text{ n}\Omega\cdot\text{cm}$ ¹⁸ and epitaxial FeGe(111) thin film with 18 nm thickness and $\rho_{xy}^T \approx 160 \text{ n}\Omega\cdot\text{cm}$.¹⁷

Furthermore, in the case of epitaxial FeGe(111) thin films, a 300 nm thin film had a significantly reduced value ($\rho_{xy}^T \approx 80 \text{ n}\Omega\cdot\text{cm}$) which might further indicate that the magnitude of the topological Hall signal can be increased by reducing the physical dimensions of the system.¹⁷

1.7 Spin Polarization Measurements by Andreev Reflection Spectroscopy

As can be seen in eq 1.8, the spin polarization (P) of conduction electrons in a chiral magnetic material may have significant impact on the magnitude of the measured topological Hall resistivity. Here, we will briefly introduce the only available technique for electrically measuring the spin polarization of an individual NW sample, namely Andreev reflection spectroscopy, which will be an essential tool for fully understanding the interaction of skyrmions and conduction electrons.

In an Andreev reflection experiment, a heterojunction is formed between the material of interest and a superconducting material (schematically shown with the band diagram in Figure 1.8). When the conduction electrons from the material being characterized impinge upon the interface with the superconductor, the conduction electrons must travel into the superconductor as Cooper pairs.^{69, 70} A Cooper pair refers to the collective motion of two electrons with opposite spin (spin up and spin down). For a diamagnetic material such as metallic copper, there are an equal number of spin up and spin down electrons in the conduction band ($P = 0$). In this case, the conduction electron impinging on the superconductor acquires an additional electron of opposite spin at the interface and passes into the superconductor, however, a hole must be reflected in the opposite direction (white circle shown moving left in Figure 1.8) to conserve the

momentum associated with the Cooper pair traveling into the superconductor (blue circle shown moving right in Figure 1.8). This reflected hole opens up a parallel conduction channel that doubles the conductance of the heterojunction and may be observed by measuring the differential conductance of the junction. In the case of non-zero spin polarization ($P \neq 0$), the formation of Cooper pairs will be hindered by the unequal number of spin up and spin down electrons at the conduction band, which causes a proportional decrease in the differential conductance signal compared to the case of $P = 0$. This simplified scenario will be further elaborated on in Chapter 2 where we discuss the specific case of spin polarization measurements of an individual chiral magnetic $\text{Fe}_{1-x}\text{Co}_x\text{Si}$ NW.

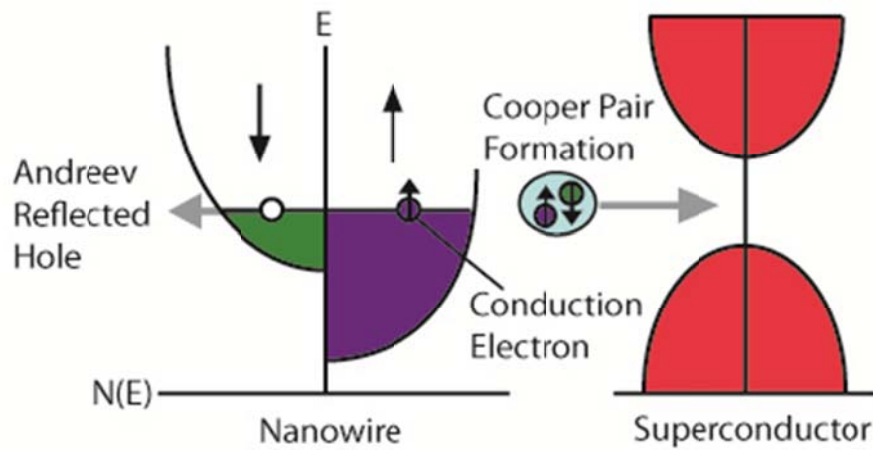


Figure 1.8. Energy (E) versus density of states [$N(E)$] schematic band diagram representation of a heterojunction formed between a spin-polarized NW and a superconductor. Black arrows indicate the spin-polarization of the spin-dependent conduction bands (green/purple shading). Gray arrows show the momentum associated with the Andreev reflected hole (moving left) and the Cooper pair formed at the interface between the materials (moving right).

1.7 Skyrmions in Motion and the Emergent Electric Field

The conduction electrons will impart a force on the skyrmion domains through the spin-transfer torque mechanism, and the skyrmion lattice will begin to translate when this force exceeds the pinning forces of the skyrmion lattice. As mentioned in the opening remarks of this introduction, skyrmion magnetic domains can be manipulated with current densities up to six orders of magnitude smaller than those used to manipulate ferromagnetic domain walls,^{38, 41, 71, 72} and therefore, skyrmion magnetic domains are extremely interesting for applications in future magnetic storage devices.^{35, 36} The first indications that the skyrmion magnetic domain could be manipulated at such low current densities via the spin-transfer-torque mechanism was a SANS study of bulk MnSi crystals that demonstrated the rotation of the six-fold diffraction pattern when a current density of $j = 2.22 \times 10^6$ A/m² was applied along with a small temperature gradient.⁴³ However, more definitive evidence of the moving skyrmion lattice is the depression of the Hall resistivity when exceeding a threshold current density (j_c). The origin of this signal is the motion of the effective magnetic field associated with the translating skyrmion lattice which necessitates the introduction of the emergent electric field,^{44, 62, 73}

$$\vec{E}_i^e = \hbar \hat{n} \cdot (\partial_i \hat{n} \times \partial_t \hat{n}) \quad (1.9)$$

where $\partial_t = \partial/\partial t$, and all other terms having the same definitions as in eq 1.6. In analogy with Faraday's law, the emergent electric field exerts an additional force on conduction electrons, $\vec{E}^e = -q_\sigma^e \vec{v}_d \times \vec{B}^e$, where \vec{v}_d is the velocity of the skyrmion lattice, and q_σ^e is the emergent charge associated with the spin of the conduction electron ($q_\uparrow^e = +1/2$ and $q_\downarrow^e = -1/2$). The induced current due to this additional force must be cancelled by an equivalent transverse Hall

field, $\Delta E_{\perp} \approx P \left| \frac{q^e}{e} \right| (\vec{v}_d \times \vec{B}^e)_y$, where P refers to the spin polarization.⁴⁴ Therefore, for $j \gg j_c$

we expect that the transverse Hall field will increase proportionally.

The emergent electric field associated with the translating skyrmion lattice was first observed in bulk MnSi through careful Hall effect measurements which demonstrated the expected change in the Hall resistivity as the current density was increased beyond the threshold value ($j_c = 2.81 \times 10^6$ A/m²) as shown in Figure 1.7b.⁴⁴ The motion of the skyrmion lattice at these very low current densities was also confirmed in LTEM observations of an FeGe thin film in which the skyrmion lattice appeared to move for a threshold current density of roughly 6.5×10^5 A/m².⁴² Although the actual speed of skyrmion lattice translation could not be directly determined in either study, a rough estimate approximates the speed to be on the order of 1.2×10^{-4} m/s.^{42, 44} This speed is not very competitive with those observed in ferromagnetic materials, but the primary advantages of a spintronics system implementing a skyrmion domain would be low power consumption and the ease of creating devices since control over impurities and other potential domain wall pinning sites does not need to be as strictly controlled.⁷⁴ As has been suggested in multiple theoretical works, the pinning forces on the skyrmion lattice are significantly weaker than in ferromagnetic systems or even the helimagnetic phase of chiral magnets due to the topological stability of the skyrmion domain.^{43, 62, 72, 74} Recent simulations have highlighted that the skyrmion lattice motion is unaffected by the presence of impurities (shown in Figure 1.9), and interestingly, the skyrmion domains can actually distort their individual domain shape to avoid these impurities.⁷⁴

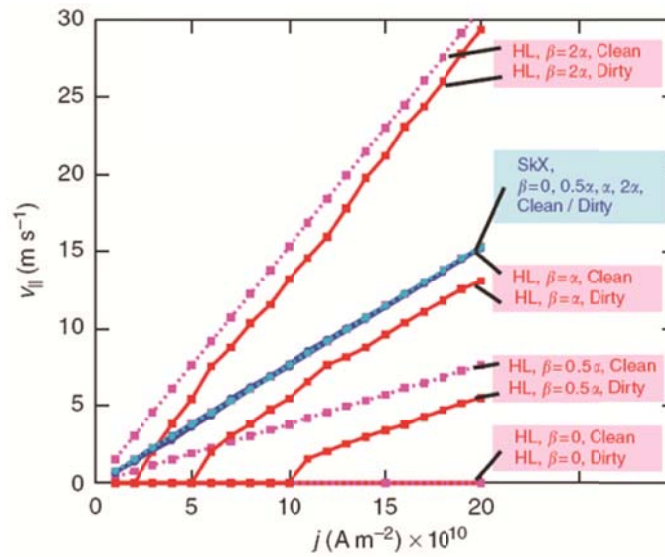


Figure 1.9. Current driven motion of the helimagnetic (HL) and skyrmion lattice (SkX) adopted from Ref 74. The red (a “dirty” sample having a large impurity density) and pink (a “clean” sample devoid of impurities) lines are simulations of the motion of the HL phase, and indicate the current driven motion requires a large critical current to achieve motion of the magnetic domains. Comparitively, SkX current driven motion appears unaffected by the presence of impurities, and the threshold current density required for domain translation is much lower than HL. Adapted by permission from Macmillan Publishers Ltd: Nature Communications Ref. 74, © 2013.

Nevertheless, it would still be interesting to have a way to measure the speed of the translating skyrmion domains much more precisely, and to accomplish this goal researchers have drawn from decades old technology based upon detection schemes for magnetic “bubbles.”⁷⁵ This recently demonstrated method for detecting the motion of magnetic domains uses Hall bar sensing elements for stray magnetic field detection. The proof of principle experiment was performed using Bi metal Hall bars on top of an iron garnet thin film to detect large magnetic domains.⁷⁶ The authors further proposed that such a Hall bar element could be used to detect skyrmion domains and provided some preliminary model calculations based upon the stray field associated with the skyrmion domain. This method seems to offer a promising way to further study the dynamics of skyrmion motion in a wide range of materials.

1.8 Motivation for Studying Skyrmions in Nanowires

With this background in chiral magnetism, and the dynamics of current-driven skyrmion domains, we may now summarize the key factors motivating investigations of chiral magnetism in NW materials. The skyrmion lattice phase is stabilized energetically over the conical phase when the size of the material approaches the skyrmion domain size, thus providing a much larger temperature-magnetic field window to observe skyrmions. Theory suggests that the skyrmion phase is further stabilized in a system with a significant anisotropy energy, which could be realized in NWs either through surface induced effects or through the intrinsic strain associated with the NW growth process. The critical temperature of magnetic ordering (T_c) has actually been shown to increase when the size of the system is reduced, such as the previously observed increase in helimagnetic ordering temperature observed by magnetoresistance and anomalous Hall effect measurements (Chapter 4) in MnSi NWs.⁷⁷⁻⁷⁹ Although this increase in T_c is opposite

what might be expected for finite size effects,⁸⁰ it is likely that the surface induced effects and strain associated with the growth of NWs outweigh the effects of nanoscale dimensions. Furthermore, an extended skyrmion phase stability compared to bulk MnSi crystals has recently been demonstrated by LTEM observations (Chapter 3) of a thinned slab of MnSi NW and topological Hall effect measurements of pristine MnSi NWs (Chapter 5).

The NW morphology is also natural geometry for the concept of racetrack memory applications. The skyrmion motion will be confined to move along the NW path, and moreover the nanoscale dimensions of NWs are more suited to high density packing for spintronic device applications. The bottom-up synthesis of chiral magnetic NWs can also be achieved with a much lower overhead cost compared to elaborate thin film fabrication of chiral magnetic materials that require expensive molecular beam epitaxy (MBE) systems. Lastly, certain dynamic regimes can be accessed at the nanoscale that cannot be achieved for bulk materials such as very large current densities that might be more relevant to functioning memory devices.

1.9 Synthesis of Silicide NWs

The recent surge in interest of nanomaterials owing to their unique properties compared to their bulk counterparts has spread to countless materials for many different applications,⁸¹⁻⁸⁴ and the B20 chiral magnets are no exception. The synthesis of silicide NWs has been complicated by the lack of success with well-known NW growth paradigms such as the vapor-liquid-solid (VLS) approach which utilizes a catalyst particle to promote 1-D growth by taking advantage of a low temperature eutectic in the binary phase diagram (as is the case for Si NWs catalyzed via gold nanoparticles).⁸⁵ In general, when considering the targeted vapor phase synthesis of silicide NWs, the two problems that must be addressed are the delivery of precursor materials and the

controlled anisotropic (1-D) crystal growth.⁸⁵ Silicide NW synthesis is further complicated by the complex binary phase diagrams of transition metals and silicon. For example, there are at least seven known intermetallic manganese silicide compounds that are stable at room temperature.⁸⁶ Over the last decade there has been a great deal of effort to develop synthetic strategies for targeting 1D silicide materials, broadly grouped into the following four categories: silicidation of Si NWs, decomposition of silicon on metal films, reaction of metals with silicon substrates, and deposition of both metal and silicon via chemical vapor deposition (CVD) or chemical vapor transport (CVT).⁸⁵ An extensive review of these developments in NW synthesis can be found in Ref. 86.

The two chiral magnetic silicide compounds, $\text{Fe}_{1-x}\text{Co}_x\text{Si}$ and MnSi , relevant to the remaining chapters of this work have been synthesized using CVD with single source precursors (SSPs) and metal halide precursors, the experimental setup is schematically shown in Figure 1.10. Specifically, $\text{Fe}_{1-x}\text{Co}_x\text{Si}$ NWs were first synthesized by mixing the two SSPs, $\text{Fe}(\text{SiCl}_3)_2(\text{CO})_4$ and $\text{Co}(\text{SiCl}_3)(\text{CO})_4$, and placing the mixture in a crucible that was inserted into the hot zone of a tube furnace to volatilize and deliver the precursors with inert gas to the growth substrate.⁸⁷ This synthesis procedure was subsequently improved with demonstrated control over the Co doping range ($0.05 \leq x \leq 0.45$) by adjusting the temperatures/positions of two separate precursor boats, one containing $\text{Fe}(\text{SiCl}_3)_2(\text{CO})_4$ and the other containing CoCl_2 .⁸⁸ A typical reaction results in long (greater than 5 μm) NWs with diameters that range between 30-80 nm and that grow along the [110] direction.^{88, 89} Using a different synthetic approach, MnSi NWs were synthesized in a similar experimental apparatus, but in place of the SSPs MnCl_2 was used as the transition metal source and a silicon substrate as the Si source. The reaction dynamics have not been fully detailed, but it is suggested that the MnCl_2 decomposes on the Si substrate which helps to

volatilize Si through the formation of SiCl_4 .⁷⁷ A typical MnSi NW synthesis results in very long (greater than 15 μm) NWs with diameters ranging from 100-300 nm and always grow along the [110] direction.⁷⁷

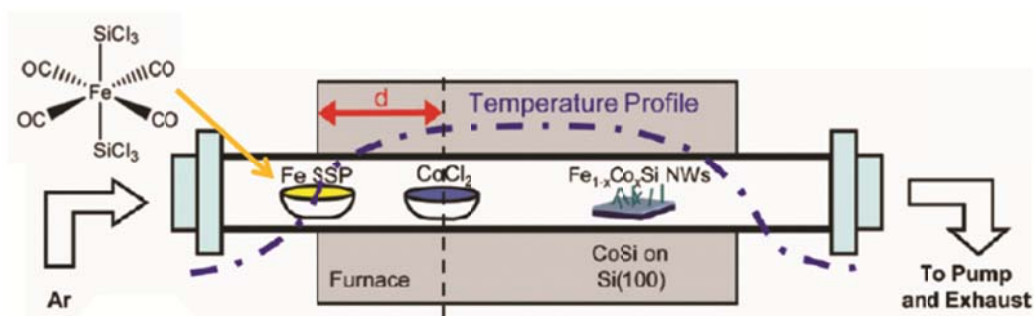


Figure 1.10. Schematic representation of a chemical vapor deposition (CVD) setup that has been used to synthesize $\text{Fe}_{1-x}\text{Co}_x\text{Si}$ NWs in an improved procedure, and can be adapted to synthesize MnSi NWs by changing the precursor material and growth substrate. The molecule shown in the yellow shaded boat is the single-source precursor $\text{Fe}(\text{SiCl}_3)_2(\text{CO})_4$ also used for the synthesis of FeSi NWs.^{87, 88, 90}

In addition to these well-established silicide NW syntheses, there have been several attempts at synthesizing NWs of the chiral magnetic B20 germanium analogues such as MnGe which is very interesting for its small skyrmion domain size (and thus large THE signal),¹⁸⁻²⁰ and FeGe which has the highest critical ordering temperature for the skyrmion magnetic phase of all the reported cubic chiral magnets.^{16, 17, 26, 42, 91-93} One approach for FeGe NW synthesis that has produced limited but promising results is via solid-state reaction in which germanium NWs are first grown by the preferential decomposition of a source gas (GeH₄) at gold catalyst nanoparticle (typically 25-100 nm diameter). Elemental iron is then deposited on the as-grown Ge NWs by electron-beam evaporation and subsequently annealed to promote diffusion of metal into the Ge NW. Despite successful formation of the B20 FeGe phase observed by select-area electron diffraction, the NWs produced via this method are polycrystalline, and therefore, are of less interest for transport measurements.⁹³

1.10 References

1. Dzyaloshinskii, I. E. *Phys. Chem. Solids* **1958**, *4*, 241-55.
2. Landau, L. D.; Lifshitz, E. M., *Electrodynamics of Continuous Media*. 2 ed.; Elsevier, Butterworth, Heinemann: New York, 2008; Vol. 8, p 451.
3. Moriya, T. *Phys. Rev.* **1960**, *120*, 91-98.
4. Yu, X. Z.; Mostovoy, M.; Tokunaga, Y.; Zhang, W. Z.; Kimoto, K.; Matsui, Y.; Kaneko, Y.; Nagaosa, N.; Tokura, Y. *Proc. Natl. Acad. Sci.* **2012**, 1-5.
5. Ishikawa, Y.; Tajima, K.; Bloch, D.; Roth, M. *Solid State Commun.* **1976**, *19*, 525-528.
6. Kadowaki, K.; Okuda, K.; Date, M. *J. Phys. Soc. Jpn.* **1982**, *51*, 2433-2438.

7. Lebech, B.; Harris, P.; Skov Pedersen, J.; Mortensen, K.; Gregory, C. I.; Bernhoeft, N. R.; Jermy, M.; Brown, S. A. *J. Magn. Magn. Mater.* **1995**, *140*, 119-120.
8. Binz, B.; Vishwanath, A. *Physica B* **2008**, *403*, 1336-1340.
9. Muhlbauer, S.; Binz, B.; Jonietz, F.; Pfleiderer, C.; Rosch, A.; Neubauer, A.; Georgii, R.; Boni, P. *Science* **2009**, *323*, 915-919.
10. Onose, Y.; Takeshita, N.; Terakura, C.; Takagi, H.; Tokura, Y. *Phys. Rev. B* **2005**, *72*, 224431/1-224431/12.
11. Uchida, M.; Onose, Y.; Matsui, Y.; Tokura, Y. *Science* **2006**, *311*, 359-361.
12. Yu, X. Z.; Onose, Y.; Kanazawa, N.; Park, J. H.; Han, J. H.; Matsui, Y.; Nagaosa, N.; Tokura, Y. *Nature* **2010**, *465*, 901-904.
13. Manyala, N.; Sidis, Y.; Ditusa, J. F.; Aeppli, G.; Young, D. P.; Fisk, Z. *Nat. Mater.* **2004**, *3*, 255-262.
14. Pfleiderer, C.; Adams, T.; Bauer, A.; Biberacher, W.; Binz, B.; Birkelbach, F.; Boni, P.; Franz, C.; Georgii, R.; Janoschek, M.; Jonietz, F.; Keller, T.; Ritz, R.; Muhlbauer, S.; Munzer, W.; Neubauer, A.; Pedersen, B.; Rosch, A. *J. Phys. Cond. Mat.* **2010**, *22*, 164207-1/164207-7.
15. Pfleiderer, C.; Rosch, A. *Nature* **2010**, *465*, 880-881.
16. Yu, X. Z.; Kanazawa, N.; Onose, Y.; Kimoto, K.; Zhang, W. Z.; Ishiwata, S.; Matsui, Y.; Tokura, Y. *Nature Mater.* **2011**, *10*, 106-109.
17. Huang, S. X.; Chien, C. L. *Phys. Rev. Lett.* **2012**, *108*, 267201/1-267201/5.
18. Kanazawa, N.; Onose, Y.; Arima, T.; Okuyama, D.; Ohoyama, K.; Wakimoto, S.; Kakurai, K.; Ishiwata, S.; Tokura, Y. *Phys. Rev. Lett.* **2011**, *106*, 156603-1/156603-4.

19. Kanazawa, N.; Kim, J. H.; Inosov, D. S.; White, J. S.; Egetenmeyer, N.; Gavilano, J. L.; Ishiwata, S.; Onose, Y.; Arima, T.; Keimer, B.; Tokura, Y. *Phys. Rev. B* **2012**, *86*, 134425/1-134425/7.
20. Makarova, O. L.; Tsvyashchenko, A. V.; Andre, G.; Porcher, F.; Fomicheva, L. N.; Rey, N.; Mirebeau, I. *Phys. Rev. B* **2012**, *85*, 205205-1/205205-5.
21. Seki, S.; Ishiwata, S.; Tokura, Y. *Phys. Rev. B* **2012**, *86*, 060403/1-060403/5.
22. Seki, S.; Kim, J. H.; Inosov, D. S.; Georgii, R.; Keimer, B.; Ishiwata, S.; Tokura, Y. *Phys. Rev. B* **2012**, *85*, 220406/1-220406/4.
23. Seki, S.; Yu, X. Z.; Ishiwata, S.; Tokura, Y. *Science* **2012**, *336*, 198-201.
24. White, J. S.; Levatic, I.; Omrani, A. A.; Egetenmeyer, N.; Prsa, K.; Zivkovic, I.; Gavilano, J. L.; Kholbrecher, J.; Bartkowiak, M.; Berger, H.; Ronnow, H. M. **2012**, arXiv:1208.1146v1.
25. Adams, T.; Chacon, A.; Wagner, M.; Bauer, A.; Brandl, G.; Pedersen, B.; Berger, H.; Lemmens, P.; Pfleiderer, C. *Phys. Rev. Lett.* **2012**, *108*, 237204/1-237204/5.
26. Moskvina, E.; Grigoriev, S.; Dyadkin, V.; Eckerlebe, H.; Baenitz, M.; Schmidt, M.; Wilhelm, H. *Phys. Rev. Lett.* **2013**, *110*, 077207/1-077207/5.
27. Skyrme, T. H. R. *Nucl. Phys.* **1962**, *31*, 556-569.
28. Bogdanov, A.; Hubert, A. *J. Magn. Magn. Mater.* **1994**, *138*, 255-69.
29. Bogdanov, A. N.; Yablonsky, D. A. *Sov. Phys. JETP* **1989**, *95*, 178-182.
30. Bogdanov, A. N.; Kudinov, M. V.; Yablonskii, D. A. *Sov. Phys. Solid State* **1989**, *31*, 99-104.
31. Rossler, U. K.; Bogdanov, A. N.; Pfleiderer, C. *Nature* **2006**, *442*, 797-801.
32. Butenko, A. B.; Leonov, A. A.; Rossler, U. K.; Bogdanov, A. N. *Phys. Rev. B* **2010**, *82*, 052403-1/052403-4.

33. Janoschek, M.; Garst, M.; Bauer, A.; Krautscheid, P.; Georgii, R.; Boeni, P.; Pfleiderer, C. *Phys. Rev. B* **2013**, *87*, 134407/1-134407/16.
34. Pulizzi, F. *Nature Mater.* **2012**, *11*, 367.
35. Kiselev, N. S.; Bogdanov, A. N.; Schafer, R.; Rossler, U. K. *J. Phys. D: Appl. Phys.* **2011**, *44*, 392001-1/392001-4.
36. Fert, A.; Cros, V.; Sampaio, J. *Nat. Nanotechnol.* **2013**, *8*, 152-156.
37. Bader, S. D.; Parkin, S. S. P. *Ann. Rev. Cond. Mat. Phys.* **2010**, *1*, 71-88.
38. Parkin, S. S. P.; Hayashi, M.; Thomas, L. *Science* **2008**, *320*, 190-194.
39. Brataas, A.; Bauer, G. E. W.; Kelly, P. J. *Phys. Rep.* **2006**, *427*, 157-255.
40. Albert, M.; Franchin, M.; Fischbacher, T.; Meier, G.; Fangohr, H. *J. Phys. Cond. Mat.* **2012**, *24*, 1-14.
41. Jiang, X.; Thomas, L.; Moriya, R.; Hayashi, M.; Bergman, B.; Rettner, C.; Parkin, S. S. P. *Nat. Commun.* **2010**, *1*, 1-5.
42. Yu, X. Z.; Kanazawa, N.; Zhang, W. Z.; Nagai, T.; Hara, T.; Kimoto, K.; Matsui, Y.; Onose, Y.; Tokura, Y. *Nat. Commun.* **2012**, *3*, 988-1/988-6.
43. Jonietz, F.; Muhlbauer, S.; Pfleiderer, C.; Neubauer, A.; Munzer, W.; Bauer, A.; Adams, T.; Georgii, R.; Boni, P.; Duine, R. A.; Everschor, K.; Garst, M.; Rosch, A. *Science* **2010**, *330*, 1648-1651.
44. Schulz, T.; Ritz, R.; Bauer, A.; Halder, M.; Wagner, M.; Franz, C.; Pfleiderer, C.; Everschor, K.; Garst, M.; Rosch, A. *Nat. Phys.* **2012**, *8*, 301-304.
45. Brataas, A.; Kent, A. D.; Ohno, H. *Nat. Mater.* **2012**, *11*, 372-381.
46. Heinze, S.; von Bergmann, K.; Menzel, M.; Brede, J.; Kubetzka, A.; Wiesendanger, R.; Bihlmayer, G.; Blugel, S. *Nat. Phys.* **2011**, *7*, 713-718.

47. Menzel, M.; Mokrousov, Y.; Wieser, R.; Bickel, J. E.; Vedmedenko, E.; Blugel, S.; Heinze, S.; von Bergmann, K.; Kubetzka, A.; Wiesendanger, R. *Phys. Rev. Lett.* **2012**, *108*, 197204/1-197204/5.
48. Romming, N.; Hanneken, C.; Menzel, M.; Bickel, J. E.; Wolter, B.; von Bergmann, K.; Kubetzka, A.; Wiesendanger, R. *Science* **2013**, *341*, 636-639.
49. Tchoe, Y.; Han, J. H. *Phys. Rev. B* **2012**, *85*, 174416/1-174416/8.
50. Lin, S.-Z.; Reichhardt, C.; Batista, C. D.; Saxena, A. *Phys. Rev. Lett.* **2013**, *110*, 207202-1/207202-5.
51. Bogdanov, A. N.; Rössler, U. K. *Phys. Rev. Lett.* **2001**, *87*, 037203-1/037203-4.
52. Wernick, J. H.; Wertheim, G. K.; Sherwood, R. C. *Mater. Res. Bull.* **1972**, *7*, 1431-1441.
53. Yasuoka, H.; Jaccarino, V.; Sherwood, R. C.; Wernick, J. H. *J. Phys. Soc. Jpn.* **1978**, *44*, 842-849.
54. Adams, T.; Chacon, A.; Wagner, M.; Bauer, A.; Brandl, B.; Pedersen, B.; Berger, H.; Lemmens, P.; Pfleiderer, C. *ArXiv.org* **2012**, arXiv:12041.3597v1.
55. Grundy, P. J.; Tebble, R. S. *Adv. Phys.* **1968**, *17*, 153-252.
56. Ishizuka, K.; Allman, B. *J. Electron Microsc.* **2005**, *54*, 191-197.
57. Reed Teague, M. *J. Opt. Soc. Am.* **1983**, *73*, 1434-1441.
58. Tonomura, A.; Yu, X. Z.; Yanagisawa, K.; Matsuda, T.; Onose, Y.; Kanazawa, N.; Park, H. S.; Tokura, Y. *Nano Lett.* **2012**, 1673–1677.
59. Li, Y.; Kanazawa, N.; Yu, X. Z.; Tsukazaki, A.; Kawasaki, M.; Ichikawa, M.; Jin, X. F.; Kagawa, F.; Tokura, Y. *Phys. Rev. Lett.* **2013**, *110*, 117202/1-117202/5.
60. Yu, X.; DeGrave, J. P.; Hara, Y.; Hara, T.; Jin, S.; Tokura, Y. *Nano Lett.* **2013**, 3755–3759.

61. Milde, P.; Köhler, D.; Seidel, J.; Eng, L. M.; Bauer, A.; Chacon, A.; Kindervater, J.; Mühlbauer, S.; Pfeiderer, C.; Buhrandt, S.; Schütte, C.; Rosch, A. *Science* **2013**, *340*, 1076-1080.
62. Zang, J. D.; Mostovoy, M.; Han, J. H.; Nagaosa, N. *Phys. Rev. Lett.* **2011**, *107*, 136804/1-136804/5.
63. Zhang, S.; Zhang, S. S. L. *Phys. Rev. Lett.* **2009**, *102*, 086601/1-086601/4.
64. Nagaosa, N.; Sinova, J.; Onoda, S.; MacDonald, A. H.; Ong, N. P. *Rev. Mod. Phys.* **2010**, *82*, 1539-1592.
65. Ritz, R.; Halder, M.; Franz, C.; Bauer, A.; Wagner, M.; Bamler, R.; Rosch, A.; Pfeiderer, C. *Phys. Rev. B* **2013**, *87*, 134424/1-134424/17.
66. Neubauer, A.; Pfeiderer, C.; Binz, B.; Rosch, A.; Ritz, R.; Niklowitz, P. G.; Boni, P. *Phys. Rev. Lett.* **2009**, *102*, 186602-1/186602-4.
67. Lee, M.; Onose, Y.; Tokura, Y.; Ong, N. P. *Phys. Rev. B* **2007**, *75*, 172403-1/172403-4.
68. Ritz, R.; Halder, M.; Wagner, M.; Franz, C.; Bauer, A.; Pfeiderer, C. *Nature* **2013**, *497*, 231-234.
69. Chalsani, P.; Upadhyay, S. K.; Ozatay, O.; Buhrman, R. A. *Phys. Rev. B* **2007**, *75*, 094417/1-094417/16.
70. Soulen, R. J., Jr.; Byers, J. M.; Osofosky, M. S.; Nadgorny, B.; Ambrose, T.; Cheng, S. F.; Broussard, P. R.; Tanaka, C. T.; Nowak, J.; Moodera, J. S.; Barry, A.; Coey, J. M. D. *Science* **1998**, *282*, 85-88.
71. Ryu, K.-S.; Thomas, L.; Yang, S.-H.; Parkin, S. S. P. *Appl. Phys. Express* **2012**, *5*, 093006/1-093006/3.

72. Everschor, K.; Garst, M.; Binz, B.; Jonietz, F.; Muehlbauer, S.; Pfliederer, C.; Rosch, A. *Phys. Rev. B* **2012**, *86*, 054432/1-054432/11.
73. Nagaosa, N.; Tokura, Y. *Physica Scripta* **2012**, *2012*, 014020/1-014020/15.
74. Iwasaki, J.; Mochizuki, M.; Nagaosa, N. *Nat. Commun.* **2013**, *4*, 1463/1-1463/8.
75. Eshenfelder, A. H., *Magnetic Bubble Technology*. Springer: New York, 1981.
76. Kubota, M.; Tokunaga, Y.; Kanazawa, N.; Kagawa, F.; Tokura, Y.; Kawasaki, M. *J. Appl. Phys.* **2013**, *114*, 053909/1-053909/4.
77. Higgins, J. M.; Ding, R.; DeGrave, J. P.; Jin, S. *Nano Lett.* **2010**, *10*, 1605-1610.
78. Seo, K.; Yoon, H.; Ryu, S.-W.; Lee, S.; Jo, Y.; Jung, M.-H.; Kim, J.; Choi, Y.-K.; Kim, B. *ACS Nano* **2010**, *4*, 2569-2576.
79. DeGrave, J. P.; Liang, D.; Jin, S. *Nano Lett.* **2013**, *13*, 2704-2709.
80. Fisher, M. E.; Barber, M. N. *Phys. Rev. Lett.* **1972**, *28*, 1516-1519.
81. Kempa, T. J.; Day, R. W.; Kim, S.-K.; Park, H.-G.; Lieber, C. M. *Energy Environ. Sci.* **2013**, *6*, 719-733.
82. Skomski, R. *J. Phys. Cond. Mat.* **2003**, *15*, R841-R896.
83. Lu, W.; Lieber, C. M. *J. Phys. D: Appl. Phys.* **2006**, *39*, R387-R406.
84. Dresselhaus, M. S.; Chen, G.; Tang, M. Y.; Yang, R.; Lee, H.; Wang, D.; Ren, Z.; Fleurial, J.-P.; Gogna, P. *Adv. Mater.* **2007**, *19*, 1043-1053.
85. Schmitt, A. L.; Higgins, J. M.; Szczech, J. R.; Jin, S. *J. Mater. Chem.* **2010**, *20*, 223-235.
86. Shukla, A.; Kang, Y.-B.; Pelton, A. D. *CALPHAD: Comput. Coupling Phase Diagrams Thermochem.* **2008**, *32*, 470-477.
87. Schmitt, A. L.; Higgins, J. M.; Jin, S. *Nano Lett.* **2008**, *8*, 810-815.

88. Higgins, J. M.; Carmichael, P.; Schmitt, A. L.; Lee, S.; DeGrave, J. P.; Jin, S. *ACS Nano* **2011**, *5*, 3268-3277.
89. DeGrave, J. P.; Schmitt, A. L.; Selinsky, R. S.; Higgins, J. M.; Keavney, D. J.; Jin, S. *Nano Lett.* **2011**, *11*, 4431-4437.
90. Schmitt, A. L.; Bierman, M. J.; Schmeisser, D.; Himpfel, F. J.; Jin, S. *Nano Lett.* **2006**, *6*, 1617-1621.
91. Wilhelm, H.; Baenitz, M.; Schmidt, M.; Naylor, C.; Lortz, R.; Rossler, U. K.; Leonov, A. A.; Bogdanov, A. N. *arXiv.org: Condens. Matter* **2012**, 1-16, arXiv:1203.4964v1.
92. Wilhelm, H.; Baenitz, M.; Schmidt, M.; Rossler, U. K.; Leonov, A. A.; Bogdanov, A. N. *Phys. Rev. Lett.* **2011**, *107*, 127203-1/127203-5.
93. Ding, R. H.; Berger, S. A.; DeGrave, J. P.; Jin, S. **2011**, (unpublished).

CHAPTER 2

*Spin Polarization Measurement of Homogeneously Doped Fe_{1-x}Co_xSi Nanowires by Andreev Reflection Spectroscopy**

2.1 Abstract

We report a general method for determining the spin polarization from nanowire materials using Andreev reflection spectroscopy implemented with a Nb superconducting contact and common electron-beam lithography device fabrication techniques. This method was applied to magnetic semiconducting Fe_{1-x}Co_xSi alloy nanowires with $\bar{x} = 0.23$ and the average spin polarization extracted from six nanowire devices is 28 ± 7 % with a highest observed value of 35 %. Local-electrode atom probe tomography (APT) confirms the homogenous distribution of Co atoms in the FeSi host lattice and X-ray magnetic circular dichroism (XMCD) establishes that the elemental origin of magnetism in this strongly correlated electron system is due to Co atoms.

* This chapter was published in *Nano Lett.*, **2011**, *11* (10), pp 4431–4437 and co-authored with A. L. Schmitt, R. S. Selinsky, J. M. Higgins, and S. Jin of the University of Wisconsin-Madison, and also D. J. Keavney of Advanced Photon Source at Argonne National Laboratory. A.L.S. carried out the APT and XMCD of the Fe_{1-x}Co_xSi nanowires, preliminary data was shown in the Ph.D. thesis of A.L.S.

2.2 Introduction

The burgeoning field of semiconductor spintronics promises to dramatically improve electronic devices by incorporating the spin degree of freedom of electrons instead of, or in addition to their charge.^{1, 2} Silicon appears to be an ideal material for demonstrating these new device concepts based on its long spin lifetime and the maturity of silicon processing technology.³⁻⁶ Silicon spin-based devices have thus far been hindered by a lack of efficient materials for direct spin-injection. An ideal injection source needs to be both highly spin-polarized and impedance-matched to silicon to overcome the conductance mismatch problem.⁷ The well-studied dilute magnetic semiconductors of $\text{Ga}_{1-x}\text{Mn}_x\text{As}$,⁸⁻¹⁰ the less studied concentrated magnetic semiconductors such as EuS ^{11, 12} and EuO ¹³ (both highly spin polarized), and CrO_2 ¹⁴ (half-metallic) suffer from poor electrical contact to silicon. The magnetic semiconducting metal silicide $\text{Fe}_{1-x}\text{Co}_x\text{Si}$, known to make ohmic contact to silicon,¹⁵ offers an alternative class of material that may serve as a promising injection source for silicon spintronics: $\text{Fe}_{1-x}\text{Co}_x\text{Si}$ is believed to be half-metallic^{16, 17} and displays the anomalous Hall effect.^{16, 18} Using the successful nanotechnology paradigm of the last ten years, the properties of these materials may be enhanced by accessing the nanoscale size regime.¹⁹ For example, the helimagnetic phase in MnSi is stabilized by nanowire morphology²⁰ and the Skyrmion magnetic ordering in $\text{Fe}_{1-x}\text{Co}_x\text{Si}$ is stabilized by thin film geometry.²¹ Additionally, nanowire morphologies have been used to demonstrate fundamental spintronics functionality such as tunneling spin injection from magnetic contacts into Ge nanowires,²² and two-terminal spin-valve behavior in $\text{MnSi}/\text{Si}/\text{MnSi}$ nanowire heterojunctions.²³

To determine the efficacy of a potential spin-injection material, it is essential to measure its absolute spin polarization ratio (P_s);^{1,24} however, there are no reported examples of spin

polarization measurements on nanowires to our knowledge. Common optical methods applicable to bulk or thin film materials such as spin-polarized photoemission are formidable to implement at the nanoscale. An electrical method is preferable for nanowire geometry and can be realized using superconducting junctions. Spin-polarized tunneling spectroscopy developed by Tedrow and Meservey measures the contact polarization, however this method requires thin and highly uniform tunneling barriers which are difficult to fabricate for many systems.²⁴⁻²⁶ Point contact Andreev reflection (PCAR) spectroscopy can be implemented by directly contacting a superconductor to the material of interest and measuring the intrinsic spin polarization.^{24, 27} In PCAR spectroscopy, electrons traversing the interface between the material and the superconductor with energy greater than the superconducting gap enter the superconductor as quasi-electrons and then relax into Cooper-pairs over a characteristic length-scale. When incident electrons have energy less than the superconducting gap, they tunnel directly into the superconductor as Cooper pairs. In order for this to occur, an incident electron pairs up with an electron of opposite spin, and a hole is reflected with opposite momentum. This effectively opens a second conductance channel that doubles the normal state conductance of the material in the limit of zero spin polarization. When there is a net spin-imbalance (P_s) defined as

$$P_s = \frac{(N_\uparrow - N_\downarrow)}{(N_\uparrow + N_\downarrow)} \quad (2.1)$$

where N_\uparrow and N_\downarrow are the spin dependent densities of states at the Fermi level, the formation of Cooper pairs will be suppressed causing a depression in the conductance. This spin polarization (P_s) can be extracted from the normalized differential conductance when the temperature and interfacial scattering are sufficiently small using $G(0)/G_n = 2(1 - P_s)$, where G_n is the normal state conductance measured just above the superconducting critical temperature, and $G(0)/G_n$ is

the normalized conductance at zero-bias.²⁴ PCAR spectroscopy has been successfully implemented with thin film samples by mechanically pressing sharpened superconducting tips into them to reveal the spin polarization of several important materials including common metals such as Ni,²⁴ Fe,²⁴ Co,^{24,28} as well as CrO₂^{24,29,30} and (Ga,Mn)As³¹ among many others.

However, mechanically contacting nanomaterials is burdensome. Therefore, we need to develop a lithographic device fabrication technique to make superconducting junctions suitable for extracting the spin polarization of nanowires using Andreev reflection. Herein we report an Andreev reflection spectroscopy method for nanowires and present the spin polarization measurements for Fe_{1-x}Co_xSi nanowires. We also provide a tomographic reconstruction of Fe_{1-x}Co_xSi nanowires to confirm the homogenous dopant distribution by atomic probe tomography (APT). The elemental origins of magnetism in this system are determined using X-ray magnetic circular dichroism (XMCD).

2.3 Results and Discussion

Three different samples of Fe_{1-x}Co_xSi nanowires with \bar{x} ranging from $0.18 \leq \bar{x} \leq 0.27$ were synthesized using a homebuilt chemical vapor deposition system and used for the present work. Samples 1 and 2 were grown by mixing two single source precursors,³² while Sample 3 was grown with an improved synthesis using the Fe(CO)₆(SiCl₃)₂ single source precursor and CoCl₂ precursor³³ (see Appendix 1 for detailed synthesis procedures). Both synthetic routes result in wires with similar morphology, and a representative scanning electron micrograph (SEM) of Sample 3 is shown in Figure 2.1a. We have also determined the Co concentration (x) for each of the samples by energy dispersive spectroscopy (EDS) analysis on individual nanowires (Figure 2.1b).

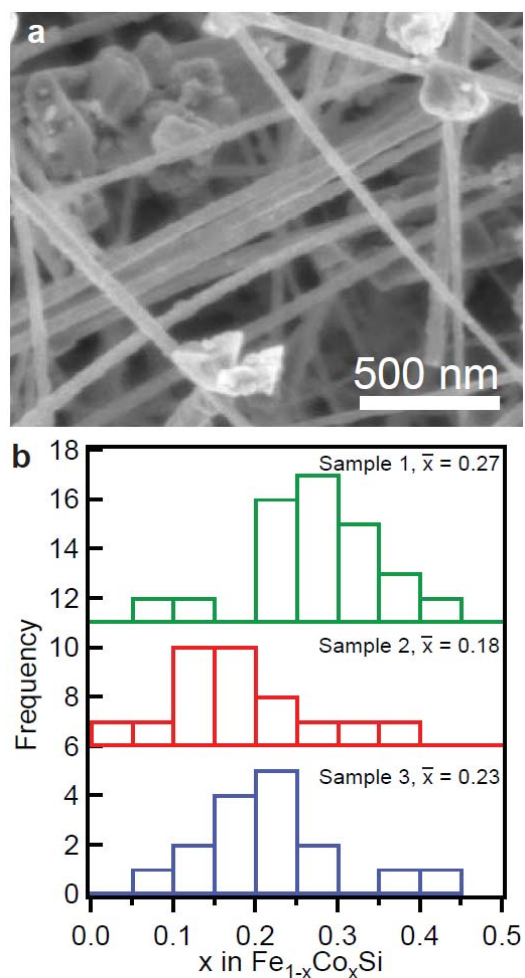


Figure 2.1. SEM and EDS analyses of the typical $\text{Fe}_{1-x}\text{Co}_x\text{Si}$ nanowires used in this study. a) Representative SEM of Sample 3. Both Sample 1 and Sample 2 have similar nanowire density and morphology. b) Histograms of the composition x for the three $\text{Fe}_{1-x}\text{Co}_x\text{Si}$ samples as determined by EDS of many individual nanowires.

In doped or alloyed nanomaterials, determining the structure-property relationships is challenging. Lack of complete microstructural understanding often leads to several possible data interpretations and is further complicated by nanoscale morphology. Atom probe tomography (APT) is a relatively new tool for materials scientists that offers spatial and elemental 3-D resolution of nanoscale materials.³⁴ Recent advances in APT technology have expanded the number and type of materials that can be studied. Initially, only metals satisfied the criteria for field evaporation,³⁵ but as a result of laser-pulsed methods for lowering the field evaporation threshold of semiconductors, APT of more resistive materials has become possible.³⁶ In contrast to scanning transmission electron microscopy (STEM), which yields 2-D projections and has elemental uncertainties on the order of the beam size ~ 1 nm, APT can create 3-D projections with \AA resolution and ppm elemental mapping within the structure. This unprecedented level of microstructural understanding is crucially important for systems in which doping and elemental distribution can dramatically affect the materials properties. APT has been applied to investigate doped nanowire materials yielding unprecedented insights.³⁷

APT is generally limited either to samples milled into 100 nm diameter slab using a focused ion-beam (FIB),³⁸⁻⁴⁰ or to nanowires grown epitaxially on conductive substrates.⁴¹⁻⁴³ We removed nanowires from a growth substrate and mechanically mounted them onto fabricated silicon posts using a micromanipulator tip. The nanowires were welded via electron-beam deposition of platinum metal inside a Zeiss Cross-beam SEM (see Appendix 1 for additional detail). This mounting procedure can be applied to other freestanding nanowire materials. Several $\text{Fe}_{1-x}\text{Co}_x\text{Si}$ wires from Sample 2 ($\bar{x} = 0.18$) were mounted and successfully analyzed using an IMAGO laser-pulsed local electrode atom probe (LEAP) instrument. Wires were cooled to 60 K and would typically begin field evaporation at a laser frequency of 50 kHz and a power

of 0.1 nJ. As seen in a representative mass spectrum shown in Figure 2.3a, attempts to analyze both Fe and Si simultaneously turned out to be problematic due to the $m/2$ overlap between the $^{54}\text{Fe}^{2+}$ and $^{27}\text{Si}^+$ peaks; therefore, we focused on optimizing the scans to produce the combination peaks FeSi^{2+} and CoSi^{2+} to investigate the atomic distribution of Co in the FeSi host lattice. For pulsed laser LEAP, we found that these complexes come off more readily at higher laser energies. Higher laser powers tend to increase the DC evaporation rate resulting in an additional contribution to the background that cannot be correlated, but can be suppressed by using lower voltages and higher temperatures. The APT data was analyzed using IMAGO's reconstruction software. The FeSi^{2+} and CoSi^{2+} events were used to create a selected volume reconstruction of the original mounted nanowire from an experimental run with $\sim 500,000$ ions collected (Figure 2.2b). From this map and others like it, we conclude that Co is, as expected, homogeneously distributed within the FeSi host lattice.

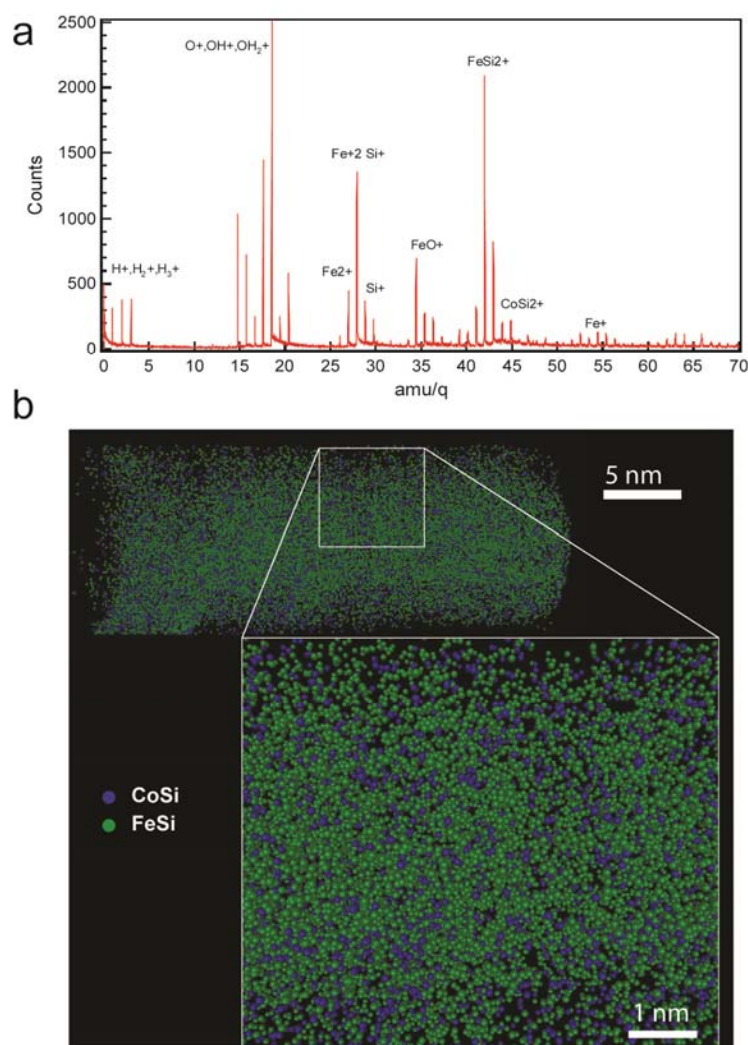


Figure 2.2. Atom probe tomography experiments of $Fe_{1-x}Co_xSi$ nanowires. a) The mass spectrum from a nanowire (~ 20 nm in diameter) from Sample 2 ($\bar{x} = 0.18$) mounted to a conductive silicon post. Contributions to the mass spectrum from Fe, Co, Si, and O moieties are labeled. b) 3D tomographic reconstruction of a $Fe_{1-x}Co_xSi$ nanowire highlighting the Co distribution in the FeSi lattice using the $FeSi^{2+}$ and $CoSi^{2+}$ combination peaks from a).

After carefully confirming the $\text{Fe}_{1-x}\text{Co}_x\text{Si}$ nanowire microstructure, we probed the magnetic properties of these materials using X-ray magnetic circular dichroism (XMCD). XMCD offers the ability to directly interrogate the spin-dependent density of states within a material with electronic and elemental specificity. Left and right circularly polarized (LCP and RCP, respectively) X-rays generated from a synchrotron source are focused onto the sample. A monochromator is used to scan the X-ray energy through an appropriate absorption resonance, in this case the Fe and Co $L_{3,2}$ and Si K edges. X-ray absorption is measured by monitoring the total electron yield (TEY) (electrons emitted from the sample as a result of X-ray absorption) or the total fluorescence yield (TFY), and the difference between LCP and RCP is the XMCD signal. XMCD on $\text{Fe}_{1-x}\text{Co}_x\text{Si}$ alloy nanowires [removed from the growth substrate of Sample 1 ($\bar{x} = 0.27$)] was performed at the Advance Photon Source beamline 4-ID-C at Argonne National Laboratory at 6 K and a magnetic field of 2 T (see Appendix 1 for experimental details). Figure 2.3a shows the X-ray absorption spectra of the nanowires at the Co L edge, the corresponding theoretical spectra for Co^{2+} and Co^{3+} electronic states, and a fit of a superposition of these two calculated spectra to the experimental data. The theoretical spectra were generated using the CTM4XAS program (for Co the parameters used were $C4$ symmetry, $M = 850$ meV, and $10Dq = -0.1$),⁴⁴ interpolated, and fit as shown. Figure 2.3b shows the XMCD spectra of the nanowires at the Co L edge, the corresponding theoretical spectra for the Co^{2+} and Co^{3+} L edge and a fit of the theoretical spectra to the experimental data. The fitting of the XAS and XMCD spectra yields compositions of approximately 91 % Co^{2+} and 9 % Co^{3+} ($R^2 = 0.95$) and 100 % Co^{2+} and 0 % Co^{3+} ($R^2 = 0.83$) respectively. Therefore, Co $3d$ electrons, specifically those attributed to Co^{2+} , are strongly contributing to the spin imbalance of the magnetic $\text{Fe}_{1-x}\text{Co}_x\text{Si}$ nanowires. Previous polarized neutron diffraction studies on $\text{Fe}_{1-x}\text{Co}_x\text{Si}$ alloys⁴⁵ suggest this system is an itinerant

electron magnet but found both $3d$ magnetic moments localized on (Fe,Co) sites and a weak moment delocalized over the crystal. The current XMCD study shows these localized moments are primarily attributed to Co atoms. To understand better the electronic structure of the FeCoSi alloy, we can compare the XAS of Co and Fe in the FeCoSi alloy to that of the Co and Fe found in pure CoSi and FeSi NWs.^{46, 47} The XAS of the Co $L_{3,2}$ and Fe $L_{3,2}$ edges for the alloy show sharper multiplet structure than the XAS for the pure CoSi and FeSi respectively. This indicates that the alloyed material has more localized $3d$ Co and Fe band states than the pure CoSi or FeSi.

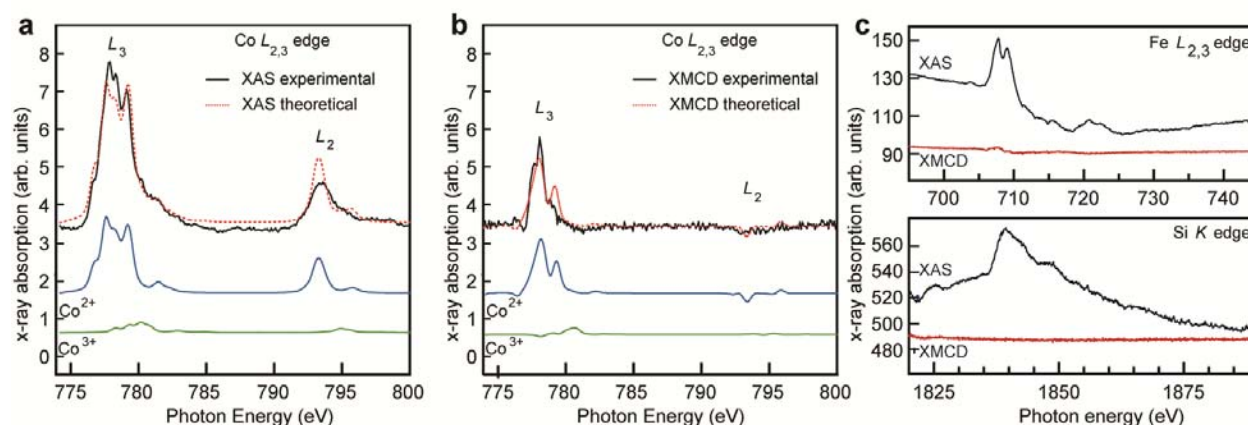


Figure 2.3. X-ray magnetic circular dichroism (XMCD) of the $\text{Fe}_{1-x}\text{Co}_x\text{Si}$ nanowires, Sample 1 ($\bar{x} = 0.27$). a) Experimental XAS of the Co L edge, theoretical fit of the XAS spectra, and the contributing theoretical XAS spectra for Co^{2+} and Co^{3+} . The XAS fit shows predominantly (91 %) Co^{2+} in the $\text{Fe}_{1-x}\text{Co}_x\text{Si}$ nanowires. b) Experimental XMCD of the Co L edge, theoretical fit of the XMCD spectra, and the contributing theoretical XMCD spectra for Co^{2+} and Co^{3+} . The XMCD fit indicates Co^{2+} is the primary magnetic contributor in the $\text{Fe}_{1-x}\text{Co}_x\text{Si}$ nanowires. c) XAS and XMCD scans for Fe and Si confirm the presence of the elements but indicate that neither is a significant contributor to the spin imbalance. The XAS and XMCD signals are in arbitrary units and are not normalized between Co, Fe, and Si elements.

To determine magnetic contributions from Fe and Si, XMCD scans were taken of the Fe $L_{3,2}$ (Figure 2.3c top panel) and Si K edges (Figure 2.3c bottom panel). Sufficient statistics were collected such that the noise level in the XMCD relative to the L_3 XAS peak height for Fe and Si are approximately 1.2 and 2.15% respectively. A small but significant Fe XMCD signal was observed (approximately 4–5 % of the XAS peak height) for the Fe $L_{3,2}$ which is consistent with the 1-2 nm oxide layer previously reported for the $Fe_{1-x}Co_xSi$ nanowires. We see no XMCD signal at the Si K edge above the noise level of 2.15% of the XAS peak height. The lack of a Si XMCD signal indicates that any magnetic contribution is very small and as such Si is not a significant contributor to the magnetic moments of the $Fe_{1-x}Co_xSi$ nanowires.^{45, 47} Thus the predominance of the Co XMCD over the small Fe and unobserved Si XMCD signals adheres to the conventional wisdom that Co is primarily, if not solely, responsible for the unusual magnetic behavior in $Fe_{1-x}Co_xSi$. These results are also consistent with the magnetometry experiments showing one Bohr magneton is added for every Co incorporated into the FeSi host lattice up to a 25 % doping level.^{16, 18, 48}

With the homogeneous dopant distribution and origin of magnetism established for $Fe_{1-x}Co_xSi$ nanowires, we set out to measure the spin polarization using Andreev reflection spectroscopy. Our initial design of the Andreev reflection measurements of nanowires used a four probe scheme (Figure A1.1a) that resembles what is commonly reported for electrical measurements on nanowire devices^{20, 32} except that half of the probes were normal metal contacts (Ti/Au) and the others superconducting (Nb). We found that this particular setup resulted in very poor success rates and peculiar conductance behavior that often mimicked the shape of Andreev reflection signal but was independent of the superconducting state of the Nb contacts. The key observation leading to higher success rates was that very short channel devices

(typically < 200 nm) yielded optimal results for Andreev reflection signal. We hypothesize that since $\text{Fe}_{1-x}\text{Co}_x\text{Si}$ is a highly disordered metal and typical nanowire resistivities are on the order of $1 \text{ m}\Omega\text{-cm}$, a short channel has the advantage of decreasing the series resistance (discussed in detail below) which otherwise causes the Andreev signal to be obscured in the background differential conductance.

Therefore, we designed devices where the Nb contact is as close as possible to the normal metal contact. Because the Ti/Au and Nb electrode are defined in two separate lithography and deposition steps, these two electrodes often end up shorted due to the inevitable lithographic misalignment as well as a lack of control over the electrode width during the sputter deposition of Nb. To overcome this issue we cap the Ti/Au contacts with an additional insulating layer of Al_2O_3 (40 nm) by rotating the sample stage during e-beam deposition of Al_2O_3 resulting in the device structure schematically shown in Figure 2.4a. Such insulating Al_2O_3 capping layer would prevent the shorting between Nb and Ti/Au in the event that the two electrodes physically overlap. The inset of Figure 2.4b shows the SEM of a working device (Device 1) demonstrating that even though the electrodes slightly overlap, the resistance versus temperature data for Device 1 (Figure 2.4b) confirms that the two-probe junction is not metallic as would be expected for a direct short between the normal metal and superconducting metal. In addition to fabricating short channel nanowire structures, we determined that a two-probe geometry would best mimic previous works on thin film Andreev reflection measurements. Each of the two physical electrodes to the $\text{Fe}_{1-x}\text{Co}_x\text{Si}$ nanowire split after the active channel for independent current and voltage measurement (Figure 2.4a).

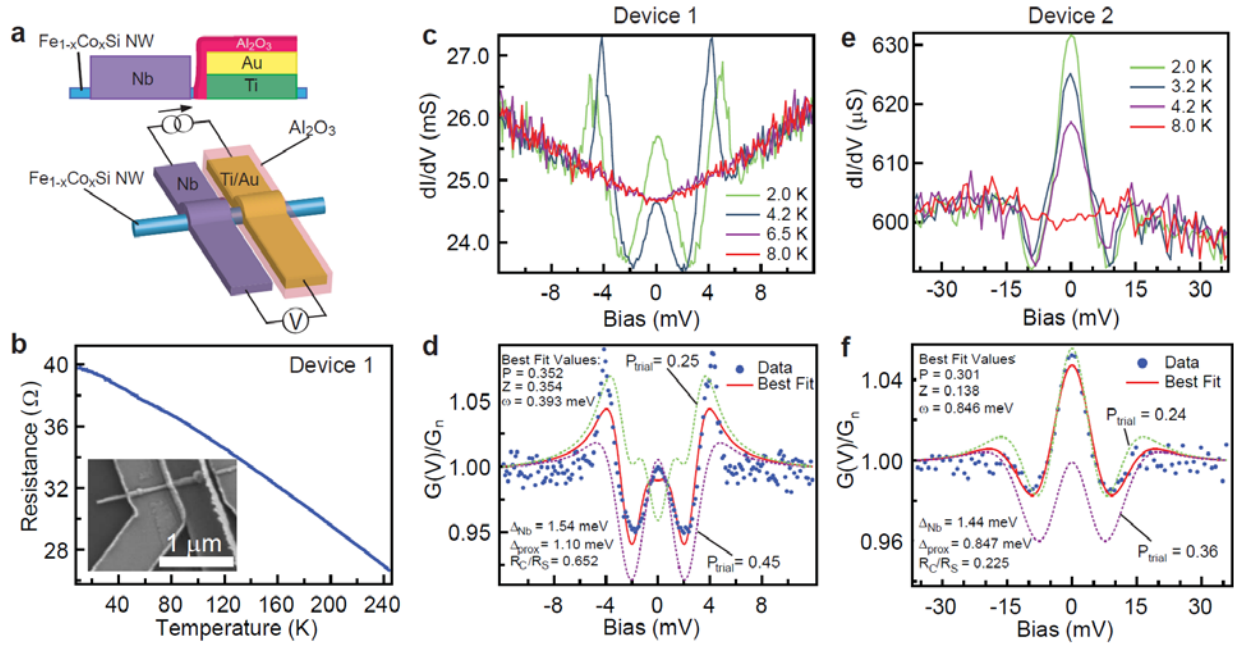


Figure 2.4. Andreev reflection spectroscopy of Fe_{1-x}Co_xSi nanowires from Sample 3 ($\bar{x} = 0.23$). a) Top diagram shows a schematic cross-section view of the two-probe nanowire device design and the bottom diagram shows a top down schematic of the nanowire device design and the electrical measurement setup. b) Resistance versus temperature for Device 1, inset shows a SEM of the nanowire device. c, e) Raw differential conductance as a function of bias voltage data for Device 1 and Device 2 at various temperatures up to the critical temperature of Nb. d, f) Normalized differential conductance as a function of bias voltage for Device 1 and Device 2. Best fit parameters to the modified BTK model are given for each device in addition to two spectra generated from the indicated P_{trial} values.

Nanowire devices were loaded into chip carriers and bonded with aluminum wire, and then measured in a Quantum Design physical properties measurement system (PPMS-9T) down to a temperature of 2 K. Differential conductance data was collected in the two-probe geometry using a DC technique implemented with a Keithley 6221 Current Source and Keithley 2182A Nanovoltmeter. A total of seven $\text{Fe}_{1-x}\text{Co}_x\text{Si}$ nanowire devices were successfully measured that yielded interpretable Andreev reflection behavior. We report two devices in the main text with the characteristic Andreev reflection signal and an additional five data sets are included in Appendix 1. The raw differential conductance curves (Figure 2.4c,e) were collected at multiple temperatures showing decreasing Andreev signal as T_c of Nb (~ 9 K) is approached. The key features of Andreev reflection appear in both Device 1 and Device 2: (1) the appearance of scattering peaks at $\pm\Delta_{\text{Nb}}$; (2) finite width of the scattering peaks due to proximity related effects; and (3) the symmetric peak near zero-bias. Due to the proximity effect and additional broadening of the Andreev peaks, the spin polarization cannot be extracted from the height of the peak at zero-bias using the simplistic equation of $G(0)/G_n = 2(1 - P_s)$.

In order to properly extract P_s , the raw differential conductance curves are first normalized by spectra in which the peaks characteristic of Andreev reflection collapse to the baseline differential conductance (this happens above the T_c of the Nb contact which can vary slightly from the bulk T_c of Nb due to the geometry of the contact). The data for Device 1 and Device 2 were both normalized by scans taken at 8.0 K (Figure 2.4d,f) and then analyzed using the 1-D modified Blonder-Tinkham-Klapwijk (BTK) model in the ballistic regime with the addition of a proximity effect correction.²⁸ Although it is uncertain whether or not the contacts in this experiment are in the ballistic or diffusive regime, it has been noted in previous work that the

extracted polarization is nearly identical for both models.⁴⁹ Furthermore, the uncertainty in transport regime is largely absorbed by the Z parameter (defined below).⁴⁹ From BTK theory the following equation can be used to generate theoretical normalized differential conductance curves,

$$G(V) = \int_{-\infty}^{\infty} \frac{df(E-V, T)}{dV} [1 + A(E, Z) - B(E, Z)] dE \quad (2.2)$$

where V is the bias voltage, E is energy of the incident electron, Z is the dimensionless parameter that absorbs all interface effects, $f(E)$ is the Fermi-Dirac distribution, A is the probability of Andreev reflection, and B is the probability of normal reflection. We implemented the appropriate definitions of A and B for the proximity effect as worked out by Strijkers et al.²⁸ Additionally, in our fitting procedure the derivative of the Fermi-Dirac distribution is approximated by a Gaussian $e^{-[(E-V)/2\omega]^2}$ where ω is equal to $k_b T$ in an ideal device, however, in non-ideal devices this parameter absorbs processes indistinguishable from thermal broadening including inelastic scattering, local heating, and pair breaking effects.⁴⁹ $G(V)$ is decomposed into a fully unpolarized channel (G_N) and a fully polarized channel (G_P) weighted by P_s

$$G(V) = (1 - P_s)G_N(V) + P_s G_P(V) \quad (2.3)$$

The experimental spectra are further complicated by the appearance of the superconducting gap at bias values much higher (sometimes tens of mV) than the expected BCS value for bulk Nb ($\Delta_{Nb} = 1.50$ meV). This is due to the voltage drop in the nanowire channel before the superconducting interface and is accounted for in our model by assuming a series resistance of the form $V_{\text{total}} = V_{\text{junction}} + V_{\text{nanowire}}$. This “spreading resistance” is fit using an additional adjustable parameter, defined as the ratio of the junction resistance to the spreading resistance

(R_c/R_s), while holding Δ_{Nb} constant at the bulk BCS value for Nb. In subsequent fitting steps the spreading resistance is held constant and the other five parameters (P_s , Z , ω , Δ_{prox} , Δ_{Nb}) are allowed to fully optimize with the exception of Δ_{Nb} which is held in a tight range (± 0.06 meV) about the BCS value. Constraining Δ_{Nb} allows us to avoid possible degeneracy in the fitting of Δ_{Nb} and the spreading resistance while allowing the model to compensate for non-ideal contact geometries that may result in small fluctuations of the accepted superconducting gap value for Nb.⁵⁰ Fitting results are shown for Device 1 and Device 2 in Figure 2.4d and 4f, respectively.

Fitting spectra with the modified BTK model can return degenerate results leading to ambiguity in the determination of the spin polarization because the model might compensate a change in P_s with the Z parameter. Following the procedure of Rigato et al. we test the robustness of the fitting results by selecting a P -trial, allowing Z and ω to vary, and then comparing the trial fit to the original best fit.⁵⁰ The resulting fits (dotted lines in Figures 2.4d,f) are significantly worse, which demonstrates that Z and ω cannot compensate for the arbitrary change in P and confirms the robustness of the fitting and the extracted spin polarization values. We also note that conductance features that commonly appear near the superconducting gap edge vary in size and shape from device to device. These features are not accounted for in the modified BTK model and deteriorate the quality of the fit. The contact area is large compared to the length of the nanowire channel resulting in multiple non-uniform point contacts which likely causes the anomalous conductance features. It has been noted that better fits can be obtained by assuming three-dimensional contacts as opposed to the one-dimensional model implemented here, however the extracted polarization value varies only slightly between the two models and the observed conductance features would still be unaccounted for.⁵¹ All of these factors taken into consideration, six devices led to robust and unique fits and the average polarization ratio (P_s)

extracted was 28% with 7% standard deviation among the six devices, the largest polarization extracted was 35% (shown in Figure 2.4d) and the lowest extracted value was 16%. The effective temperature for Device 1 was 0.393 meV which is very near the ideal limit (0.362 meV at 4.2 K) indicating an absence of additional broadening effects.

2.4 Conclusion

In summary, we have employed APT, XMCD, and Andreev reflection techniques to thoroughly characterize the structural and magnetic properties of $\text{Fe}_{1-x}\text{Co}_x\text{Si}$ nanowires. Atom probe tomography confirms the homogeneous distribution of Co atoms within the FeSi host lattice. XMCD establishes that Co is the primary contributor to the spin imbalance in $\text{Fe}_{1-x}\text{Co}_x\text{Si}$ nanowires. Moreover, a general methodology for measuring Andreev reflection in nanowire devices was developed and used to extract an average spin polarization of $28 \pm 7\%$ for $\text{Fe}_{1-x}\text{Co}_x\text{Si}$ ($\bar{x} = 0.23$) nanowires. Measuring the spin polarization of nanomaterials is a difficult task and the analysis can be complex, yet we have shown Andreev reflection measurement on lithographically fabricated nanowire devices to be an effective approach. The relatively simple assumptions in the modified BTK model fit the Andreev reflection data well. This demonstrates that this technique could be generally applicable to other interesting magnetic nanowire materials especially where the interfaces can be engineered more reliably and the intrinsic electrical transport is less disordered. These characterization techniques can be extended to other nanomaterials where the doping concentration and distribution within the material is strongly correlated to its physical properties.

2.5 Acknowledgement

This research was supported by the Research Corporation for Science Advancement through a Cottrell Scholar Award. S.J. also thanks NSF (CBET-1048625) and the Sloan Research Fellowship for support. Use of the Advance Photon Source was supported by the U.S. Department of Energy, Office of Science, Office of Basic Energy Sciences, under Contract DE-AC02-06CH11357.

2.6 References

1. Zutic, I.; Fabian, J.; Das Sarma, S. *Rev. Mod. Phys.* **2004**, *76*, 323-410.
2. Wolf, S. A.; Jiwei, L.; Stan, M. R.; Chen, E.; Treger, D. M. *Proc. IEEE* **2010**, *98*, 2155-2168.
3. Zutic, I.; Fabian, J.; Erwin, S. C. *Phys. Rev. Lett.* **2006**, *97*, 026602/1-026602/4.
4. Appelbaum, I.; Huang, B. Q.; Monsma, D. J. *Nature* **2007**, *447*, 295-298.
5. Jang, H. J.; Xu, J.; Li, J.; Huang, B. Q.; Appelbaum, I. *Phys. Rev. B* **2008**, *78*, 165329-1/165329-6.
6. Li, C. H.; van 't Erve, O. M. J.; Jonker, B. T. *Nat. Commun.* **2011**, *2*, 1256/1-1256/7.
7. Fert, A.; Jaffres, H. *Phys. Rev. B* **2001**, *64*, 184420/1-184420/9.
8. Ohno, H.; Shen, A.; Matsukura, F.; Oiwa, A.; Endo, A.; Katsumoto, S.; Lye, Y. *Appl. Phys. Lett.* **1996**, *69*, 363-365.
9. Macdonald, A. H.; Schiffer, P.; Samarth, N. *Nat. Mater.* **2005**, *4*, 195-202.
10. Dietl, T. *Nat. Mater.* **2010**, *9*, 965-974.

11. Selinsky, R. S.; Keavney, D. J.; Bierman, M. J.; Jin, S. *Appl. Phys. Lett.* **2009**, *95*, 202501/1-202501/3.
12. Selinsky, R. S.; Han, J. H.; Morales, P. E. A.; Guzei, I. A.; Jin, S. *J Am Chem Soc* **2010**, *132*, 15997-6005.
13. Bierman, M. J.; Van Heuvelen, K. M.; Schmeisser, D.; Brunold, T. C.; Jin, S. *Adv. Mater.* **2007**, *19*, 2677-2681.
14. Song, Y.; Schmitt, A. L.; Jin, S. *Nano Lett.* **2008**, *8*, 2356-2361.
15. Maex, K.; Van Rossum, M., *Properties of Metal Silicides*. INSPEC, the Institution of Electrical Engineers: London: UK, 1995.
16. Manyala, N.; Sidis, Y.; DiTusa, J. F.; Aeppli, G.; Young, D. P.; Fisk, Z. *Nature* **2000**, *404*, 581-584.
17. Guevara, J.; Vildosola, V.; Milano, J.; Llois, A. M. *Phys. Rev. B* **2004**, *69*, 184422/1-184422/6.
18. Manyala, N.; Sidis, Y.; Ditusa, J. F.; Aeppli, G.; Young, D. P.; Fisk, Z. *Nat. Mater.* **2004**, *3*, 255-262.
19. Lu, W.; Lieber, C. M. *Nat. Mater.* **2007**, *6*, 841-850.
20. Higgins, J. M.; Ding, R.; De Grave, J. P.; Jin, S. *Nano Lett.* **2010**, *10*, 1605-1610.
21. Yu, X. Z.; Onose, Y.; Kanazawa, N.; Park, J. H.; Han, J. H.; Matsui, Y.; Nagaosa, N.; Tokura, Y. *Nature* **2010**, *465*, 901-904.
22. Liu, E. S.; Nah, J.; Varahramyan, K. M.; Tutuc, E. *Nano Lett.* **2010**, *10*, 3297-3301.
23. Lin, Y.-C.; Chen, Y.; Shailos, A.; Huang, Y. *Nano Lett.* **2010**, *10*, 2281-2287.

24. Soulen, R. J., Jr.; Byers, J. M.; Osofosky, M. S.; Nadgorny, B.; Ambrose, T.; Cheng, S. F.; Broussard, P. R.; Tanaka, C. T.; Nowak, J.; Moodera, J. S.; Barry, A.; Coey, J. M. D. *Science* **1998**, *282*, 85-88.
25. Meservey, R.; Tedrow, P. M.; Fulde, P. *Phys. Rev. Lett.* **1970**, *25*, 1270-2.
26. Meservey, R.; Tedrow, P. M. *Phys. Rep.* **1994**, *283*, 173-243.
27. Upadhyay, S. K.; Palanisami, A.; Louie, R. N.; Buhrman, R. A. *Phys. Rev. Lett.* **1998**, *81*, 3247-3250.
28. Strijkers, G. J.; Ji, Y.; Yang, F. Y.; Chien, C. L.; Byers, J. M. *Phys. Rev. B* **2001**, *63*, 104510/1-104510/6.
29. Ji, Y.; Strijkers, G. J.; Yang, F. Y.; Chien, C. L.; Byers, J. M.; Anguelouch, A.; Xiao, G.; Gupta, A. *Phys. Rev. Lett.* **2001**, *86*, 5585-5588.
30. Anguelouch, A.; Gupta, A.; Xiao, G.; Abraham, D. W.; Ji, Y.; Ingvarsson, S.; Chien, C. L. *Phys. Rev. B* **2001**, *64*, 180408/1-180408/3.
31. Braden, J. G.; Parker, J. S.; Xiong, P.; Chun, S. H.; Samarth, N. *Phys. Rev. Lett.* **2003**, *91*, 056602/1-056602/4.
32. Schmitt, A. L.; Higgins, J. M.; Jin, S. *Nano Lett.* **2008**, *8*, 810-815.
33. Higgins, J. M.; Carmichael, P.; Schmitt, A. L.; Lee, S.; DeGrave, J. P.; Jin, S. *ACS Nano* **2011**, *5*, 3268-3277.
34. Seidman, D. N.; Stiller, K. *MRS Bull.* **2009**, *34*, 717-724.
35. Miller, M. K., *Atom Probe Tomography: Analysis at the Atomic Level*. Kluwer Academic/Plenum Publishers: New York, 2000.
36. Kelly, T. F.; Larson, D. J.; Thompson, K.; Alvis, R. L.; Bunton, J. H.; Olson, J. D.; Gorman, B. P. *Annu. Rev. Mater. Res.* **2007**, *37*, 681-727.

37. Perea, D. E.; Hemesath, E. R.; Schwalbach, E. J.; Lensch-Falk, J. L.; Voorhees, P. W.; Lauhon, L. J. *Nature Nanotech.* **2009**, *4*, 315-319.
38. Miller, M. K.; Russell, K. F.; Thompson, G. B. *Ultramicroscopy* **2005**, *102*, 287-298.
39. Larson, D. J.; Cerezo, A.; Clifton, P. H.; Petford-Long, A. K.; Martens, R. L.; Kelly, T. F.; Tabat, N. *J. Appl. Phys.* **2001**, *89*, 7517-7521.
40. Larson, D. J. *Thin Solid Films* **2006**, *505*, 16-21.
41. Perea, D. E.; Allen, J. E.; May, S. J.; Wessels, B. W.; Seidman, D. N.; Lauhon, L. J. *Nano Lett.* **2006**, *6*, 181-185.
42. Perea, D. E.; Lensch, J. L.; May, S. J.; Wessels, B. W.; Lauhon, L. J. *Appl. Phys. A-Mater.* **2006**, *85*, 271-275.
43. Perea, D. E.; Wijaya, E.; Lensch-Falk, J. L.; Hemesath, E. R.; Lauhon, L. J. *J. Solid State Chem.* **2008**, *181*, 1642-1649.
44. Stavitski, E.; de Groot, F. M. F. *Micron* **2010**, *41*, 687-694.
45. Ishimoto, K.; Ohashi, M.; Yamauchi, H.; Yamaguchi, Y. *J. Phys. Soc. Jpn.* **1992**, *61*, 2503-2511.
46. Schmitt, A. L.; Zhu, L.; Schmeier, D.; Himpsel, F. J.; Jin, S. *J. Phys. Chem. B* **2006**, *110*, 18142-18146.
47. Schmitt, A. L.; Bierman, M. J.; Schmeisser, D.; Himpsel, F. J.; Jin, S. *Nano Lett.* **2006**, *6*, 1617-1621.
48. Onose, Y.; Takeshita, N.; Terakura, C.; Takagi, H.; Tokura, Y. *Phys. Rev. B* **2005**, *72*, 224431/1-224431/12.
49. Woods, G. T.; Soulen, R. J., Jr.; Mazin, I.; Nadgorny, B.; Osofsky, M. S.; Sanders, J.; Srikanth, H.; Egelhoff, W. F.; Datla, R. *Phys. Rev. B* **2004**, *70*, 054416/1-054416/8.

50. Rigato, F.; Piano, S.; Foerster, M.; Giubileo, F.; Cucolo, A. M.; Fontcuberta, J. *Phys. Rev. B* **2010**, *81*, 174415/1-174415/6.
51. Chalsani, P.; Upadhyay, S. K.; Ozatay, O.; Buhrman, R. A. *Phys. Rev. B* **2007**, *75*, 094417/1-094417/16.

CHAPTER 3

Observation of the Magnetic Skyrmion Lattice in a MnSi Nanowire by Lorentz TEM*

3.1 Abstract

We report here the real-space observation of skyrmions and helical magnetic domains in a MnSi nanowire (NW) using Lorentz transmission electron microscopy (LTEM). The MnSi NW was thinned to a rectangular cross-section by focused-ion beam milling to reduce obstructive Fresnel fringes. Helimagnetic domains, imaged as alternating bright and dark contrast stripes with an 18 nm period were observed to be the spontaneous magnetic ground state at 6 K, while the hexagonal skyrmion lattice (SkX) with a domain diameter of 18 nm was observed under a normal magnetic field of 210 mT. Temperature dependent measurements reveal that the SkX is stable over a larger range in this NW system (6 K – 35 K) compared to the narrow temperature regime of skyrmion phase in bulk MnSi (26 - 30 K) and thin films of MnSi (5 - 23 K).

* This chapter was published in *Nano Lett.*, **2013**, *13* (8), pp 3755–3759. The manuscript and experiments were completed in collaboration with X. Yu, and Y. Tokura of RIKEN Center for Emergent Matter Science (CEMS) and the University of Tokyo, Department of Applied Physics and Quantum-Phase Electronics Center (QPEC). Y. Hara and T. Hara from Electron Microscopy Group at the National Institute for Materials Science (NIMS) performed FIB sample preparation. S. Jin from University of Wisconsin-Madison, USA contributed to the writing of the manuscript. The initial observations were performed by X. Yu and J. DeGrave, and were completed by X. Yu.

3.2 Introduction

Magnetic domain walls in ferromagnetic nanomaterials such as permalloy nanowires (NWs) can be manipulated by applied currents through the spin transfer torque mechanism, a concept of interest for nonvolatile memory devices, especially the magnetic racetrack design.¹⁻³ However, a large current density is required to translate magnetic domains in ferromagnetic materials, typically higher than 10^5 A/cm², inducing a large Joule heating effect causing the NW devices to breakdown. A promising alternative to these NW ferromagnetic domain wall devices is the class of chiral B20-type helimagnets such as FeGe and MnSi.⁴⁻⁸ Bulk cubic chiral magnetic compounds order into a magnetic skyrmion crystal (SkX) phase when a small magnetic field is applied perpendicular to the helical propagation vector.⁹ Magnetic skyrmions are topologically nontrivial vortex-like magnetic configurations with the periphery spins aligned antiparallel to central spin direction, and they vary in size according to the competing Dzyaloshinskii-Moriya and ferromagnetic exchange interactions. Furthermore, these skyrmions are mobile at remarkably low current densities ($\sim 10^2$ A/cm²).^{6, 9-13} Magnetic skyrmion domains in bulk crystals have been imaged in reciprocal space using small-angle neutron scattering experiments¹⁴⁻¹⁶ and also in thin films using the real-space imaging technique of Lorentz transmission electron microscopy (LTEM).^{5, 12, 17-19} Together, these techniques have revealed skyrmion domain diameters ranging from 90 nm down to 18 nm.^{5, 16, 19}

If these magnetic skyrmions are to be useful for magnetic storage devices, the properties of the SkX confined to nanometer dimensions must be understood.²⁰ B20 silicide nanowires are an attractive system for studying these confinement effects because they can act as a quasi-1D system for magnetic skyrmions, provide a natural extension to the racetrack memory concept,

and moreover, several bottom-up syntheses have been previously developed.²¹⁻²⁴ Initial magnetotransport studies of the helimagnetic phase in MnSi NWs suggest a small increase in T_c compared to bulk.²⁴ The magnetic SkX has been observed so far in bulk MnSi via SANS⁹ and in thin film samples using LTEM,¹⁸ and investigated also by topological Hall effect measurements for both bulk²⁵ and thin film.²⁶ In bulk MnSi, the SkX exists only in a very small temperature window (26 – 29.5 K) with a small applied magnetic field (~250 mT), however, the thin film morphology was shown to stabilize the SkX over a much larger temperature region (6 – 23 K).¹⁸ The increased temperature window for SkX clearly demonstrates that it is possible to stabilize the skyrmion phase in helimagnets with noncentrosymmetric cubic structure by reducing sample dimensions.^{5, 19, 27, 28} We attempt to further extend the understanding of confinement effects on SkX using the Lorentz TEM technique to observe MnSi NWs that can be considered a quasi-1D helimagnetic system when the diameter of the NW approaches the magnetic skyrmion diameter or skyrmion lattice constant. Such a NW system is attractive for demonstrating the controlled motion of skyrmions by the spin-transfer torque mechanism. However, the NW system presents several challenges in the LTEM observation compared to bulk and thin film morphologies due to the nanoscale dimensions and the obstructive Fresnel fringes. We therefore shaped the NW into a rectangular geometry and thinned the NW via focused-ion beam milling to allow LTEM observation.

3.3 Results and Discussion

MnSi NWs were grown in a chemical vapor deposition system by vaporizing MnCl_2 and transporting it downstream with inert gas flow to a Si (100) substrate with native SiO_2 , as previously reported.²⁴ The as-grown NWs were then thinned using a focused-ion beam (FIB)

equipped with a scanning electron microscope (SEM). First, NWs with large diameter (> 200 nm) were picked up by a micromanipulator probe and then fixed to a sample carrier by depositing W at the base of the NW and sample carrier. Once affixed to the holder, these NWs were further thinned along the transverse direction by FIB (FIB-SEM: SMF1000, Hitachi High-Tech Science Corporation) milling to produce a rectangular plate shape with uniform thickness down the axis of the NW, drastically reducing the obstructive Fresnel fringes otherwise observed in unmodified NWs via LTEM. To clean up the damaged layer and resputtered materials and obtain a clean flat nanoband sample we used low-energy Ar ion milling (NanoMill: Model 1040, Fischione Instruments). The crystallographic orientation of the NWs was determined by selected-area electron diffraction (SAED) and the magnetic domain structure was determined using Lorentz TEM (JEM-2100F) with a liquid-He cooled sample holder capable of controlling temperature from 6 K up to room temperature. Magnetic fields were applied in the microscope by adjusting the objective lens current. The real-space magnetic domain structure is obtained by viewing the sample in an overfocused and underfocused plane, and the in-plane magnetic component is observed to have opposite contrast in these two images while the infocus image should have uniform contrast. The under- and overfocused images are analyzed with the transport-of-intensity (TIE) equation using the QPt software package (HREM Co.) to obtain the in-plane magnetic component map of the sample.^{5, 19}

Two MnSi NWs with rhombohedra cross-sections shaped into a rectangular geometry by SEM-FIB are shown in Figure 3.1. Figure 3.1b shows a magnified view of the NW viewed by infocus LTEM that shows uniform contrast, indicating a flat sample surface without significant shape irregularity which is important for observing the magnetic contrast. The thinned NWs had an approximate thickness of 50 nm and widths of about 200 nm. The fraction of magnetically

dead layer was estimated to be less than 10% of the total NW thickness. The SAED pattern indicates that the (110) crystallographic plane is perpendicular to the incident electron beam.

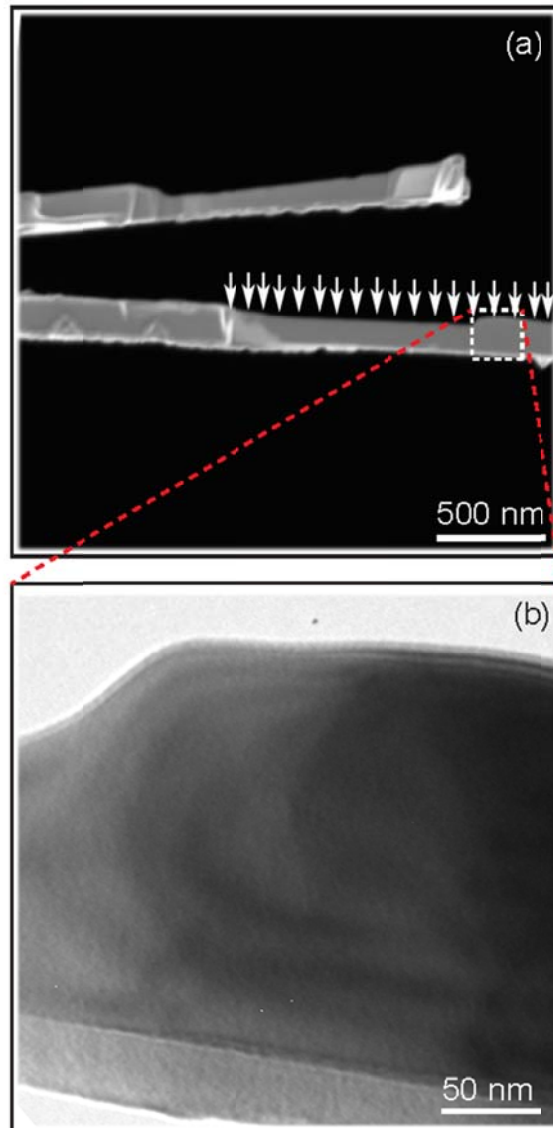


Figure 3.1. MnSi NW sample thinned by a scanning electron microscope – focused-ion beam instrument (SEM-FIB). (a) SEM image of two MnSi NWs thinned using FIB-SEM. White arrows indicate the direction of irradiated Ga ion beam. (b) Transmission electron microscopy (TEM) image of the highlighted portion of the MnSi NW shown in (a).

The spontaneous magnetic configuration of the MnSi NW sample at 6 K is shown in Figure 3.2. An intermittent stripe pattern is observed in the defocused LTEM images: underfocus in Figure 3.2a and overfocus in Figure 3.2b. However, the intermittent stripe contrast only extends from the bottom edge of the NW to roughly 100 nm from the top edge. In order to more clearly observe the magnetic stripe domain structure, the background noise is removed by first obtaining the FFT of the boxed region shown in Figure 3.2a and then applying masks on the two main reflection spots in the FFT pattern (indicated by circles in Figure 3.2c). The image is then reconstructed with the applied masks to obtain the image in Figure 3.2d, clearly showing the alternating bright and dark contrast lines that are indicative of the helical magnetic order in the spontaneous (zero-field cooled) ground state. The period of the helical structure is approximately 18 nm and is along the [110] direction which is also the growth axis of the MnSi NW, in contrast to the preferred helimagnetic [111] direction in bulk MnSi.⁹

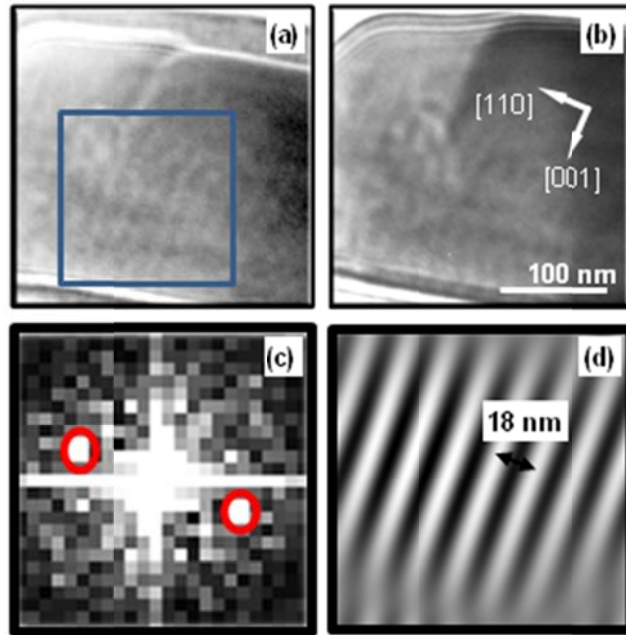


Figure 3.2 Spontaneous striped magnetic configuration of a thinned MnSi NW observed using LTEM on the highlighted area shown in Figure 3.1b. (a) Underfocused and (b) overfocused image planes at 6 K. (c) Fast Fourier transform (FFT) pattern of the region highlighted by the blue square in (a). (d) Reconstructed LTEM image from the inverse FFT after applying masks on the two reflections circled by red open circles in (c).

A magnetic field of 210 mT was then applied perpendicularly to the [110] sample axis between the temperatures of 6 and 40 K, and representative under- and overfocused images are shown in Figures 3a, b respectively. The contrast observed with the applied magnetic field shows an array of dots, significantly different from that observed for the ground state striped structure. The contrast is weak, but the light contrast dots in the underfocused image (Figure 3.3a) are clearly inverted to dark contrast for the overfocused image (Figure 3.3b). Moreover, the array of dots is not observed for the infocus image proving their magnetic origin. We attribute these dots to the formation of the magnetic SkX phase in this MnSi NW. Interestingly, this array of dots is observed to extend over the full length of the observed NW section which was not the case for the striped ground state magnetic domain structure, as noted above for Figures 3.2a,b. The upper-left insets of Figures 3.3a,b show the FFTs of the boxed regions, and a clear six-fold symmetry is observed, consistent with the hexagonal symmetry of the SkX. Similar to the analysis of the FFT for the helical domain structure, masks are applied to the 6-fold symmetrical reflections and the resulting inverted FFT is shown in the lower left insets of Figures 3.3a,b. The magnetic TIE equation was used to analyze the under- and overfocused images to obtain the in-plane magnetic component map of the magnetic skyrmions as shown in Figure 3.3c with colors and white arrows indicating the inplane magnetization. The dark regions in Figure 3.3c observed at the core and periphery of the magnetic skyrmions indicate an out of plane magnetization, thus we assume the periphery aligns with the applied field and the core of the skyrmion is antiparallel to this direction.¹⁹ The chirality of the skyrmion domains was observed to be left-handed across the whole of the observed NW region, and the skyrmions size or SkX lattice constant is roughly 18 nm which corresponds to the helimagnetic pitch. Moreover, the SkX is observed to collapse in some local regions. These could be caused by the residual domains of helimagnetic structure,

but it is more likely that these are artifacts of the image analysis caused by localized areas with exceptionally weak contrast.

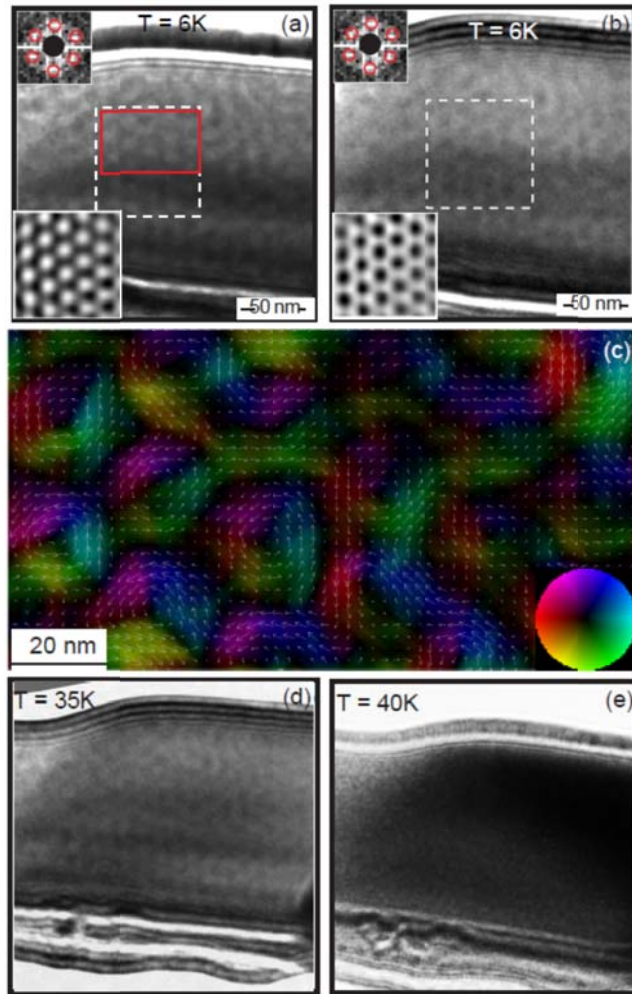


Figure 3.3. Magnetic configurations and corresponding spin texture in a normal magnetic field of 210 mT. (a) Underfocused and (b) overfocused images at 6 K. Insets at left bottoms of (a) and (b) are the reconstructed images of the boxed areas, which were produced from the inverse FFT with masks applied on the six-fold symmetric reflections shown in the upper left insets of (a) and (b). (c) In-plane magnetic component map of the skyrmions for the red highlighted area in (a). Colors and white arrows indicate the magnitude and direction of the in-plane component. (See the color wheel in the corner.) Dark color indicates zero in-plane and hence strong out-of-plane component. (d)-(e) Underfocused Lorentz TEM images of the same region at 35 K and 40 K.

In addition to observing the formation of the SkX under the effects of applied magnetic fields, we investigated the temperature dependence. The contrast intensity of the SkX was observed to decrease with increasing temperature. The skyrmion magnetic contrast is barely observable up to 35 K (see Figure 3.3d), but completely disappears above 35 K, as revealed by a uniform contrast in the over- and underfocused images (Figure 3.3e) for a temperature of 40 K and applied magnetic field of 210 mT. This indicates that the critical magnetic ordering temperature for the thinned MnSi NWs is approximately 35 K. Summarizing all of the LTEM experiments at different temperatures and applied magnetic fields, we construct an approximate temperature-magnetic field phase diagram for the thinned MnSi NW system as displayed in Figure 3.4. It is clear that the skyrmion phase is further stabilized in this thinned MnSi NW system compared to both bulk (Figure 3.4a) and thin film (Figure 3.4b).

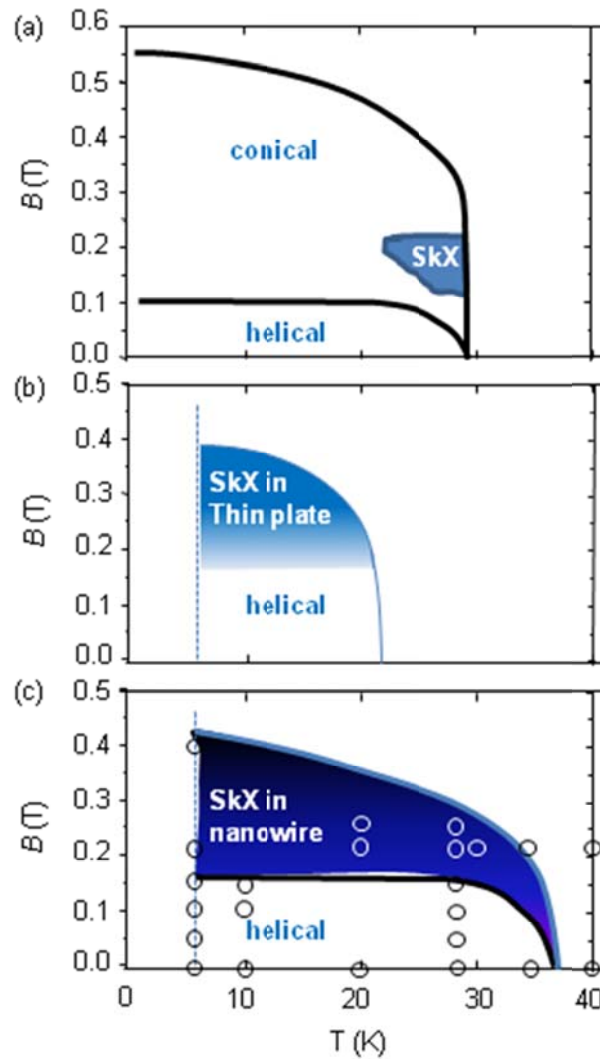


Figure 3.4. Magnetic field versus temperature phase diagrams for various MnSi morphologies. (a) Schematic of magnetic phase diagram in bulk MnSi,⁹ (b) thin film MnSi¹⁸ and (c) a MnSi NW (this work). SkX stands for the skyrmion phase. Open circles show the LTEM data for a MnSi NW.

Several theoretical and experimental reports predict that the critical ordering temperature is strongly affected by finite size effects in NWs.²⁹⁻³² Geometrical confinement hinders the formation of a conical phase in chiral B20 magnets and the SkX becomes the favored phase. Additionally, the skyrmion phase can be stabilized by anisotropic effects such as strain.^{33, 34} Further experimental evidence of these stabilization effects has been demonstrated for a variety of B20 systems including MnSi NWs by magnetoresistance measurements,²⁴ strained MnSi thin films using magnetic susceptibility measurements,^{28, 35, 36} thin films of MnSi,¹⁸ Fe_{0.5}Co_{0.5}Si,¹⁹ and FeGe⁵ by LTEM observations, as well as topological Hall effect measurements in thin films of FeGe²⁸ and MnSi.²⁶ Furthermore, it was suggested that the finite size effect might actually reduce T_c for a NW system due to the decreased correlation length of magnetic interactions when the sample dimensions are reduced,³¹ however, the strain caused by defects induced either by the FIB thinning process or inherent to the as-grown NWs could also affect T_c . Therefore, we expect both the finite size and strain effects to play a significant role in the observed change in T_c for the thinned NW observed here. On the other hand, the experimental observations as shown in Figure 3.4c indicate that the skyrmion phase was stabilized in this quasi-1D system, compared with the 2D thin plate and 3D bulk sample. The increase of width of a NW may change the system to quasi-2D and reduce transition temperature of SkX, while the increase of thickness of a NW may destabilize the skyrmion formation as in the case of the quasi-2D system.⁵

3.4 Conclusion

In conclusion, using the Lorentz TEM technique, we have successfully realized helimagnetic and magnetic skyrmion domains in thinned MnSi NWs with an observed periodicity and domain size of 18 nm. The magnetic SkX was stabilized in a larger temperature window with an

increased T_c (35 K) compared to both bulk (30 K) and thin film (22 K) samples of MnSi. These results demonstrate that SkX formation is not hindered by thinning the MnSi NW using FIB, a technique known to cause partial damage to the fabricated structures. Moreover, our results demonstrate the enhanced robustness of the skyrmion phase that can be achieved by reducing the dimensions of the system. Therefore, NWs of the noncentrosymmetric B20 chiral magnets, such as MnSi^{23, 24, 37} and Fe_{1-x}Co_xSi,³⁸ are extremely interesting for the manipulation of skyrmions by applied currents and for future magnetic storage technologies.

3.5 Author Contributions

X.Y. designed the experiments, performed the Lorentz TEM observations, and analyzed the Lorentz TEM data. J. P. D. and S.J. synthesized the nanowire. Y. H. and T. H. fabricated the nanowire by using SEM-FIB. S.J. and Y.T. conceived the project. X.Y., J.P.D., S.J., and Y.T. wrote the draft. All authors discussed the data and commented on the manuscript.

3.6 Acknowledgements

We are grateful to RIKEN CEMS materials characterization support unit for providing a transmission electron microscope (JEM2100F). We would like to thank T. Kikitsu (RIKEN), W.Z. Zhang (NIMS), M. Nagao (NIMS), K. Kimoto (NIMS), and K. Shibata (Univ. of Tokyo) for helpful discussion. This work was supported by the Funding Program for World-Leading Innovative R&D on Science and Technology on “Quantum Science on Strong Correlation” and by JSPS Grant-in-Aid for Scientific Research(S) No. 24224009. J.P.D. and S.J. are supported by a US NSF grant (ECCS-1231916). J.P.D. would also like to thank NSF and JSPS for jointly funding a fellowship partially supporting this collaboration through the EAPSI program.

3.7 References

1. Hayashi, M.; Thomas, L.; Moriya, R.; Rettner, C.; Parkin, S. *Science* **2008**, *320*, 209-211.
2. Hayashi, M.; Thomas, L.; Rettner, C.; Moriya, R.; Jiang, X.; Parkin, S. S. P. *Phys. Rev. Lett.* **2006**, *97*, 207205/1-207205/4.
3. Parkin, S. S. P.; Hayashi, M.; Thomas, L. *Science* **2008**, *320*, 190-194.
4. Brataas, A.; Bauer, G. E. W.; Kelly, P. J. *Phys. Rep.* **2006**, *427*, 157-255.
5. Yu, X. Z.; Kanazawa, N.; Onose, Y.; Kimoto, K.; Zhang, W. Z.; Ishiwata, S.; Matsui, Y.; Tokura, Y. *Nature Mater.* **2011**, *10*, 106-109.
6. Yu, X. Z.; Kanazawa, N.; Zhang, W. Z.; Nagai, T.; Hara, T.; Kimoto, K.; Matsui, Y.; Onose, Y.; Tokura, Y. *Nat. Commun.* **2012**, *3*, 988.
7. Kiselev, N. S.; Bogdanov, A. N.; Schafer, R.; Rossler, U. K. *J. Phys. D: Appl. Phys.* **2011**, *44*, 392001-1/392001-4.
8. Fert, A.; Cros, V.; Sampaio, J. *Nat. Nanotechnol.* **2013**, *8*, 152-156.
9. Jonietz, F.; Muehlbauer, S.; Pfleiderer, C.; Neubauer, A.; Munzer, W.; Bauer, A.; Adams, T.; Georgii, R.; Boni, P.; Duine, R. A.; Everschor, K.; Garst, M.; Rosch, A. *Science* **2010**, *330*, 1648-1651.
10. Schulz, T.; Ritz, R.; Bauer, A.; Halder, M.; Wagner, M.; Franz, C.; Pfleiderer, C.; Everschor, K.; Garst, M.; Rosch, A. *Nat. Phys.* **2012**, *8*, 301-304.
11. Everschor, K.; Garst, M.; Binz, B.; Jonietz, F.; Muehlbauer, S.; Pfleiderer, C.; Rosch, A. *Phys. Rev. B* **2012**, *86*, 054432/1-054432/11.
12. Seki, S.; Yu, X. Z.; Ishiwata, S.; Tokura, Y. *Science* **2012**, *336*, 198-201.
13. Iwasaki, J.; Mochizuki, M.; Nagaosa, N. *Nat. Commun.* **2013**, *4*, 1463.

14. Kanazawa, N.; Kim, J. H.; Inosov, D. S.; White, J. S.; Egetenmeyer, N.; Gavilano, J. L.; Ishiwata, S.; Onose, Y.; Arima, T.; Keimer, B.; Tokura, Y. *Phys. Rev. B* **2012**, *86*, 134425/1-134425/7.
15. Pfleiderer, C.; Adams, T.; Bauer, A.; Biberacher, W.; Binz, B.; Birkelbach, F.; Boni, P.; Franz, C.; Georgii, R.; Janoschek, M.; Jonietz, F.; Keller, T.; Ritz, R.; Muhlbauer, S.; Munzer, W.; Neubauer, A.; Pedersen, B.; Rosch, A. *J. Phys. Cond. Mat.* **2010**, *22*, 164207-1/164207-7.
16. Muhlbauer, S.; Binz, B.; Jonietz, F.; Pfleiderer, C.; Rosch, A.; Neubauer, A.; Georgii, R.; Boni, P. *Science* **2009**, *323*, 915-919.
17. Yu, X. Z.; Mostovoy, M.; Tokunaga, Y.; Zhang, W. Z.; Kimoto, K.; Matsui, Y.; Kaneko, Y.; Nagaosa, N.; Tokura, Y. *Proc. Natl. Acad. Sci.* **2012**, 1-5, 5 pp.
18. Tonomura, A.; Yu, X. Z.; Yanagisawa, K.; Matsuda, T.; Onose, Y.; Kanazawa, N.; Park, H. S.; Tokura, Y. *Nano Lett.* **2012**, 1673–1677.
19. Yu, X. Z.; Onose, Y.; Kanazawa, N.; Park, J. H.; Han, J. H.; Matsui, Y.; Nagaosa, N.; Tokura, Y. *Nature* **2010**, *465*, 901-904.
20. Zang, J. D.; Mostovoy, M.; Han, J. H.; Nagaosa, N. *Phys. Rev. Lett.* **2011**, *107*, 136804/1-136804/5.
21. Schmitt, A. L.; Higgins, J. M.; Jin, S. *Nano Lett.* **2008**, *8*, 810-815.
22. Schmitt, A. L.; Higgins, J. M.; Szczech, J. R.; Jin, S. *J. Mater. Chem.* **2010**, *20*, 223-235.
23. Higgins, J. M.; Carmichael, P.; Schmitt, A. L.; Lee, S.; DeGrave, J. P.; Jin, S. *ACS Nano* **2011**, *5*, 3268-3277.
24. Higgins, J. M.; Ding, R.; DeGrave, J. P.; Jin, S. *Nano Letters* **2010**, *10*, 1605-1610.

25. Neubauer, A.; Pfleiderer, C.; Binz, B.; Rosch, A.; Ritz, R.; Niklowitz, P. G.; Boni, P. *Phys. Rev. Lett.* **2009**, *102*, 186602-1/186602-4.
26. Li, Y.; Kanazawa, N.; Yu, X. Z.; Tsukazaki, A.; Kawasaki, M.; Ichikawa, M.; Jin, X. F.; Kagawa, F.; Tokura, Y. *Phys. Rev. Lett.* **2013**, *110*, 117202/1-117202/5.
27. Yi, S. D.; Onoda, S.; Nagaosa, N.; Han, J. H. *Phys. Rev. B* **2009**, *80*.
28. Huang, S. X.; Chien, C. L. *Phys. Rev. Lett.* **2012**, *108*, 267201/1-267201/5.
29. Zhang, R.; Willis, R. F. *Phys. Rev. Lett.* **2001**, *86*, 2665-2668.
30. Croitoru, M. D.; Shanenko, A. A.; Peeters, F. M. *Phys. Rev. B* **2007**, *76*, 024511/1-024511/6.
31. Sun, L.; Searson, P. C.; Chien, C. L. *Phys. Rev. B* **2000**, *61*, R6463-R6466.
32. Fisher, M. E.; Barber, M. N. *Phys. Rev. Lett.* **1972**, *28*, 1516-1519.
33. Wilson, M. N.; Karhu, E. A.; Quigley, A. S.; Rossler, U. K.; Butenko, A. B.; Bogdanov, A. N.; Robertson, M. D.; Monchesky, T. L. *Phys. Rev. B* **2012**, *86*, 144420/1-144420/6.
34. Butenko, A. B.; Leonov, A. A.; Rossler, U. K.; Bogdanov, A. N. *Phys. Rev. B* **2010**, *82*, 052403-1/052403-4.
35. Magnano, E.; Bondino, F.; Cepek, C.; Parmigiani, F.; Mozzati, M. C. *Appl. Phys. Lett.* **2010**, *96*, 152503/1-152503/3.
36. Karhu, E.; Kahwaji, S.; Monchesky, T. L.; Parsons, C.; Robertson, M. D.; Maunders, C. *Phys. Rev. B* **2010**, *82*, 184417/1-184417/11.
37. Yi, S. D.; Onoda, S.; Nagaosa, N.; Han, J. H. *Physical Review B* **2009**, *80*.
38. DeGrave, J. P.; Schmitt, A. L.; Selinsky, R. S.; Higgins, J. M.; Keavney, D. J.; Jin, S. *Nano Lett.* **2011**, *11*, 4431-4437.

CHAPTER 4

A General Method to Measure the Hall Effect in Nanowires:

*Examples of FeS₂ and MnSi**

4.1 Abstract.

We present a general methodology for measuring the Hall effect on nanostructures with one-dimensional (1D) nanowire morphology. Relying only on typical e-beam lithography, the methodology developed herein utilizes an angled electrode evaporation technique so that the nanowire itself is a shadow mask and an intimate sidewall contact can be formed for the Hall electrodes. A six-contact electrode scheme with offset transverse contacts is utilized that allows monitoring of both the longitudinal resistivity and the Hall resistivity which is extracted from the raw voltage from the transverse electrodes using an antisymmetrization procedure. Our method does not require the use of a highly engineered lithographic process to produce directly opposing Hall electrodes with a very small gap. Hall effect measurements on semiconducting iron pyrite (FeS₂) nanowire devices are validated by comparing to Hall effect measurements in the conventional Hall geometry using FeS₂ plate devices. This Hall effect measurement is further extended to MnSi nanowires, and the distinct anomalous Hall effect signature is identified for the first time in chiral magnetic MnSi nanowires, a significant step towards identifying the topological Hall effect due to skyrmions in chiral magnetic nanowires.

* This chapter was published in *Nano Lett.*, **2013**, *13* (6), pp 2704–2709 and was co-authored by D. Liang and S. Jin of the University of Wisconsin-Madison.

4.2 Introduction

Hall effect measurements have been used to reveal fundamental solid state physical phenomena since the initial discovery of the conventional Hall effect in 1879.¹ In a conventional Hall effect measurement a magnetic field is applied perpendicular to the plane of the electrical current imparting a Lorentz force on the charge carriers which preferentially deflects them to one side of the device and a transverse electric field develops known as the Hall field. Carrier type, concentration, and mobility are commonly extracted from Hall measurements in semiconductors. Hall effect measurements led to the discoveries of integer and fractional quantum Hall effects in two-dimensional (2D) electron systems.^{2, 3} Recently, Hall measurements have been extended to study a wide variety of strongly correlated materials such as ferromagnets (anomalous Hall effect),⁴ chiral magnets (topological Hall effect and Skyrmion Hall effect),⁵⁻⁹ and topological insulators (integer quantum Hall effect).^{10, 11} Furthermore, it is very interesting to study these materials in the nanotechnology paradigm to exploit confinement effects due to the reduction of physical dimensions of the system, such as in one-dimensional (1D) nanowires (NWs).¹²

Therefore, there is a strong motivation to extend Hall effect measurements to NWs since many NW materials are being vetted for possible advantageous properties across a variety of fields such as solar energy,¹³⁻¹⁶ nanoelectronics,^{17, 18} optoelectronics,¹⁹⁻²¹ spintronics,²²⁻²⁶ thermoelectrics,²⁷⁻²⁹ and the recently discovered topological insulators.^{11, 30-32} Not only are NWs an interesting platform for studying fundamental effects of geometrical confinement, but also they often offer advantages in applications. For example, the separation of charge carriers can be improved by 1D morphology in semiconductors,^{15, 16} and the helical magnetic phase is stabilized in MnSi NWs in an extended temperature range compared to the bulk due to the reduced dimension and NW geometry.^{5, 33-36} For topological insulator materials the increased surface area

to volume ratio in NW geometries physically limits the unwanted bulk conduction contribution to transport properties, therefore, Hall effect measurements on such NW topological insulators can help to confirm the metallic surface states by measuring an integer quantum Hall effect.^{11, 30,}

³¹ However, NWs have been especially resistant to Hall effect measurement techniques due to the prohibitive 1D geometry. Carrier properties in semiconductor NW systems instead have been probed with other methods such as transconductance measurements in field-effect device geometries (often requiring modeling assumptions to be made to extract the carrier properties)^{17,}
^{37, 38} and thermoelectric measurements.²⁷⁻²⁹

Recently, two groups have succeeded in measuring the induced Hall field of a NW device.^{39,}
⁴⁰ Both of these NW device experiments require a highly engineered lithographic process that utilizes highly accurate and well-resolved e-beam lithography patterning to precisely position electrodes that only contact the NW on one sidewall facet and are separated by a distance of less than roughly 100 nm across the top NW facet. Such high accuracy lithographic patterning demands highly specialized equipment and is a low through-put experiment. A facile, high-throughput and general method that accurately measures the Hall effect is desired for NWs so that relevant transport properties can be obtained and statistics can be collected from many different devices.

Here we demonstrate a general method for the fabrication of Hall effect devices and making Hall measurements for NW morphology that utilizes conventional electron beam lithography and metal deposition techniques to create intimate sidewall contact with a variety of well-faceted NW cross-section shapes and sizes. We demonstrate the successful measurement of the Hall field in semiconducting FeS₂ NWs with square cross-section and compare this to conventional Hall devices of FeS₂ nanoplates to validate this method. We then extend the technique to NWs

of chiral magnetic MnSi and demonstrate the first observation of anomalous Hall effect in MnSi NWs. This facile method is widely extendable to NWs of many different materials and cross-section geometries by small adjustments to the procedures outline here.

4.3 Results and Discussion

We first chose NWs of semiconducting iron pyrite (FeS_2) as the model system to demonstrate the Hall measurement, not only because FeS_2 NWs are of current interest to solar energy conversion^{41, 42} and it is important to understand its semiconducting properties, but also because FeS_2 NWs, nanorods, and nanoplates can be obtained via a single synthesis, as reported previously.⁴² The coexistence of 1D and plate morphologies would allow the comparison of the NW Hall measurement with the conventional Hall measurements using FeS_2 nanoplates. The synthesized pyrite nanostructures were dry-transferred to a Si/SiO₂ (600 nm) substrate by gently brushing the growth substrate across the SiO₂ layer which generates a preferential alignment of the anisotropic nanostructures. Next, in a critical step illustrated in Figure 4.1a, an insulating Al₂O₃ layer is deposited onto the sample at an angle of $\Theta = 0^\circ$ (i.e. the incident angle of deposited material is perpendicular to the plane of the device substrate). The experimental details of the device fabrication process are discussed in Appendix 2. Carefully tailoring the thickness of insulating Al₂O₃ leaves the sides of the NW exposed and insulates the top of the device to prevent shorting the Hall field even though the final Hall device electrodes cross the top of the NW (see Figure 4.1e). We determine the thickness of Al₂O₃ required by considering both the thickness of the nanostructure and the required HF etching time to make Ohmic contact to the material because the buffered HF solution will etch both the insulating Al₂O₃ layer (albeit very slowly) and the intended contact surface. We suggest that the final thickness of insulating

layer should be at least 10 nm to safely prevent the transverse field from shorting out. If the alumina layer is completely removed due to wet etching, the transverse field will be shorted and the detected Hall voltage is observed to oscillate about zero. Two example devices intentionally fabricated without the insulating alumina layer are shown in Appendix 2 to illustrate this effect (Figure A2.1). Additionally, if the nanostructure is too small, it will not be possible to deposit a thick enough insulating layer to prevent shorting the Hall voltage while also leaving the sidewalls of the NW exposed for contact deposition. We suggest that this limit will occur for NWs less than 40 nm thick for e-beam deposited Al_2O_3 used here.

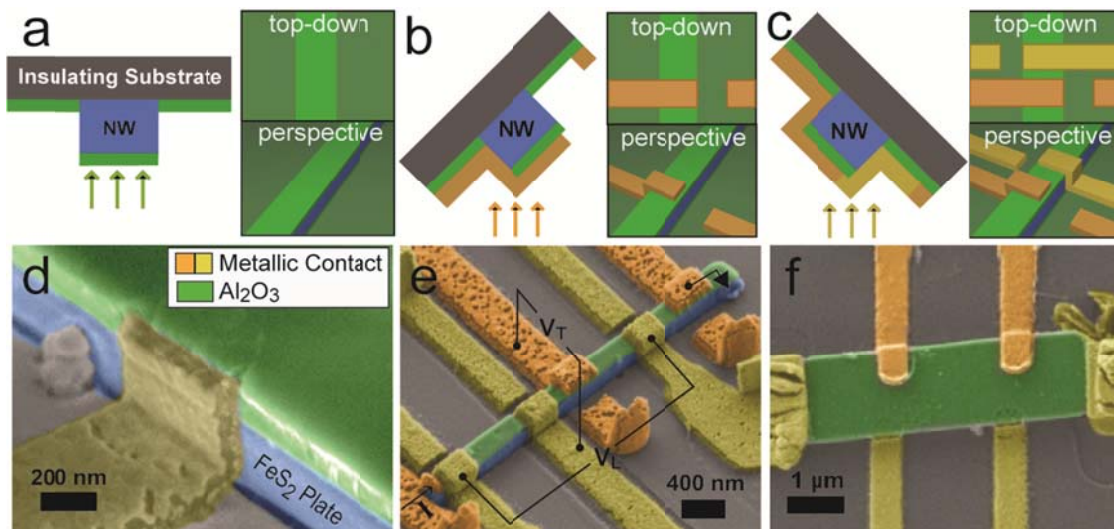


Figure 4.1. Fabrication of Hall effect devices using NWs. a-c) Schematic cross-sectional, top-down, and perspective views of the Hall device fabrication process. Arrows indicate the incidence of evaporated material (alumina in green and metal in orange or yellow). a) The first step of device fabrication is to evaporate an alumina layer with the incident angle of deposition perpendicular to the device substrate plane to insulate the top of the NW and prevent shorting of the Hall voltage by metal electrodes. b) The substrate plane is angled at 45 degrees allowing the NW to act as a shadow mask during contact deposition (orange electrodes). c) Completed device after flipping the substrate the opposite direction for final contact deposition (yellow electrodes). d-f) False color scanning electron micrographs (SEMs) of: d) a Hall electrode in contact with a FeS_2 nanoplate demonstrating intimate side wall contact, e) a completed six-probe FeS_2 NW Hall device, and f) a conventional Hall device based on a FeS_2 plate.

After completing the insulating Al_2O_3 layer, metal electrodes are deposited in two separate e-beam lithography and electrode deposition steps. We angle the plane of the device substrate ($\Theta = 45^\circ$) with respect to the emission source (Figure 4.1b) providing access to one of the exposed NW sidewalls while simultaneously using the NW structure itself as a shadow mask to prevent exposure of the opposite sidewall. The plane of the device substrate is flipped 180° for the second electrode deposition step (Figure 4.1c) providing access to the opposite sidewall. Since the device substrate is angled during deposition, we are careful to design the electrodes in such a way that the first electrode layer (orange in Figure 4.1) does not shadow the second electrode layer (yellow). This can only be accomplished by providing a longitudinal offset for the opposing Hall electrode which introduces an undesired longitudinal component to the transverse Hall voltage detection that reduces the sensitivity of the measurement. More sensitive Hall voltage measurements are obtained by minimizing the longitudinal separation between transverse electrodes. For well faceted nanostructures such as the FeS_2 NWs and nanoplates with rectangular cross-section we often observe that the electrode will lift off from the top of the device leaving only the sidewall contact (Figure 4.1d). Furthermore, we create intimate sidewall contact with much less deposited metal compared to a non-angled evaporation. A false color scanning electron micrograph (SEM) of a final Hall device fabricated using this scheme is shown in Figure 4.1e. (Note that even though the outmost current-source electrode for this particular NW device appears to be barely in contact, this contact was active during measurement). This fabrication method can be used equally well for thicker and thinner objects, with the smallest object successfully measured so far having a cross sectional dimension of 150 nm thick by 235 nm wide. The rectangular cross-section of the FeS_2 NWs makes the shadow evaporation easier and the fabrication process intuitive to illustrate, but Hall devices can also be fabricated using

NWs with other cross-section geometries albeit with some additional complications in the fabrication and data analysis procedures. An example NW Hall device fabricated from a cylindrical NW is shown in Figure A2.2 in Appendix 2.

We adopt a six-contact electrode geometry, schematically shown in Figure 4.2a inset and also superimposed on the SEM in Figure 4.1e, to enable the simultaneous monitoring of the pure longitudinal voltage signal (V_L) and the transverse voltage signal (V_T). Note that V_T is a convolution of the antisymmetric Hall voltage (V_H) and symmetric voltage (V_{xx}) which consists of the longitudinal and transverse magnetoresistance due to the small offset of opposing transverse contact electrodes mentioned above. The current is sourced through the outermost set of electrodes. Using this six-contact device scheme (Figure 4.2a inset), the longitudinal offset for the transverse contact electrode set creates a background contribution that reduces the sensitivity of the measurement, but the Hall voltage is by definition antisymmetric in magnetic field and can therefore be extracted by taking only the antisymmetric component of V_T . Therefore the Hall voltage (V_H) is calculated by

$$V_H = \frac{V_T(+B) - V_T(-B)}{2} \quad (4.1)$$

The Hall coefficient (R_H) and Hall mobility (μ_H) can then be calculated straightforwardly

$$R_H = \frac{V_H}{B} \frac{t}{I} \quad (4.2)$$

$$\mu_H = \frac{R_H}{\rho_{xx}} \quad (4.3)$$

where t is the thickness of the device, I is the applied current, and ρ_{xx} is the resistivity of the device at zero-field. The longitudinal voltage (V_L) enables the determination of ρ_{xx} and thus the

Hall mobility (μ_H), but if one is only interested in the Hall resistivity (ρ_{xy}) then the longitudinal contact set is not required in the device design, and a 4-probe measurement with only the transverse contact set can be used instead.

Measurements were performed inside a Quantum Design PPMS-9T where the orientation of the applied magnetic field is perpendicular to the NW axis. A Keithley 6221 is the DC current source and Keithley 2182A Nanovoltmeter was used to simultaneously monitor the longitudinal and transverse voltage signals. Data were collected by continuous sampling of the two voltage channels and were averaged over five voltage readings prior to post collection analysis. Figure 4.2a shows the relative voltage change as a function of magnetic field calculated as $[V(B)-V(0)]/V(B)$ measured for the transverse contacts (red dots) and the pure longitudinal component (blue dots) for a representative FeS₂ NW device at 300 K. For the longitudinal contacts this relative voltage change is essentially the longitudinal magnetoresistance. The Hall voltage (V_H) calculated using eq 4.1 versus the applied magnetic field is shown in Figure 4.2b.

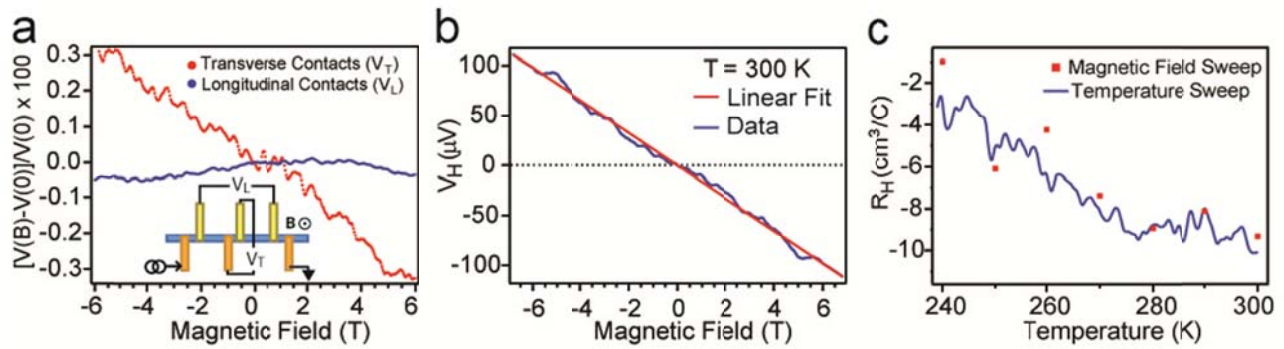


Figure 4.2. Measurement and extraction of the Hall voltage for a representative FeS₂ NW device. a) Inset shows the six-contact electrode geometry used to measure both longitudinal and transverse voltage signal. The outermost electrodes act as current source and drain. The relative voltage change from the transverse contacts (V_T) and longitudinal contacts (V_L) versus the magnetic field is plotted for 300 K. b) The Hall voltage (V_H) versus magnetic field calculated using eq 4.1 at 300 K. c) Comparison of Hall coefficients obtained for magnetic field sweeps at fixed temperature (red squares) and a temperature sweep scan with a fixed applied magnetic field (blue line). Good agreement is obtained between the two different scan methods for Hall data collection.

We can use two different types of data scans to extract the Hall coefficient at different temperatures. In the first type of scan, the temperature of the device is fixed and the magnetic field (B) is scanned from negative to positive values (Figure 4.2b). The best linear fit to the resulting data is used to extract the Hall coefficient using eq 4.2 (displayed as red squares for several temperatures in Figure 4.2c) and the Hall mobility using eq 4.3 at each temperature point. This is the more conventional method of determining the Hall coefficient and can be used to confirm the Hall effect results from the less conventional temperature sweep scans (solid line in Figure 4.2c). In the case of a temperature sweep, a Hall device is cooled to some initial starting temperature and held there for 20 min to reach thermal equilibrium, a positive magnetic field (typically 5.0 T) is applied and the temperature is scanned at a rate no faster than 5 K/min with continuous voltage data collection to the final temperature. Slower temperature scan rates minimize thermal equilibration artifacts in the measurement. Similar temperature scans are then performed under zero applied magnetic field and a negative magnetic field (typically -5.0 T). The zero applied field scan allows monitoring of the longitudinal resistivity. The Hall voltage (V_H) can then be calculated from eq 4.1 at each temperature. Comparing the calculated Hall coefficients derived from the two scan methods shown in Figure 4.2c clearly demonstrates that the faster temperature sweep (blue line) yields the same result as the magnetic field sweeps (red squares).

We have validated the Hall measurement method on NW devices by comparing FeS₂ NW Hall devices with the more conventional Hall plate devices (Figure 4.1f) because the as-synthesized FeS₂ nanostructures also include nanoplates of several micrometers wide and long and a few hundred nanometers thick in the same synthesis. This allows us to fabricate NW Hall devices and conventional Hall plate devices together. Table 1 summarizes the morphological

designation, the measured thickness and width, as well as the calculated Hall coefficient (R_H), resistivity (ρ_{xx}) and Hall mobility (μ_H) for 11 FeS₂ Hall devices that yielded the highest quality data with low noise. Nanostructures from bottom-up synthesis are expected to have variations in properties, and therefore, it is not surprising that the observed Hall coefficient among different devices ranges from -3.08 to -21.5 cm³/C. The calculated Hall coefficient was not found to correlate with device dimensions or any other measurement parameters (e.g. current density), as clearly shown in Figure A2.3 of Appendix 2. A scattered plot of R_H -values versus μ_H -values at $T = 295$ K (Figure 4.3) clearly shows the correlation of Hall coefficient with Hall mobility *independent of device morphology*. Therefore, we believe the variations in the observed Hall coefficients are caused by the variations in the semiconducting properties of various FeS₂ nanostructures as reflected in the mobility. This further confirms two key aspects of the experimental design: the measured Hall signal is not affected by the presence of a “residual” metal contact over the top of the NW (i.e., the Al₂O₃ layer is effective at preventing the shorting of Hall field), and the antisymmetrization analysis of the NW Hall device with offset transverse electrodes produces the same result as the more conventional plate geometry. From the comparison of different devices we can confidently conclude that the fabrication method, measurement setup, and data analysis produce the expected Hall signal for semiconducting NW Hall devices.

Table 1. Morphology and measured dimensions, calculated Hall coefficient (R_H), resistivity (ρ_{xx}) and Hall mobility (μ_H) at 295 K for 11 FeS₂ Hall devices.

morphology	width × thickness (nm)	R_H (cm ³ /C)	ρ_{xx} ($\Omega \cdot \text{cm}$)	μ_H (cm ² /V·s)
NW	234 × 150	-15.6	2.16	-7.23
NW	300 × 235	-21.5	1.73	-12.4
NW	353 × 220	-19.3	1.30	-14.8
NW	500 × 220	-3.08	1.42	-2.17
Rod	580 × 258	-21.1	3.14	-6.73
Rod	800 × 405	-8.39	2.69	-3.12
Rod	853 × 335	-7.76	2.30	-3.38
Plate	1450 × 550	-6.43	1.77	-3.64
Plate	1500 × 400	-12.5	3.42	-3.64
Plate	1800 × 330	-12.1	0.94	-12.9
Plate	2150 × 455	-3.72	1.19	-3.12

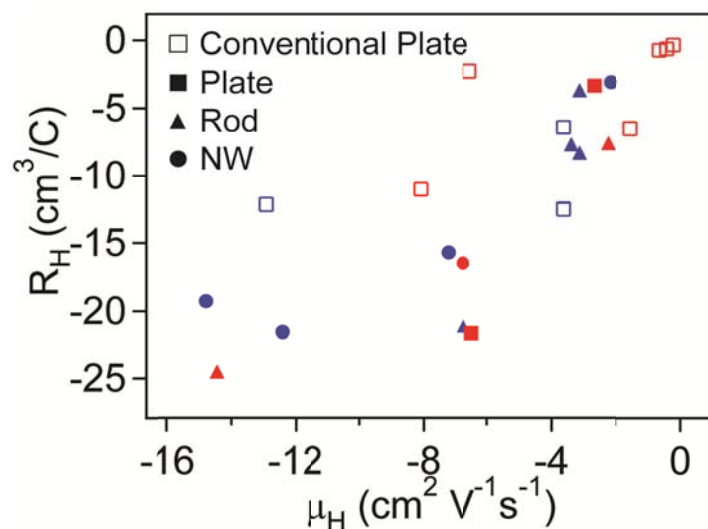


Figure 4.3. A scattered plot showing the calculated Hall coefficient (R_H) versus Hall mobility (μ_H) at 295 K for 21 Hall devices of FeS₂ NWs, nanorods, and nanoplates. Blue symbols represent the highest quality device data sets with low noise that have been presented in Table 4.1. Red symbols are extracted from 10 additional device sets not shown in Table 4.1. The extracted Hall coefficient agrees well for the NW (\bullet), rod (\blacktriangle), and plate (\square, \blacksquare) morphologies and no correlation was found for R_H and any specific device parameters. A *conventional plate* device (\square) does not have metallic electrodes that cross the top of the device, while a *plate* device (\blacksquare) has metallic electrodes that do cross the top of the device similar to the NW and rod devices.

Furthermore, we have extended the Hall measurement methodology to faceted MnSi NWs with widths between 100 and 500 nm that were synthesized according to our previous report.³⁶ MnSi is an itinerant-electron helical magnet that orders into a magnetic spin helix with a pitch of 19 nm below the magnetic transition temperature $T_c \approx 30$ K, due to the competition between ferromagnetic exchange interaction and the chiral Dzyaloshinsky-Moriya interaction.⁴³⁻⁴⁵ For small applied magnetic fields just below T_c , spins in MnSi form a Skyrmion lattice which can result in an additional small contribution to the measured Hall resistivity.⁷ Anomalous Hall effect measurements on bulk MnSi crystals have previously demonstrated that below the magnetic ordering temperature (about 30 K) a prominent “knee” feature appears in the low-field region of the Hall resistivity followed by positive curvature in the high-field region (these data are reproduced as Figure A2.5 in Appendix 2).^{7, 46} The Hall resistivity for the MnSi NW Hall device can be calculated as

$$\rho_{xy} = \left(\frac{V_H}{I} \right) \frac{A}{l} \quad (4.4)$$

where V_H is the Hall voltage calculated using eq 4.1, I is the source-drain current, A is the average of the Hall sidewall-contact areas, and l is width of the NW. Figures 4.4a,b show the symmetric (blue line) and antisymmetric (red line) components of the raw voltage measured by the transverse contact set (green line). The Hall resistivity data from a MnSi NW Hall device collected at 27 K (blue trace in Figure 4.4c) clearly shows a “knee” at roughly 0.6 T and then increases monotonically in the high-field region (also seen clearly in the 23 K and 28.5 K traces). This MnSi NW Hall device clearly displays similar qualitative behavior to the anomalous Hall effect observed in bulk MnSi, and the quantitative agreement is off by an order of magnitude compared to the reported bulk MnSi Hall resistivity.^{7, 46} To demonstrate generality, the data for

an additional MnSi NW device is shown as Figure A2.4 in Appendix 2 where similar knee features are also observed, and the magnitude of the Hall resistivity is off by a factor of about two. We do not expect perfect agreement since the magnetic phase diagram in NWs of MnSi is likely to deviate from that of bulk samples due to the nanoscale dimensions.^{5, 33-36} This second example of a successfully measured NW Hall device demonstrates the validity of our Hall effect measurement method for NW morphology and also shows the promise of using Hall measurements to probe the physics of the strongly correlated material MnSi. The development of a Hall measurement method is the first step towards electrically identifying the skyrmion phase in nanowire materials such as MnSi and $\text{Fe}_{1-x}\text{Co}_x\text{Si}$.^{47, 48}

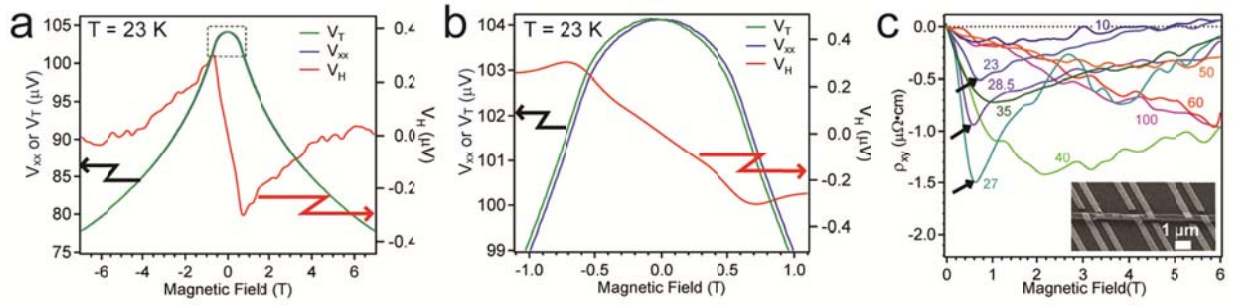


Figure 4.4. Measurement of a MnSi NW Hall device with a rhombohedra cross-section measuring $260 \text{ nm} \times 360 \text{ nm}$. a) For $T = 23 \text{ K}$, raw voltage measured by the transverse contacts (green line, V_T) along with separate symmetric (blue line, V_{xx}) and antisymmetric (red line, V_H) components. b) Zoom-in view of the highlighted rectangle in panel (a). c) Hall resistivity (ρ_{xy}) versus applied magnetic field at several temperatures for a MnSi NW (SEM image of the finished device shown as inset). Arrows indicate the “knee” feature of the anomalous Hall effect signal.

4.4 Conclusion

In summary, we have developed a general and facile method for making Hall measurements on NWs and have successfully demonstrated this method on well-faceted NW systems of FeS₂ and MnSi. We show that the offset of the transverse contacts does not impact the extraction of the Hall voltage when an antisymmetrization procedure is applied, and moreover, the insulating layer preventing the shorting of the Hall voltage and the intimate side-wall contact created by the angled evaporation technique are the keys to making successful Hall measurements. The addition of a longitudinal contact set can then be used to obtain the Hall mobility. The Hall coefficient has been successfully calculated for FeS₂ NWs, nanorods, and nanoplates using both temperature and magnetic field sweeps. The calculated Hall coefficient of FeS₂ NWs is consistent with the results from measurements on the conventional FeS₂ Hall plate devices, thus validating the Hall measurement on NWs. Furthermore, we measure the Hall resistivity of a MnSi NW device and show qualitative agreement with the anomalous Hall effect observed in bulk MnSi. We expect that this methodology will be widely applicable for measuring the Hall effect in 1D nanowire systems where such information can reveal basic semiconducting properties such as carrier type, concentration, mobility. Furthermore, new fundamental physical phenomena such as the integer quantum Hall effects in topological insulator materials, elucidation of chiral magnetic phases through topological Hall effects and anomalous Hall effects in other nanostructures of strongly correlated materials could be enabled by this measurement methodology.

Appendix 2 contains experimental details of nanowire Hall device fabrication, a schematic fabrication of nanowire Hall device with cylindrical geometry and an example device, two example Hall devices without the insulating alumina layer, additional comparisons of Hall

measurement results for 21 FeS₂ Hall devices, an additional MnSi NW Hall device, and reproduced bulk Hall resistivity data for MnSi from the literature.

4.5 Acknowledgement.

This work is supported by a NSF grant (ECCS-1231916). D. L. synthesized the pyrite nanostructures and contributed to device measurements of pyrite nanostructures and is supported by the U.S. Department of Energy, SunShot NextGen PV II program under Award DE-EE0005330. S.J. also thanks the UW-Madison Vilas Associate Award for support.

4.6 References

1. Popovic, R. S., *Hall Effect Devices*. 2nd ed.; Institute of Physics Publishing: Bristol, 2004.
2. Von, K. K.; Dorda, G.; Pepper, M. *Phys. Rev. Lett.* **1980**, *45*, 494-497.
3. Tsui, D. C.; Stormer, H. L.; Gossard, A. C. *Phys. Rev. Lett.* **1982**, *48*, 1559-1562.
4. Nagaosa, N.; Sinova, J.; Onoda, S.; MacDonald, A. H.; Ong, N. P. *Rev. Mod. Phys.* **2010**, *82*, 1539-1592.
5. Huang, S. X.; Chien, C. L. *Phys. Rev. Lett.* **2012**, *108*, 267201/1-267201/5.
6. Kanazawa, N.; Onose, Y.; Arima, T.; Okuyama, D.; Ohoyama, K.; Wakimoto, S.; Kakurai, K.; Ishiwata, S.; Tokura, Y. *Phys. Rev. Lett.* **2011**, *106*, 156603-1/156603-4.
7. Neubauer, A.; Pfeleiderer, C.; Binz, B.; Rosch, A.; Ritz, R.; Niklowitz, P. G.; Boni, P. *Phys. Rev. Lett.* **2009**, *102*, 186602-1/186602-4.
8. Schulz, T.; Ritz, R.; Bauer, A.; Halder, M.; Wagner, M.; Franz, C.; Pfeleiderer, C.; Everschor, K.; Garst, M.; Rosch, A. *Nat Phys* **2012**, *8*, 301-304.

9. Zang, J.; Mostovoy, M.; Han, J. H.; Nagaosa, N. *Phys. Rev. Lett.* **2011**, *107*, 136804/1-136804/5.
10. Benoît, D. *C. R. Phys.* **2011**, *12*, 323-331.
11. Hasan, M. Z.; Kane, C. L. *Rev. Mod. Phys.* **2010**, *82*, 3045-3067.
12. Law, M.; Goldberger, J.; Yang, P. *Annu. Rev. Mater. Res.* **2004**, *34*, 83-122.
13. Law, M.; Greene, L. E.; Johnson, J. C.; Saykally, R.; Yang, P. *Nat. Mater.* **2005**, *4*, 455-459.
14. Wallentin, J.; Anttu, N.; Asoli, D.; Huffman, M.; Aaberg, I.; Magnusson, M. H.; Siefer, G.; Fuss-Kailuweit, P.; Dimroth, F.; Witzigmann, B.; Xu, H. Q.; Samuelson, L.; Deppert, K.; Borgstroem, M. T. *Science* **2013**, *339*, 1057-1060.
15. Kempa, T. J.; Day, R. W.; Kim, S.-K.; Park, H.-G.; Lieber, C. M. *Energy Environ. Sci.* **2013**, *6*, 719-733.
16. Bierman, M. J.; Jin, S. *Energy Environ. Sci.* **2009**, *2*, 1050-1059.
17. Lu, W.; Lieber, C. M. *Nat. Mater.* **2007**, *6*, 841-850.
18. Liao, L.; Lin, Y.-C.; Bao, M.; Cheng, R.; Bai, J.; Liu, Y.; Qu, Y.; Wang, K. L.; Huang, Y.; Duan, X. *Nature* **2010**, *467*, 305-308.
19. Yan, R.; Gargas, D.; Yang, P. *Nat. Photonics* **2009**, *3*, 569-576.
20. Won, R. *Nat. Photonics* **2012**, *6*, 216.
21. Chen, R.; Ye, Q.-L.; He, T.; Ta, V. D.; Ying, Y.; Tay, Y. Y.; Wu, T.; Sun, H. *Nano Lett.* **2013**, *13*, 734-739.
22. Lin, Y.-C.; Chen, Y.; Shailos, A.; Huang, Y. *Nano Lett.* **2010**, *10*, 2281-2287.
23. Bierman, M. J.; Van Heuvelen, K. M.; Schmeisser, D.; Brunold, T. C.; Jin, S. *Adv. Mater.* **2007**, *19*, 2677-2681.

24. DeGrave, J. P.; Schmitt, A. L.; Selinsky, R. S.; Higgins, J. M.; Keavney, D. J.; Jin, S. *Nano Lett.* **2011**, *11*, 4431-4437.
25. Tian, Y.; Bakaul, S. R.; Wu, T. *Nanoscale* **2012**, *4*, 1529-1540.
26. Tang, J.; Wang, C.-Y.; Hung, M.-H.; Jiang, X.; Chang, L.-T.; He, L.; Liu, P.-H.; Yang, H.-J.; Tuan, H.-Y.; Chen, L.-J.; Wang, K. L. *ACS Nano* **2012**, *6*, 5710-5717.
27. Kim, P.; Shi, L.; Majumdar, A.; McEuen, P. L. *Phys. Rev. Lett.* **2001**, *87*, 215502-1/215502-4.
28. Zhou, F.; Szczech, J.; Pettes, M. T.; Moore, A. L.; Jin, S.; Shi, L. *Nano Lett.* **2007**, *7*, 1649-1654.
29. Szczech, J. R.; Higgins, J. M.; Jin, S. *J. Mater. Chem.* **2011**, *21*, 4037-4055.
30. Kong, D.-S.; Randel, J. C.; Peng, H.-L.; Cha, J. J.; Meister, S.; Lai, K.; Chen, Y.-L.; Shen, Z.-X.; Manoharan, H. C.; Cui, Y. *Nano Lett.* **2010**, *10*, 329-333.
31. Peng, H.; Lai, K.; Kong, D.; Meister, S.; Chen, Y.; Qi, X.-L.; Zhang, S.-C.; Shen, Z.-X.; Cui, Y. *Nat. Mater.* **2010**, *9*, 225-229.
32. Tang, H.; Liang, D.; Qiu, R. L. J.; Gao, X. P. A. *ACS Nano* **2011**, *5*, 7510-7516.
33. Wilson, M. N.; Karhu, E. A.; Quigley, A. S.; Rossler, U. K.; Butenko, A. B.; Bogdanov, A. N.; Robertson, M. D.; Monchesky, T. L. *Phys. Rev. B* **2012**, *86*, 144420/1-144420/6.
34. Tonomura, A.; Yu, X.; Yanagisawa, K.; Matsuda, T.; Onose, Y.; Kanazawa, N.; Park, H. S.; Tokura, Y. *Nano Lett.* **2012**, 1673-1677.
35. Karhu, E. A.; Rossler, U. K.; Bogdanov, A. N.; Kahwaji, S.; Kirby, B. J.; Fritzsche, H.; Robertson, M. D.; Majkrzak, C. F.; Monchesky, T. L. *Phys. Rev. B* **2012**, *85*, 094429/1-094429/12.
36. Higgins, J. M.; Ding, R.; DeGrave, J. P.; Jin, S. *Nano Lett.* **2010**, *10*, 1605-1610.

37. Cui, Y.; Zhong, Z.; Wang, D.; Wang, W. U.; Lieber, C. M. *Nano Lett.* **2003**, *3*, 149-152.
38. Garnett, E. C.; Tseng, Y.-C.; Khanal, D. R.; Wu, J.; Bokor, J.; Yang, P. *Nat. Nanotechnol.* **2009**, *4*, 311-314.
39. Storm, K.; Halvardsson, F.; Heurlin, M.; Lindgren, D.; Gustafsson, A.; Wu, P. M.; Monemar, B.; Samuelson, L. *Nat. Nanotechnol.* **2012**, *7*, 718-722.
40. Bloemers, C.; Grap, T.; Lepsa, M. I.; Moers, J.; Trellenkamp, S.; Gruetzmacher, D.; Lueth, H.; Schaepers, T. *Appl. Phys. Lett.* **2012**, *101*, 152106/1-152106/4.
41. Caban-Acevedo, M.; Faber, M. S.; Tan, Y.; Hamers, R. J.; Jin, S. *Nano Lett.* **2012**, *12*, 1977-1982.
42. Caban-Acevedo, M.; Liang, D.; Chew, K. S.; DeGrave, J. P.; Kaiser, N. S.; Jin, S. *ACS Nano* **2013**, *7*, 1731-1739.
43. Kadowaki, K.; Okuda, K.; Date, M. *J. Phys. Soc. Jpn.* **1982**, *51*, 2433-2438.
44. Adams, T.; Muhlbauer, S.; Pfeleiderer, C.; Jonietz, F.; Bauer, A.; Neubauer, A.; Georgii, R.; Boni, P.; Keiderling, U.; Everschor, K.; Garst, M.; Rosch, A. *Phys. Rev. Lett.* **2011**, *107*, 217206/1-217206/5.
45. Petrova, A. E.; Stishov, S. M. *Phys. Rev. B* **2012**, *86*, 174407-1/174407-5.
46. Lee, M.; Onose, Y.; Tokura, Y.; Ong, N. P. *Phys. Rev. B* **2007**, *75*, 172403-1/172403-4.
47. Higgins, J. M.; Carmichael, P.; Schmitt, A. L.; Lee, S.; Degrave, J. P.; Jin, S. *ACS Nano* **2011**, *5*, 3268-3277.
48. Porter, N. A.; Creeth, G. L.; Marrows, C. H. *Phys. Rev. B* **2012**, *86*, 064423-1/064423-6.

CHAPTER 5

Topological Hall Effect from Skyrmion Domains

in MnSi Nanowires at Large Current Densities

5.1 Abstract

Skyrmion magnetic domains have been revealed as general phenomenon in the B20 systems, characterized by a cubic lattice lacking a center of inversion symmetry. Here we use the topological Hall effect which is the definitive electrical signature of the skyrmion magnetic domain to map the phase stability of the skyrmion lattice in bottom-up synthesized MnSi nanowires. We show that the skyrmion phase is stabilized over an extended magnetic field—temperature window (15 to 35 K) compared to bulk MnSi crystals (27 to 29.5 K), and therefore, the nanowire morphology is an attractive system for implementing magnetic storage memory concepts such as racetrack memory. Lastly, we observe two additional critical fields in the magnetoresistance measurements of MnSi nanowires that can be attributed to the skyrmion magnetic phase when the applied magnetic field is preferentially applied along the long axis of the nanowire.

5.2 Introduction

Skyrmion magnetic domains can be manipulated using remarkably low current densities compared to ferromagnetic domain walls, and have become the focus of intense interest for

future low-power consumption nanoscale spintronics devices.¹⁻⁴ The relative stability and ease of manipulating magnetic skyrmions with electrical current results from their non-trivial topology, smoothly varying spin configuration, and unique ability to deform and avoid lattice defects.^{5,6} A magnetic skyrmion is a vortex-like spin texture in which the outer spins are aligned with the externally applied magnetic field and the central spin is anti-aligned. Their formation results from the competition of strong ferromagnetic exchange and the weaker spin-orbit Dzyaloshinskii-Moriya interaction that appears in crystal systems lacking a center of inversion symmetry. The cubic, non-centrosymmetric B20 crystal system is ideally suited for the observation and fundamental study of skyrmions and their current-driven dynamics, and several materials have so far been the focus of theoretical and experimental investigations including MnSi,^{3, 7-11} Fe_{1-x}Co_xSi,^{12, 13} FeGe,^{14, 15} MnGe,^{16, 17} and the multiferroic insulator Cu₂OSeO₃, that shares the P2₁3 space group.¹⁸⁻²⁰

To explore skyrmions for potential magnetic storage technology, we must further study the dynamics of skyrmions in nano-sized systems having already demonstrated significant advantages over bulk materials such as the stabilization of the skyrmion lattice.^{9, 21, 22} For example, as the dimension of the system approaches the size of the helical pitch (characterizing the ground magnetic state), the 1D conical magnetic configuration will be destabilized energetically compared to the 2D skyrmion state.^{8, 12, 15} The energetic stabilization of the skyrmion lattice can also be achieved in nanoscale systems by the introduction of large anisotropy energy that might result from surface induced effects or some strain in the system, such as an intrinsic strain associated with the growth of NWs.^{23, 24} Furthermore, the emergent electrostatics associated with current-driven skyrmions have not been explored extensively, and nanowire (NW) systems, having a smaller physical cross-section, are an essential platform

for exploring the dynamics of the skyrmion lattice at much larger current densities than can ever be achieved in bulk, and therefore, NWs can be utilized to manipulate skyrmions on faster timescales and understand fundamental dynamics of the skyrmion lattice.

The magnetic structure of the skyrmion domain can be described by the winding number defined as

$$\phi = \frac{1}{4\pi} \bar{n} \cdot \frac{\partial \bar{n}}{\partial x} \times \frac{\partial \bar{n}}{\partial y} \quad (5.1)$$

where $\bar{n} = \frac{\vec{M}_s}{|\vec{M}_s|}$ is the local magnetization direction, and x and y are the coordinates perpendicular to the applied magnetic field. When a conduction electron passes through such a topologically non-trivial spin texture, the conduction electron spin adiabatically couples to the local spin and acquires a quantum-mechanical Berry phase and can be re-formulated in terms of an effective magnetic field.^{3, 25} This effective magnetic field acts on the conduction electron such that the electron is deflected perpendicular to the current direction. Therefore, the presence of a skyrmion lattice will cause an additional contribution to the observed transverse electric field which has been termed the “topological” Hall contribution to the total Hall field.

Furthermore, the conduction electrons impart a force on the underlying magnetic spin structure through the spin-transfer-torque mechanism, a phenomenon that has been explored extensively in ferromagnetic systems.^{5, 26-29} At sufficiently high current densities this force is large enough to overcome the pinning forces of the skyrmion lattice, and the skyrmion domains begin to translate. In analogy with Faraday’s law, the motion of the effective magnetic field is expected to cause an “emergent” electric field perpendicular to the motion of the skyrmion lattice

$\vec{E}^e = -q_\sigma^e \vec{v}_d \times \vec{B}^e$ where \vec{B}^e is the effective field associated with a skyrmion, \vec{v}_d is the velocity of

the domains, and q_{σ}^e is the emergent charge associated with the conduction electron ($q_{\uparrow}^e = +1/2$ and $q_{\downarrow}^e = -1/2$). This emergent electric field opposes the topological Hall field from the Berry phase coupling in the case of the stationary skyrmion lattice and has been termed the skyrmion Hall effect.²⁹

Experimental observations of current driven motion of skyrmion domains have been carried out in bulk crystals of MnSi via small-angle neutron scattering¹ and Hall effect transport measurements,³ as well as observations of a FeGe thin film sample in real-space via Lorentz transmission electron microscopy (LTEM),² and these observations have revealed that the skyrmion magnetic domains translate primarily along the current direction and at a current density on the order of 10^5 - 10^6 A/m² which is up to 4-5 orders of magnitude smaller than the current densities required for the translation of ferromagnetic and helimagnetic domain walls.^{5, 30} This ultra-low current density may enable low-power consumption applications, and help to avoid common failure modes associated with very large current densities encountered in ferromagnetic systems being explored for racetrack memory concepts.³¹ If the skyrmion magnetic domain is to be exploited for such memory concepts, current-driven studies of skyrmion motion need to be extended to nanoscale morphologies which allow much higher current densities to be studied and higher velocities of the skyrmion lattice which are more technologically relevant.⁵ Therefore, there exists a strong motivation to extend topological Hall studies of skyrmion motion to the MnSi NW system in which skyrmion magnetic domains have already been observed using the LTEM technique.⁹

Here we report the observation of the topological Hall effect due to the skyrmion lattice phase measured using Hall effect measurements of MnSi NWs at large current densities (10^8 –

10^9 A/m²). We clearly demonstrate the extraction of the topological portion of the signal using a phenomenological fitting to account for the normal and anomalous Hall effect components of the total Hall signal. The analysis of the skyrmion lattice phase was also aided by the inferred phase diagram of magnetic ordering for a thinned slab of MnSi NW from previous Lorentz TEM observations. Additionally, the topological Hall effect was observed in both field-perpendicular and field-“parallel” (slight misorientation) to the long axis of the MnSi NW. In this magnetic field “parallel” to the NW axis orientation we identify two additional critical transitions in the symmetric magnetoresistance that have not previously been identified in MnSi NW measurements, and we attribute these additional transitions to the skyrmion lattice phase.

5.3 Results and Discussion

Electrical measurements were implemented on MnSi NWs obtained via a chemical vapor deposition synthesis²² using the Hall effect measurement methodology developed for faceted NW samples.²¹ Prior to depositing Ti/Au for Ohmic electrical contacts, a 20 nm insulating Al₂O₃ layer is deposited on top of the MnSi NW which prevents the shorting of the Hall field across the top of the NW, while also leaving the sidewall facets of the MnSi NW exposed for electrical contacts that are deposited with the device substrate tilted at a 45° angle.²¹ A four-terminal measurement was used in which the outermost electrical contacts act as current-source and drain, and the inner two contacts patterned via e-beam lithography are contacting opposite sides of the faceted MnSi NW to allow detection of the transverse Hall voltage (see Figure 5.1b inset for SEM of typical MnSi NW Hall effect device). The DC current was supplied by a Keithley 6221 current source, and a Keithley 2182A nanovoltmeter was used to monitor the voltage across the transverse contacts. The temperature and magnetic field control was provided

by a Quantum Design PPMS-9T. A common problem in some NW measurements made on devices fabricated using e-beam lithography is the observation of sporadic “2-level” jumping in which the resistance of the NW transitions between two different resistance levels, but exists for the majority of measurement in the lower of the two resistance states (see Appendix 3, Figure A3.1). This 2-level jumping adds additional noise to the measurements when continuously sweeping the magnetic field, and obtaining highly accurate signal becomes difficult. In order to achieve the high fidelity signal levels required to extract the small topological Hall contribution to the total Hall voltage we hold the externally applied magnetic field constant and acquire 50 voltage readings at each applied magnetic field (red dots in Figure 5.1a). Such a data collection method allows us to reject data points in the higher resistance state and allows further signal averaging over the lower resistance data points to obtain the most statistically accurate signal at each value of the magnetic field, represented by the blue squares in Figure 5.1a. This method of data collection is significantly more time consuming than previously collected data on MnSi NWs in which the field is continuously swept across a pre-defined field range. For this reason we only collected data in the field range from -0.9 T to $+0.9$ T which was determined to be the region of greatest interest through preliminary scans for identifying the topological Hall effect attributed to the skyrmion lattice phase in MnSi NWs, and was additionally confirmed by previous Lorentz-TEM observations of a MnSi NW from the same synthesis.⁹ Furthermore, at all temperatures studied, no magnetic transitions were observed to occur above 0.72 T which allows us to set this value as the maximum value for the upper-critical field transition to the field-polarized paramagnetic state (H_c), and the field value of this transition was found to decrease with increasing temperature. The MnSi NWs were tested at room temperature for Ohmic contact and were cooled from 300 K down to 10 K at a rate of 10 K/min under zero-

applied magnetic field. Once base temperature was reached, the device was allowed to equilibrate at 10.0 K for 80 min, and the field was set to -0.9 T. After collecting data across the field range from -0.9 T to $+0.9$ T the data collection was repeated in the reverse direction (from $+0.9$ T to -0.9 T) allowing us to check the reproducibility of the observed signals as well as to detect any magnetic hysteresis. After completion of the data collection to the final field of the second scan, the field was held fixed at the final value of -0.9 T and temperature was set to the next value at a rate of 0.2 K/min, and the device was allowed to equilibrate at the new set temperature for 60 min prior to beginning data collection. The 60 min equilibration time was found to be more than sufficient to reduce any artifacts caused by thermal equilibration to a negligible level.

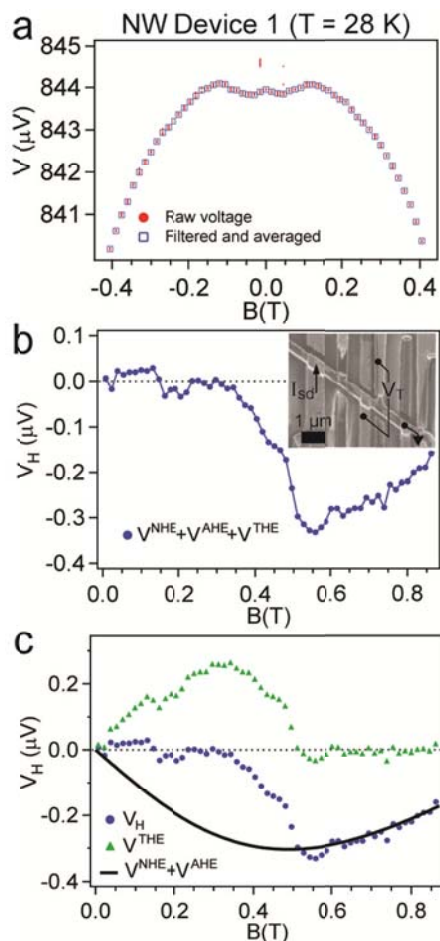


Figure 5.1. Extraction of the topological Hall effect voltage (V_{THE}) with external magnetic field perpendicular to the electrical current for NW Device 1 at $T = 28$ K. a) The raw voltage measured by the transverse Hall electrodes shown as red dots, and the blue squares represent the averaged data used for Hall analysis after removing the “2-level” jumping. b) The antisymmetric voltage (V_H) extracted from the raw voltage measurement in (a). c) The black line shows the fitting of the anomalous Hall effect and normal Hall effect contributions to the total Hall voltage. The fitting function is a combination of a linear term representing the NHE, and the Langevin function to represent the anomalous term that scales with the magnetization, saturating above H_c . The remaining signal (green triangles) is termed the topological Hall voltage (V_{THE}).

The Hall voltage (V_H) data is obtained by antisymmetrizing the raw voltage measured by the transverse contacts²¹ and is shown for a representative magnetic field sweep taken at $T = 28.0$ K in Figure 5.1b. The total Hall voltage (V_H) measured in MnSi NWs in the region of the skyrmion lattice phase consists of three components,

$$V_H = V_{NHE} + V_{AHE} + V_{THE} \quad (5.2)$$

these are the normal Hall effect (NHE) attributed to Lorentz forces on the conduction electrons due to the externally applied magnetic field, the anomalous Hall effect (AHE) which is known to scale with the magnetization of the sample, and the topological Hall effect (THE) which is attributed to the emergent magnetic and electric fields associated with the skyrmion magnetic texture in MnSi. Above the critical field for the transition between the conical and field-induced ferromagnetic state (H_c), the magnetization of the NW is saturated and the dominant contribution to the measured Hall voltage is the normal Hall effect, $V_{NHE} = R_0 BI/t$, where R_0 is the normal Hall coefficient, I is the source-drain current, and t is the thickness of the device. The AHE contribution (V_{AHE}) which when expressed in terms of resistivity is $\rho_{xy}^A = \alpha M \rho_{xx0} + \beta M \rho_{xx0}^2 + b M \rho_{xx}^2$ where α , β , and b correspond to the skew scattering, side jump, and intrinsic contributions to the anomalous Hall resistivity, ρ_{xx0} is the residual resistivity, and M is the magnetization.^{10, 32} To date, no technique has been developed for measuring the magnetization (M) of a single NW specimen while also allowing for the magnetotransport characterization of the same NW. For this reason, we importantly note that our results for the THE cannot be taken to represent an accurate quantitative picture of the magnitude of the THE in MnSi NWs since the AHE cannot be quantitatively subtracted from the data, and instead we must rely on a phenomenological assumption inferred from previous works on bulk MnSi, thin

films of MnSi,¹⁰ and MnSi NWs.^{21, 22} Namely, we assume that the magnetization is smoothly varying in the region of skyrmion lattice and the AHE and NHE can be subtracted by fitting the total Hall effect signal above the transition into the field-polarized ferromagnetic state (H_c), as shown in Figure 5.1c. We accomplish this by using a function that consists of a term linear in field to represent the NHE and a second term that is an approximation to the Langevin function (modeling the saturating magnetization of the MnSi NW) to represent the AHE contribution. We perform this subtraction confidently in the suspected region of the skyrmion lattice formation based both upon previous transport studies of MnSi NWs as well as recent Lorentz-TEM results of a thinned MnSi NW specimen.^{9, 21, 22} In principle, a similar phenomenological data extraction was applied to recent experiments of the topological Hall effect anomaly in bulk MnSi under pressure in which the non-topological Hall signal was fit using the assumption of a linear background.³³

We obtain the topological Hall voltage (V_{THE}) after this subtraction mentioned above, and then calculate the topological Hall resistivity

$$\rho_{xy}^T = \frac{V_{THE}}{I} \frac{\bar{a}}{w} \quad (5.3)$$

where I is the source-drain current, \bar{a} is the average area of the contacts used to collect the Hall voltage, and w is the width of the NW. The calculated ρ_{xy}^T values are shown for several temperatures from 10 to 40 K for a representative MnSi NW device (NW Device 1) in Figure 5.2a, and we use this set of data to construct the interpolated phase diagram shown in Figure 5.2c. The black dots in Figure 5.2c indicate the actual values of temperature and magnetic field where the voltage was collected to construct the THE phase diagram. To show the generality of the topological Hall signal, we have performed the same analysis on a second MnSi NW device

(NW Device 2) and construct the phase diagram for the topological Hall resistivity shown in Figure 5b. The magnitude of the topological Hall voltage that we extract can vary by up to 30% in magnitude depending on the precise cutoff field we chose for the fitting procedure, and a more detailed discussion follows below, however, the qualitative features remain unchanged by the exact details of the fitting procedure. The topological Hall voltage extracted using the above procedure was reproducible sweeping the field both from negative to positive and in the reverse direction, with the exception of a small hysteresis associated with the transitions into and out of the expected skyrmion lattice region, as shown in Figure 5.2a.

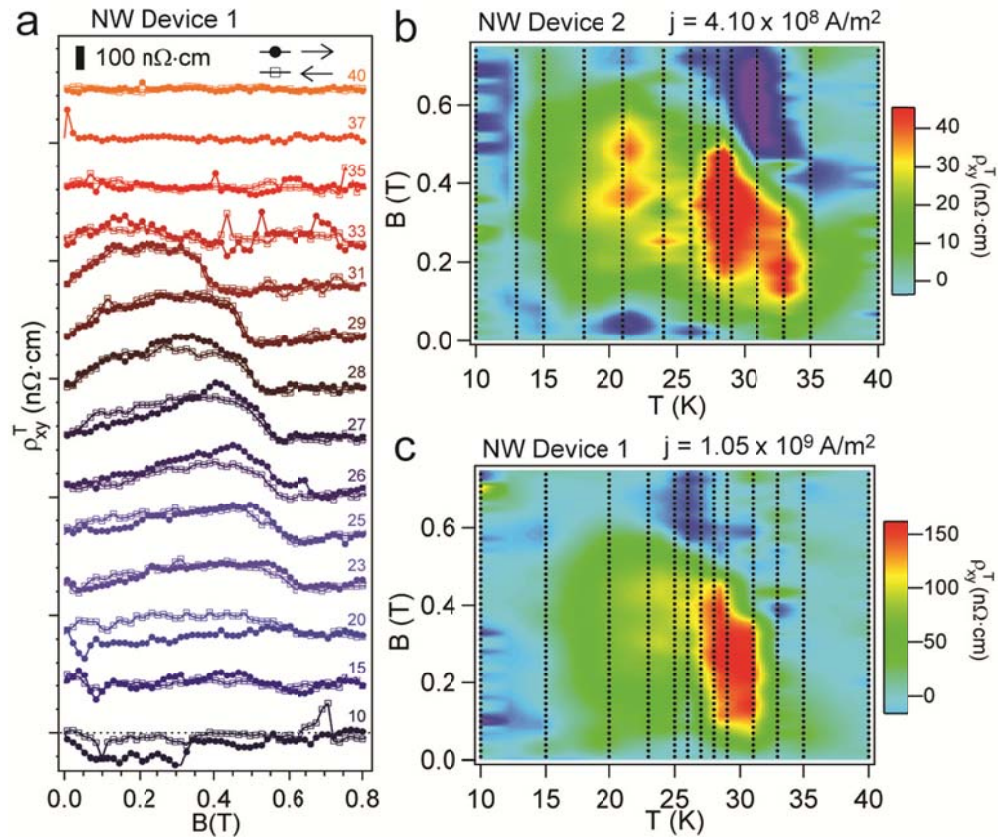


Figure 5.2. Topological Hall resistivity of two MnSi NW devices. a) Topological Hall resistivity for NW Device 1 at several temperatures extracted using the fitting procedure detailed in the text. Closed symbols represent data obtained by sweeping the magnetic field from negative to positive values, and open symbols were obtained in the reverse direction. b,c) Extracted topological Hall resistivity (ρ_{xy}^T) external magnetic field (B) versus temperature (T) phase diagrams constructed by interpolating ρ_{xy}^T between temperatures for NW Device 1 (232 nm wide by 164 nm thick) and NW Device 2 (305 nm wide by 280 nm thick). The black dots on the phase diagrams mark the temperature and field values of actual data points used to produce the colored phase diagram.

Since we did not examine the NWs in an electron microscope prior to measurement, the current density applied to the device can only be calculated after the electrical measurements were complete. We typically used applied currents of between 30 and 50 μA , or roughly $10^8 - 10^9 \text{ A/m}^2$ depending on the NW cross section geometry, in an attempt to optimize the signal level while also avoiding excessive Joule heating of the NW device caused by any contact resistance. Current levels below 10 μA did not produce sufficient signal levels to extract V_{THE} reliably, while current levels above 100 μA caused excessive Joule heating which can raise the temperature of the device beyond T_c (e.g. Figure A3.1c). The recorded temperatures of the measurements correspond to the thermometer reading in the cryogenic system, and the true temperatures of the NW device measurements could be slightly higher due to the local Joule heating effect. Therefore, the temperatures reported in the phase diagrams (Figures 5.2b,c) can be underestimates of the true NW device temperature. Furthermore, this local heating of the NW devices has so far made it difficult to examine the current dependence of the topological Hall signal. The magnitude of the extracted topological Hall resistivity differs significantly between NW Devices 1 and 2, discussed in detail below. Given the observed ρ_{xy}^T for NW Devices 1 and 2, the skyrmion phase has been identified in the extended phase region from a minimum of 15 K up to T_c or roughly 35 K which is in agreement with previous measurements of T_c for helimagnetic MnSi NWs.^{22, 34}

MnSi has now been studied extensively in several morphologies, and with several different characterization techniques. High purity bulk crystals of MnSi show a T_c of $\sim 29.5 \text{ K}$, and the skyrmion lattice phase has been identified down to $\sim 27.0 \text{ K}$ using a combination of SANS and topological Hall effect studies.^{7, 8, 35-37} Unstrained thin films of MnSi (thinned from bulk MnSi

crystals) observed via LTEM have shown an extended skyrmion phase region, with skyrmions observed at a minimum temperature of roughly 6 K, but there was also an observed decrease in T_c to 22 K that could be accounted for by the limitation of the spin-spin correlation length imposed by the thin film.^{11, 38} On the other hand, strained thin films of MnSi (111) grown on Si(111) by molecular beam-epitaxy (MBE) examined by susceptibility,^{24, 39} topological Hall effect,¹⁰ and LTEM measurements¹⁰ have also shown a significantly extended skyrmion phase region with a lower bound for the skyrmion lattice at 2 K and an increase in T_c up to ~45 K. The increased T_c of these MnSi thin films has been attributed to the de-compressive strain (or negative pressure) associated with the mismatched MnSi(111) film and Si(111) substrate.¹⁰ While MnSi bulk crystals under the effects of significant external pressure have shown a decrease in T_c .^{33, 40} Taking all these various morphologies into consideration, it is likely that our NWs experience some intrinsic strain or other surface induced effects that tend to increase T_c . Moreover, the lowest temperature we observe the topological Hall effect signal in MnSi NWs is roughly 15 K which places these MnSi NW samples somewhere between observed bulk behavior with a narrow skyrmion phase region (27 – 29.5 K), and the observed behavior for 50 nm thin films of strained MBE grown MnSi with a wider skyrmion phase region extending from 2 – 45 K. Since the dimensions of our NW sample are on the order of 200 nm, our results agree well with those previously reported.

As mentioned above, the magnitude of the extracted topological Hall voltage may be associated with a systematic error of up to 30%, and in order to compare these two NW Devices we show in Figure 5.3a the extracted ρ_{xy}^T for each device taken at the peak value with the error bars calculated from multiple fittings of the Hall voltage (V_H) clearly demonstrating the

statistically different results for ρ_{xy}^T . The magnitude of ρ_{xy}^T is known to depend on several factors and can be written as $\rho_{xy}^T \approx n_{skx} P R_0 B^e$, with n_{skx} the skyrmion density ($n_{skx} = 1$ for compact arrays), P the spin polarization of conduction electrons, R_0 the normal Hall coefficient, and B^e is the emergent magnetic field associated with one unit cell of the skyrmion lattice, or roughly -13 T for the hexagonal lattice of skyrmions in MnSi.^{7, 14, 33, 41, 42} It has also been previously suggested for the case of the THE measured for epitaxial FeGe(111) thin films, that size confinement may cause an increase in the skyrmion density.¹⁴ This effect is consistent with the MnSi NW devices measured here, since the NW having smaller cross-section (NW Device 1) produced a larger ρ_{xy}^T . Specifically, the ratio of NW cross-sections between NW Device 1 and NW Device 2 ≈ 2.24 , which is nearly the ratio between the observed ρ_{xy}^T for these two MnSi NW devices. The spin polarization (P) in MnSi can also be drastically affected by surface induced effects or by the presence of strain which can change the band structure of conduction electrons in MnSi.^{10, 43-45} Moreover, the residual resistivity ratios (RRR), calculated as $R(300\text{ K})/R(10\text{ K})$, for NW Device 1 and 2 were 10.55 and 7.74, respectively, indicating that our NW samples contain a higher level of defects and impurities compared to the high purity bulk single crystals and epitaxial MnSi(111) thin films so far reported for THE measurements.^{3, 10} The phenomenological fitting procedure prevents us from quantitatively extracting R_0 , but the sign of our Hall effect measurements here is opposite to those so far reported but consistent with the previous report of the AHE in MnSi NWs.²¹ This is a clear indication that the higher level of extrinsic defects and impurities are significantly impacting the band structure. Taking all these differences into account, it is not unexpected that we measure a larger ρ_{xy}^T for our MnSi NW devices compared to previous bulk and thin film measurements of MnSi.

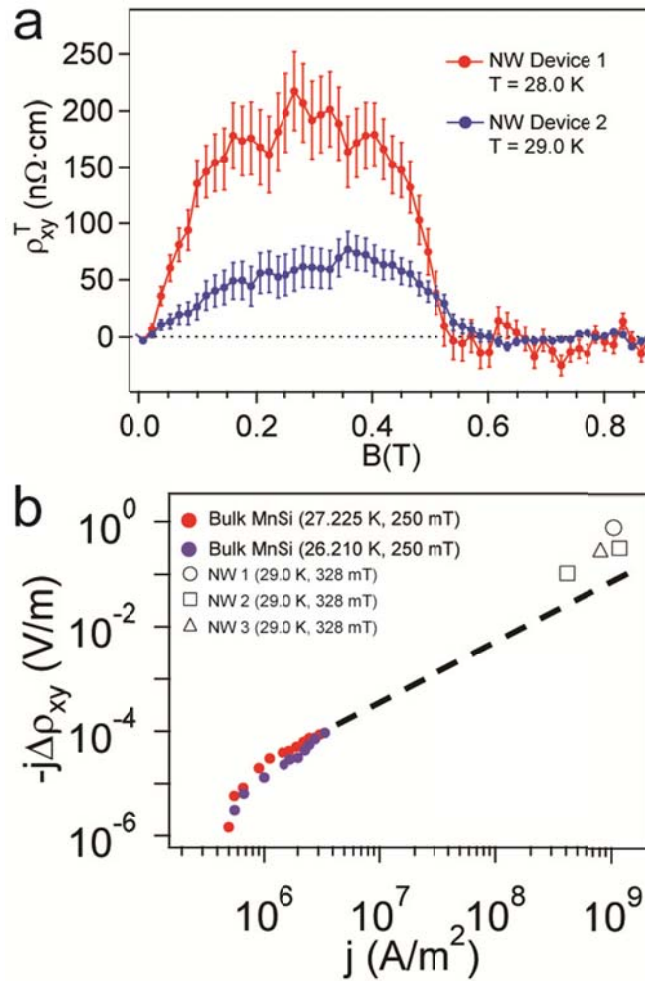


Figure 5.3. a) Comparisons of the topological Hall resistivity for MnSi NW Device 1 and 2. The temperatures of magnetic field sweeps selected for each NW device correspond to the maximum extracted value for ρ_{xy}^T . Error bars are calculated from multiple fittings of the Hall voltage (V_H), as described in the main text. b) Calculated perpendicular emergent electric field versus the current density. The two data sets plotted for bulk MnSi ($T = 26.210, 27.225$ K; $B = 250$ mT) were adopted from the un-scaled data in the supplement of Ref. 3. NW 1 and 2 correspond to NW Devices 1 and 2, previously discussed in this work, and NW 3 is taken from an additional data set for a MnSi NW with the dimension of 210 nm wide x 145 nm thick. The dashed line provides a guide to the eye.

As was demonstrated in the recent studies on bulk MnSi crystals³ and an FeGe thin film² the skyrmion lattice translates under sufficiently large applied current densities. The smaller sample dimensions of the NW morphology allow us to access much larger current densities compared to bulk systems. The translating skyrmion lattice causes a reduction in the measured ρ_{xy}^T that saturates for $j \gg j_c$ as the speed of the skyrmion domains becomes roughly equivalent to the speed of conduction electrons. Although the current-driven dynamics of the skyrmion lattice are relatively unexplored at large current densities, the speed of the skyrmion lattice translation (v_d) is expected to increase linearly with current density and thus the magnitude of the emergent electric field (E^e) also increases linearly.^{3, 5, 29} In our work, the current densities used to measure NW Device 1 and 2 were 1.05×10^9 A/m² and 4.10×10^8 A/m², respectively (as noted in Figures 5.2b,c) and is roughly three orders of magnitude larger than the critical current required for depinning the skyrmion lattice as observed for high purity bulk crystals of MnSi, yet the applied current density is still lower than a recent calculation suggesting the melting of the skyrmion lattice into a chiral liquid phase beyond an upper threshold current density (on the order of 10^{12} A/m²).⁴⁶ The magnitude of the extracted Hall voltage (V_{THE}) in these MnSi NW devices was used to provide a rough estimate of the emergent electric field (E^e) associated with the suspected motion of the skyrmion lattice at these large current densities using the simple assumption that $E^e \approx V_{THE}/w$, where w is the width of the MnSi NW device. We present a comparison to the experimental data observed for the translating skyrmion lattice in bulk MnSi in Figure 5.3b.³ The difference in sample quality, indicated by the small residual resistivity values for MnSi NW Device 1 and 2 is not expected to significantly impact E^e due to the weak pinning of the skyrmion lattice on impurities,⁵ therefore, a rough extrapolation can be used to

provide confidence in the extracted topological Hall voltage for these MnSi NW devices. We have adopted the un-scaled data for bulk MnSi³ at $T = 27.225$ and 26.210 K, and $B = 250$ mT shown as red and purple dots in Figure 5.3b, respectively, and compare this to data from three NW devices used in this work. The temperature and field values selected for comparison were chosen for the NW devices to be within the maximum extracted topological Hall voltage, and the dotted line provides a guide to the eye. The estimated electric field should be on the order of tens of nanovolts, and this result matches very well with the magnitude of our measurements of these MnSi NWs (given the error associated with the extraction of the topological Hall voltage).

We have additionally studied the THE with the external magnetic field preferentially parallel to the NW axis (with the angle between the long axis of the NW and the applied magnetic field at 26°). This “parallel” orientation was accomplished by warming the device back to room temperature so that the device carrier could be physically rotated by 90 degrees and the externally applied magnetic field lies in the plane of the device substrate. The e-beam lithography process we utilize creates an inherent uncertainty in the exact orientation of the NW, but the exact orientation of the NW axis in relation to the applied magnetic field was measured post-electrical measurement using a scanning electron microscope. This misalignment inevitably introduces a contribution to the measured Hall effect from the NHE attributed to Lorentz forces, but this is taken account for and subtracted in the same manner as presented for the magnetic field perpendicular to the NW axis which is the more typical geometry for Hall effect measurements. This magnetic field orientation allows us to observe the effects of the strong geometrical anisotropy from the NW morphology on the formation of the skyrmion phase while still being able to measure the THE due to the angle between the source-drain current and external magnetic field direction. First, the magnetoresistance, calculated from the symmetric

signal as $[\rho_{xx}(B) - \rho_{xx}(0)] / \rho_{xx}(0)$, measured by the transverse contacts is plotted in Figure 5.4a. At several temperatures in the suspected skyrmion phase region we observe the clear signature of two additional critical fields (highlighted with arrows in Figure 5.4a) that cannot be attributed to the spin-flop conical transition at low field or the transition from conical to field-polarized ferromagnetic state at high field (H_c). Decreasing the magnetic field from the field-polarized ferromagnetic state, the following critical fields are identified: (1) H_c (commonly referred to as B_{C2} in MnSi literature)³⁵ corresponding to the inflection point in the magnetoresistance and is identified up to $T = 35$ K, (2) B_{A2} which we define as a minimum in $d\rho_{xx}/dB$, (3) B_{A1} which is the next minimum in $d\rho_{xx}/dB$, and finally, (4) near $B = 0$ there appears a consistent local minimum in $d\rho_{xx}/dB$ that we identify as B_{C1} . B_{A1} and B_{A2} do not appear as strong features in $d\rho_{xx}/dB$ when the magnetic field is applied perpendicular to the current direction for our NW devices, and have not been previously identified in transport measurements. These additional critical fields have been identified in bulk MnSi susceptibility measurements, and have been attributed to the skyrmion lattice phase.³⁵ Furthermore, we have plotted B_{A1} and B_{A2} as open symbols on the phase diagram obtained for the topological Hall resistivity in Figure 5.4b. The critical fields, B_{A1} and B_{A2} , in the magnetoresistance fall in the same region as the observed topological Hall resistivity, providing further supporting evidence for our interpretation of the Hall effect anomaly as the THE.

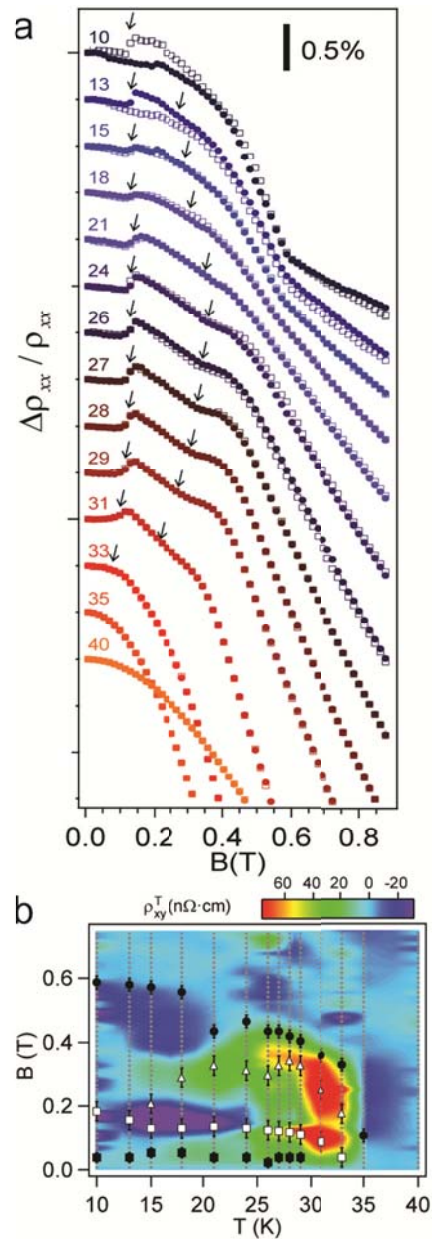


Figure 5.4. Symmetric magnetoresistance and topological Hall effect of NW Device 2 measured with the externally applied magnetic field preferentially applied parallel to the long axis of the NW (26° misalignment). a) Symmetric magnetoresistance signal plotted as a function of magnetic field of NW device 2, with arrows indicating the approximate position of critical fields leading to the open symbols in the temperature-magnetic field phase diagram in panel b. b)

Phase diagram obtained for the topological Hall resistivity of NW Device 2 by interpolating the signal between several fixed temperature magnetic field sweeps. Filled circles are the upper critical field transition to the field-polarized ferromagnetic state and the filled squares correspond to the first minimum in $d\rho_{xx}/dB$.

The following are the main differences between this “parallel” measurement orientation and the measurements presented in the first part of this work: (1) the critical temperature for the observed topological Hall signal remains unchanged between the two orientations, (2) the upper critical field for the observed topological Hall anomaly in the parallel orientation is roughly 0.45 T compared to 0.58 T in the perpendicular orientation, (3) the magnitude of the maximum topological Hall resistivity is unchanged in the center of the skyrmion phase region, (4) in the “parallel” orientation there appears to be two peaks in the skyrmion phase, and the peak at lower field (roughly 0.17 T across the whole temperature range) changes sign between 20 and 26 K. T_c would not be expected to change when the measurement orientation is changed, and therefore provides a self-consistent confirmation of the upper critical temperature for the skyrmion phase in MnSi NW Device 2 at roughly 35 K which agrees with all previous measurements on NW samples.^{9, 21, 22} The rest of the observed differences can be attributed to the demagnetizing field associated with strong geometrical anisotropy. When the device is measured in the parallel orientation, the demagnetizing factor is nearly zero so that the external magnetic field is nearly equal to the internal field, and we therefore are much more sensitive to the fine magnetic structure of the NW sample. When the device is measured in the perpendicular orientation, the demagnetizing factor cannot be calculated exactly, but should be greater than 0.5, and this large demagnetizing factor will broaden the observed critical features.

5.4 Conclusion

In summary, we have measured the topological Hall effect signal in MnSi NW devices using large current densities, and have used this signal to map the phase diagram of the skyrmion lattice. The topological Hall effect signal was extracted using a phenomenological assumption

which has prohibited some quantitative analyses that would be interesting for future work on MnSi NWs, but preliminary estimates show that the magnitude of emergent electric field roughly follows the expected linear increase with applied current density. In the measurement orientation with magnetic field “parallel” to the NW axis, we have identified additional critical fields in the magnetoresistance of MnSi NWs that can be attributed to the skyrmion magnetic phase. Finally, the skyrmion phase was shown to be stabilized over an extended magnetic field—temperature window (15 to 35 K) compared to bulk MnSi crystals (27 to 29.5 K). The extended skyrmion phase stability of a MnSi NW compared to bulk MnSi would be interesting to extend to other systems, especially FeGe in which both the enhanced stability of the skyrmion lattice and an increase in T_c resulting from NW morphology could help realize the use skyrmion domains in near room temperature applications.

5.5 References

1. Jonietz, F.; Muhlbauer, S.; Pfleiderer, C.; Neubauer, A.; Munzer, W.; Bauer, A.; Adams, T.; Georgii, R.; Boni, P.; Duine, R. A.; Everschor, K.; Garst, M.; Rosch, A. *Science* **2010**, *330*, 1648-1651.
2. Yu, X. Z.; Kanazawa, N.; Zhang, W. Z.; Nagai, T.; Hara, T.; Kimoto, K.; Matsui, Y.; Onose, Y.; Tokura, Y. *Nat. Commun.* **2012**, *3*, 988-1/988-6.
3. Schulz, T.; Ritz, R.; Bauer, A.; Halder, M.; Wagner, M.; Franz, C.; Pfleiderer, C.; Everschor, K.; Garst, M.; Rosch, A. *Nat. Phys.* **2012**, *8*, 301-304.
4. Fert, A.; Cros, V.; Sampaio, J. *Nat. Nanotechnol.* **2013**, *8*, 152-156.
5. Iwasaki, J.; Mochizuki, M.; Nagaosa, N. *Nat. Commun.* **2013**, *4*, 1463/1-1463/8.
6. Rosch, A. *Nat. Nanotechnol.* **2013**, *8*, 160-161.

7. Neubauer, A.; Pfeleiderer, C.; Binz, B.; Rosch, A.; Ritz, R.; Niklowitz, P. G.; Boni, P. *Phys. Rev. Lett.* **2009**, *102*, 186602-1/186602-4.
8. Mühlbauer, S.; Binz, B.; Jonietz, F.; Pfeleiderer, C.; Rosch, A.; Neubauer, A.; Georgii, R.; Boni, P. *Science* **2009**, *323*, 915-919.
9. Yu, X.; DeGrave, J. P.; Hara, Y.; Hara, T.; Jin, S.; Tokura, Y. *Nano Lett.* **2013**, 3755–3759.
10. Li, Y.; Kanazawa, N.; Yu, X. Z.; Tsukazaki, A.; Kawasaki, M.; Ichikawa, M.; Jin, X. F.; Kagawa, F.; Tokura, Y. *Phys. Rev. Lett.* **2013**, *110*, 117202/1-117202/5.
11. Tonomura, A.; Yu, X. Z.; Yanagisawa, K.; Matsuda, T.; Onose, Y.; Kanazawa, N.; Park, H. S.; Tokura, Y. *Nano Lett.* **2012**, 1673–1677.
12. Yu, X. Z.; Onose, Y.; Kanazawa, N.; Park, J. H.; Han, J. H.; Matsui, Y.; Nagaosa, N.; Tokura, Y. *Nature* **2010**, *465*, 901-904.
13. Milde, P.; Köhler, D.; Seidel, J.; Eng, L. M.; Bauer, A.; Chacon, A.; Kindervater, J.; Mühlbauer, S.; Pfeleiderer, C.; Buhrandt, S.; Schütte, C.; Rosch, A. *Science* **2013**, *340*, 1076-1080.
14. Huang, S. X.; Chien, C. L. *Phys. Rev. Lett.* **2012**, *108*, 267201/1-267201/5.
15. Yu, X. Z.; Kanazawa, N.; Onose, Y.; Kimoto, K.; Zhang, W. Z.; Ishiwata, S.; Matsui, Y.; Tokura, Y. *Nature Mater.* **2011**, *10*, 106-109.
16. Kanazawa, N.; Kim, J. H.; Inosov, D. S.; White, J. S.; Egetenmeyer, N.; Gavilano, J. L.; Ishiwata, S.; Onose, Y.; Arima, T.; Keimer, B.; Tokura, Y. *Phys. Rev. B* **2012**, *86*, 134425/1-134425/7.
17. Kanazawa, N.; Onose, Y.; Arima, T.; Okuyama, D.; Ohoyama, K.; Wakimoto, S.; Kakurai, K.; Ishiwata, S.; Tokura, Y. *Phys. Rev. Lett.* **2011**, *106*, 156603-1/156603-4.

18. White, J. S.; Levatic, I.; Omrani, A. A.; Egetenmeyer, N.; Prsa, K.; Zivkovic, I.; Gavilano, J. L.; Kholbrecher, J.; Bartkowiak, M.; Berger, H.; Ronnow, H. M. **2012**, arXiv:1208.1146v1.
19. Seki, S.; Yu, X. Z.; Ishiwata, S.; Tokura, Y. *Science* **2012**, *336*, 198-201.
20. Seki, S.; Kim, J. H.; Inosov, D. S.; Georgii, R.; Keimer, B.; Ishiwata, S.; Tokura, Y. *Phys. Rev. B* **2012**, *85*, 220406/1-220406/4.
21. DeGrave, J. P.; Liang, D.; Jin, S. *Nano Lett.* **2013**, *13*, 2704-2709.
22. Higgins, J. M.; Ding, R.; DeGrave, J. P.; Jin, S. *Nano Lett.* **2010**, *10*, 1605-1610.
23. Butenko, A. B.; Leonov, A. A.; Rossler, U. K.; Bogdanov, A. N. *Phys. Rev. B* **2010**, *82*, 052403-1/052403-4.
24. Wilson, M. N.; Karhu, E. A.; Quigley, A. S.; Rossler, U. K.; Butenko, A. B.; Bogdanov, A. N.; Robertson, M. D.; Monchesky, T. L. *Phys. Rev. B* **2012**, *86*, 144420/1-144420/6.
25. Nagaosa, N.; Tokura, Y. *Physica Scripta* **2012**, *2012*, 014020/1-014020/15.
26. Everschor, K.; Garst, M.; Duine, R. A.; Rosch, A. *Phys. Rev. B* **2011**, *84*, 064401/1-064401/10.
27. Brataas, A.; Bauer, G. E. W.; Kelly, P. J. *Phys. Rep.* **2006**, *427*, 157-255.
28. Zutic, I.; Fabian, J.; Das Sarma, S. *Rev. Mod. Phys.* **2004**, *76*, 323-410.
29. Zang, J. D.; Mostovoy, M.; Han, J. H.; Nagaosa, N. *Phys. Rev. Lett.* **2011**, *107*, 136804/1-136804/5.
30. Jiang, X.; Thomas, L.; Moriya, R.; Hayashi, M.; Bergman, B.; Rettner, C.; Parkin, S. S. P. *Nat. Commun.* **2010**, *1*, 1-5.
31. Parkin, S. S. P.; Hayashi, M.; Thomas, L. *Science* **2008**, *320*, 190-194.
32. Nagaosa, N.; Sinova, J.; Onoda, S.; MacDonald, A. H.; Ong, N. P. *Rev. Mod. Phys.* **2010**, *82*, 1539-1592.

33. Ritz, R.; Halder, M.; Franz, C.; Bauer, A.; Wagner, M.; Bamler, R.; Rosch, A.; Pfeleiderer, C. *Phys. Rev. B* **2013**, *87*, 134424/1-134424/17.
34. Seo, K.; Yoon, H.; Ryu, S.-W.; Lee, S.; Jo, Y.; Jung, M.-H.; Kim, J.; Choi, Y.-K.; Kim, B. *ACS Nano* **2010**, *4*, 2569-2576.
35. Bauer, A.; Pfeleiderer, C. *Phys. Rev. B* **2012**, *85*, 214418/1-214418/16.
36. Lebech, B.; Harris, P.; Skov Pedersen, J.; Mortensen, K.; Gregory, C. I.; Bernhoeft, N. R.; Jermy, M.; Brown, S. A. *J. Magn. Magn. Mater.* **1995**, *140*, 119-120.
37. Kadowaki, K.; Okuda, K.; Date, M. *J. Phys. Soc. Jpn.* **1982**, *51*, 2433-2438.
38. Fisher, M. E.; Barber, M. N. *Phys. Rev. Lett.* **1972**, *28*, 1516-1519.
39. Karhu, E. A.; Rossler, U. K.; Bogdanov, A. N.; Kahwaji, S.; Kirby, B. J.; Fritzsche, H.; Robertson, M. D.; Majkrzak, C. F.; Monchesky, T. L. *Phys. Rev. B* **2012**, *85*, 094429/1-094429/12.
40. Ritz, R.; Halder, M.; Wagner, M.; Franz, C.; Bauer, A.; Pfeleiderer, C. *Nature* **2013**, *497*, 231-234.
41. Bruno, P.; Dugaev, V. K.; Taillefumier, M. *Phys. Rev. Lett.* **2004**, *93*, 096806/1-096806/4.
42. Tatara, G.; Kohno, H.; Shibata, J.; Lemaho, Y.; Lee, K.-J. *J. Phys. Soc. Jpn.* **2007**, *76*, 054707/1-054707/13.
43. Jeong, T.; Pickett, W. E. *Phys. Rev. B* **2004**, *70*, 075114/1-075114/8.
44. Hortamani, M.; Sandratskii, L.; Kratzer, P.; Mertig, I.; Scheffler, M. *Phys. Rev. B* **2008**, *78*, 104402/1-104402/9.
45. DeGrave, J. P.; Schmitt, A. L.; Selinsky, R. S.; Higgins, J. M.; Keavney, D. J.; Jin, S. *Nano Lett.* **2011**, *11*, 4431-4437.

46. Lin, S.-Z.; Reichhardt, C.; Batista, C. D.; Saxena, A. *Phys. Rev. Lett.* **2013**, *110*, 207202-1/207202-5.

APPENDIX 1

Supporting information for CHAPTER 2

Spin Polarization Measurement of Homogeneously Doped

Fe_{1-x}Co_xSi Nanowires by Andreev Reflection Spectroscopy

A1.1 Synthesis of Fe_{1-x}Co_xSi nanowires

Nanowires were synthesized using two separate precursor routes in a home-built chemical vapor deposition setup with Ar gas flow and pressure control as previously described.^{1, 2} In both methods the furnace was used to maintain the Si substrate at 750° C, and the reaction was held at a constant pressure of 200 torr. For Sample1/Sample 2 a mixture of *Trans*-Fe(SiCl₃)₂(CO)₂ (Sample 1: 88 mg, 0.20 mmol, Sample 2: 78 mg, 0.18 mmol) and Co(SiCl₃)(CO)₄ (Sample 1: 100 mg, 0.33 mmol, Sample 2: 174 mg, 0.57 mmol) were reacted as described in Ref. 1. Sample 3 was synthesized using two precursor boats, one containing 100 mg *Trans*-Fe(SiCl₃)₂(CO)₂ and the other containing 50 mg CoCl₂ as described in Ref. 2.

A1.2 Elemental analysis

Elemental analysis was performed on single nanowires dispersed onto TEM grids via an ethanol solution. The spectra were recorded using an Energy Dispersive Spectroscopy (EDS) Analysis System on a Zeiss LEO 1530 SEM and analyzed for Fe : Co ratio using Noran Systems Software.

A1.3 Atom probe specimen mounting

Nanowire specimens were mounted onto microtips supplied by Imago Scientific Instruments. c nanowires were plucked from the Sample 2 ($\bar{x} = 0.18$) growth substrate using a micromanipulator tip and moved to contact the microtip pillars at 54° in a Zeiss Cross-beam scanning electron microscope (SEM). The wire was welded to the post using Pt deposition from a gas injection system housed within the SEM. Pt is deposited by focusing the electron beam on specific areas. Beam shift control is used to shape the specimen into a conical shape to maximize heat conduction away from the tip.

A1.4 Atom probe tomography

An Imago local electrode atom probe (LEAP) instrument with laser pulsing was used at the Northwestern University Center for Atom Probe Tomography (NUCAPT) to collect data from mounted $\text{Fe}_{1-x}\text{Co}_x\text{Si}$ alloy nanowires. A variety of conditions were tested to obtain mass spectra including temperature, voltages, pulse fraction, laser energy and frequency, and evaporation rate. Nanowire samples were initially cooled to 30 K and the temperature slowly rose to 56.5 K over the 2 h duration of the experiment. The laser frequency was 50 kHz, and the laser energy was stepped between 0.15 nJ and 0.21 nJ. The resulting spectrum is calibrated using the $^{12}\text{C}^{+1}$ and H^{+1} peaks. Peaks are calculated based on the elements present in the sample (Fe, Co, Si, and O) and in the LEAP environment (H and C). Mass spectra were corrected and reconstructed using Imago IVAS 3.0.5 software package. A typical nanowire tomographic reconstruction contains over 500,000 ions collected in the voltage range of 3000-3700 V.

A1.5 X-ray magnetic circular dichroism (XMCD)

XMCD was performed on $\text{Fe}_{1-x}\text{Co}_x\text{Si}$ nanowire Sample 1 ($\bar{x} = 0.27$) at the Argonne National Laboratory (ANL) Advance Photon Source (APS) on beamline 4ID-C. Nanowires were sonicated in ethanol and dispersed onto Ge substrates aggregating into a large cluster of wires about 1 mm wide. The substrates were electrically contacted to a Cu stage using both carbon tape and silver paint to ensure electrical conduction. Ensemble nanowire samples were then loaded into a vacuum chamber and aligned in the beam at 55° incident angle to maximize total electron yield (TEY) at the Si K edge prior to sample collection at a 2 Tesla field strength and temperature of 6 K. Because of the nanomorphology of the sample, TEY detection is preferred. Total fluorescence yield (TFY) is noisy due to scattering of phonons off the rough surface of the nanowire bunches, and a significant amount of the nanowires (with diameters 30-70 nm) are detected in TEY. For every energy point, both left and right circularly polarized x-ray data were collected.

A1.6 Andreev reflection measurements

Electrical measurements were made on devices fabricated using e-beam lithography. $\text{Fe}_{1-x}\text{Co}_x\text{Si}$ nanowires were drop-cast from an ethanol dispersion onto degenerately doped p-type silicon substrates coated with a 600 nm thermal oxide layer. The wires were located using optical microscopy on a pre-written grid. Electrodes were written using the Nanoscale Pattern Generation System (NPGS) in two lithographic steps to pattern contacts of both a normal metal and a superconductor. Prior to each deposition step the device is subjected to a buffered HF

solution for ~ 7 seconds to remove any silicon oxide layer on the nanowire. In the first lithographic step normal metal contacts consisting nominally of 40 nm Ti/ 60 nm Au/ 40 nm Al_2O_3 were deposited via e-beam evaporation. In the second step, Nb (~ 90 nm) was deposited with a DC magnetron CVC 601 Sputtering System (6" target, 500 V, 5 mtorr, 20 sccm Ar, 15 mins). The device substrate was mounted on a chip carrier, wire bonded with Al wire, and measured inside a Quantum Design Physical Property Measurement System (9T-PPMS) at liquid helium temperatures. Measurements presented in the main text were made using a Keithley 6221 Current Source and a Keithley 2182A Nanovoltmeter in differential conductance mode (probe setup described in the main text). Figure A1.1a shows the scheme for an alternate measurement setup employing a conventional AC Lock-in technique with an EG&G 7265 DSP Lock-in Amplifier and an EG&G Model 113 Pre-amplifier that was used in some early measurements.

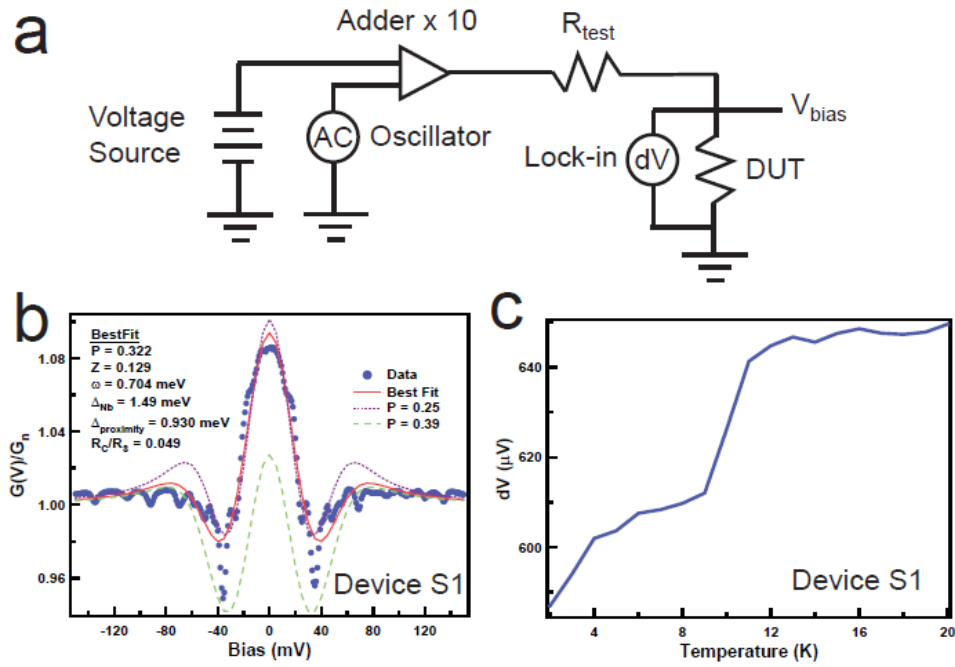


Figure A1.1. a) Schematic AC Lock-in measurement setup used to measure Device S1. b) Normalized differential conductance as a function of bias voltage for Device S1. c) Differential voltage as a function of temperature indicating the rise in device resistance as T_c of Nb is approached.

A1.7 Additional Andreev Reflection Data

We include here a total of five $\text{Fe}_{1-x}\text{Co}_x\text{Si}$ nanowire device Andreev reflection measurement data sets in addition to the ones shown in the main text. Figure A1.1b shows the only data set presented here that was measured with the AC Lock-in measurement setup, moreover Device S1 was taken from Sample 1 ($\bar{x} = 0.27$). All other data sets were collected with the DC technique described above and were fabricated with nanowires from Sample 3 ($\bar{x} = 0.23$). Both measurement techniques produce similar results, however, the DC technique is capable of acquiring data much more rapidly and requires fewer pieces of equipment and is the preferred method. Device S1 through S4 (Figure A1.2) were all successfully fit with the modified BTK model described in the main text. Each set of normalized conductance data is accompanied by additional temperature dependent behavior that indicates the respective zero-bias feature is dependent on the superconducting state of the Nb contact, allowing us to rule out other phenomena. The devices shown in Figure A1.2 are ordered from the largest spreading resistance to the lowest spreading resistance. The two probe resistances for Device S2, S3, S4 (measured with the DC technique) were 1.60 k Ω , 1.20 k Ω , and 47 Ω respectively. Each of the data sets also has two *P-trial* fits plotted atop the data. Some of these fits are nearly degenerate with the best fit, however, none of the data sets could be successfully fit using a *P-trial* set equal to zero spin-polarization. This is further evidence that the Andreev reflection data does not arise from a direct short between Ti/Au and Nb electrodes.

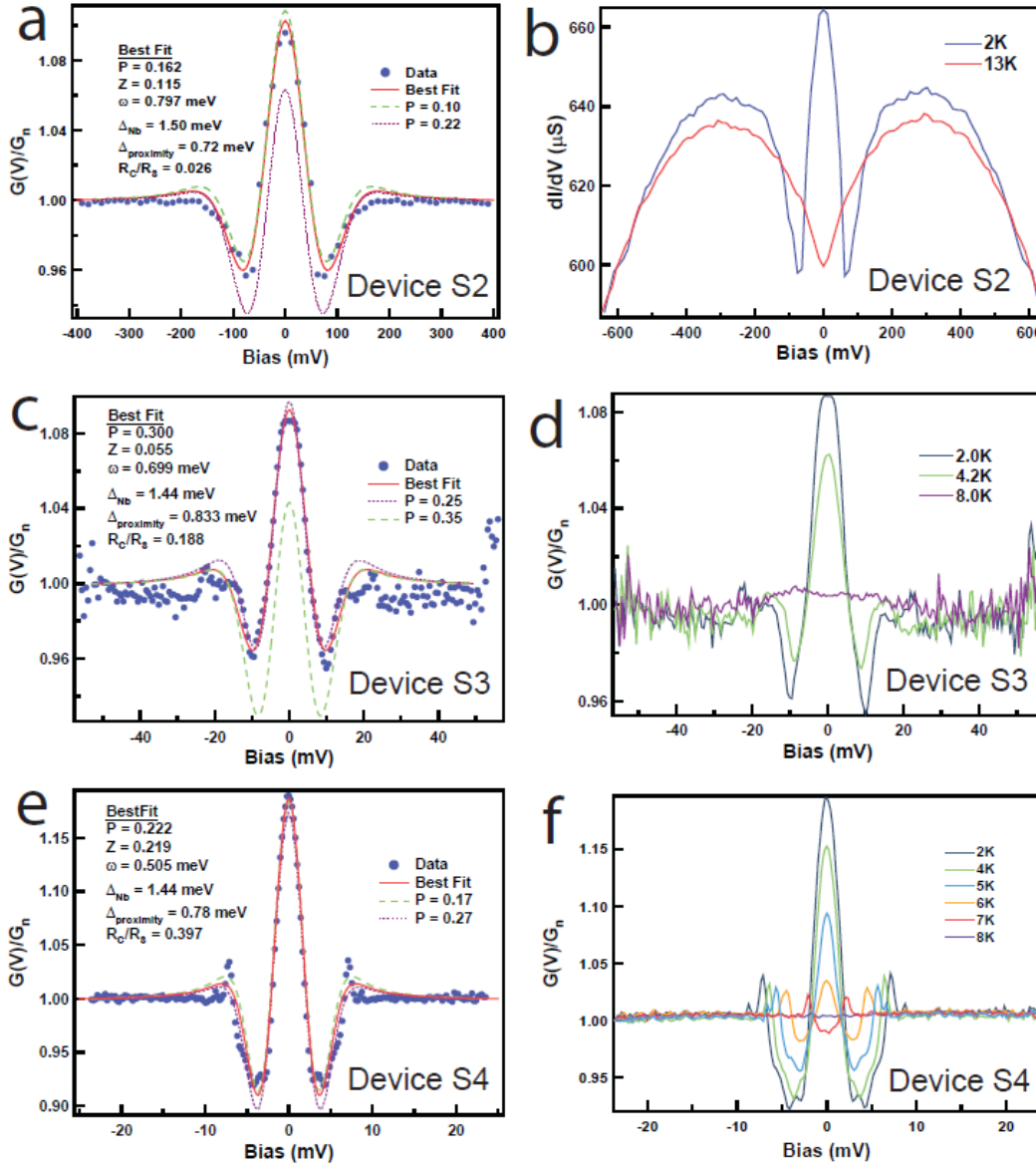


Figure A1.2. Additional Andreev Reflection measurement data sets for devices S2-S4 that can be fit with the modified BTK model. a, c, e) Normalized differential conductance data plotted with the best fit lines from the modified-BTK model. Each plot also includes two P-trial fits demonstrating the robustness of the fitting result. b, d, f) Additional differential conductance behavior at various temperatures demonstrating the reduction in Andreev reflection signal as T_c of Nb is approached.

Figure A1.3 shows an additional data set that appears to have Andreev reflection signal (Figure A1.3a) and the correct resistance versus temperature behavior (Figure A1.3b) for $\text{Fe}_{1-x}\text{Co}_x\text{Si}$ nanowires. However, a robust fit was not obtained due to the large amount of noise in the data. The SEM image of this device shows clearly that the normal metal and superconducting contacts are well separated by a nanowire channel of 420 nm (Figure A1.3b inset). The two-probe resistance obtained for this device was 2.29 k Ω and it was the highest resistance device that still produced an Andreev reflection signal. Devices that have channel lengths longer than this yielded no observable Andreev reflection signal.

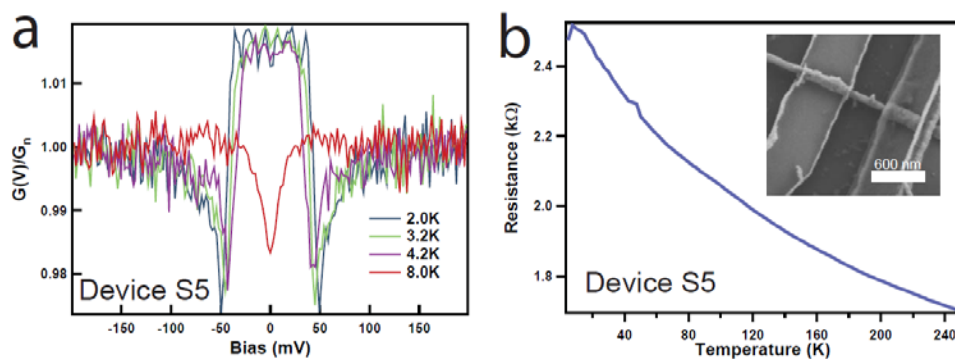


Figure A1.3. a) Andreev reflection signal at various temperatures for a $\text{Fe}_{1-x}\text{Co}_x\text{Si}$ nanowire device that cannot be successfully fit with the modified BTK model. b) Resistance versus temperature data that matches the established behavior of this material. Inset shows a SEM of the device measured.

A1.7 References

1. Higgins, J. M.; Carmichael, P.; Schmitt, A. L.; Lee, S.; Degrave, J. P.; Jin, S. *ACS Nano* **2011**, 5, (4), 3268-3277.
2. Schmitt, A. L.; Higgins, J. M.; Jin, S. *Nano Lett.* **2008**, 8, (3), 810-815.

APPENDIX 2

Supporting Information for CHAPTER 4

A General Method to Measure the Hall Effect in Nanowires:

Examples of FeS₂ and MnSi

A2.1 Experimental Details for Fabricating Nanowire Hall Effect Devices

Nanowires (NWs) are deposited onto a Si/SiO₂ (600 nm) substrate either by dry transfer or by drop casting from an ethanol dispersion created by sonicating the growth substrate in 3-4 drops of ethanol for about 10 s. In the case of drop casting, nitrogen gas is flown across the surface of the device substrate which tends to align the NWs with the stream of nitrogen. The substrate covered with aligned NWs is then loaded into a metal deposition system for deposition of insulating alumina (Al₂O₃) by e-beam evaporation without tilting the sample stage. The thickness of the alumina layer depends on the NW material as discussed in the main text, typically 40 nm for nanowires of FeS₂ and MnSi .

Next, a numeric grid with alignment marks and wire bonding pads is patterned on the device substrate in the first lithographic step using a Zeiss LEO Supra 55 VP (30 kV) scanning electron microscope (SEM) and Nanometer Pattern Generation System (NPGS) e-beam system. We implement a MMA/PMMA bilayer e-beam resist (MicroChem) for all e-beam lithography steps and develop the exposed patterns in 1:3 IPA:MIBK solution (MicroChem). For the numeric grid

and bonding pads, a metallic bi-layer of 40 nm Ti and 30 nm Au are deposited via e-beam evaporation.

After liftoff in acetone, the positions of the NWs on the numerical grid are located and recorded digitally using a dark-field optical microscope. The lithographic pattern was then designed using NPGS and DesignCAD LT2000 software. The first layer is written via e-beam lithography and the pattern developed, and then the device substrate is subjected to a 30 s, 100 W oxygen plasma etch and 3-5 s buffered HF (Buffered HF improved, Transene Company Inc.) etch prior to metal deposition. The device substrates are loaded onto a sample stage tilted 45° with respect to the incident angle of evaporated material. The first electrode contact layer is then deposited and the choice of contact metal depends upon the necessary conditions for ohmic contact. In the case of FeS₂ nanostructures either Au or Ti/Au is used, and in the case of MnSi NWs a Ti/Au bilayer is used. The total electrode thickness ranged between 60 and 110 nm with no observable difference in device performance. After another round of e-beam lithography to define the second set of opposing electrode pattern, the final contact electrode layer is then deposited with the device substrate flipped the opposite direction but still on the sample stage tilted 45° with respect to the incident angle of evaporated material to allow the contact to the opposite sidewall of the NW device (see schemes in Figure 4.1 a-c of the main text).

A2.2 Hall Devices without the Insulating Al₂O₃ Layer

To demonstrate the importance of the insulating alumina layer, we show in Figure A2.1 the device measurement results for two FeS₂ Hall devices that were fabricated without the alumina deposition step (but otherwise the same as shown in Figures 4.1a-c of the main text). The extracted Hall voltage is observed to oscillate about zero, thus the calculated Hall coefficient will

also oscillate about zero in stark contrast to devices that include the insulating alumina layer, as presented in the main text.

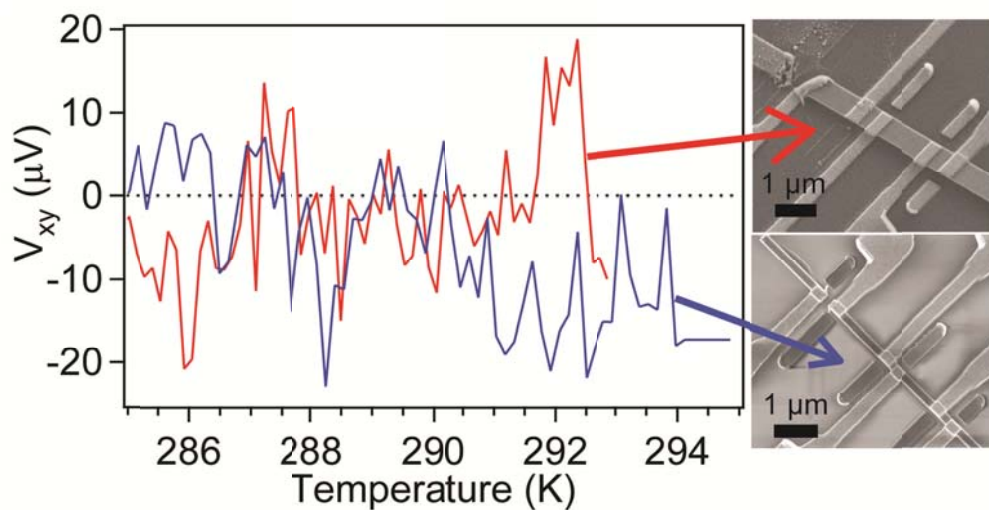


Figure A2.1. FeS₂ nanowire hall devices without the insulating Al₂O₃ layer. The Hall voltage oscillates about zero, clearly demonstrating the importance of including an insulating layer on the top of the nanowire to prevent the Hall voltage from shorting. The SEM images on the right were taken after the devices were measured and broke. The red line corresponds to a FeS₂ nanobelt device with 550 nm width and the blue line corresponds to a FeS₂ nanowire device with 220 nm width.

A2.3 Cylindrical Nanowire Hall Device

The Hall device fabrication and measurement methodology developed in this work is general to other materials and to samples with both circular and square cross-sections. We also used a Si NW with 100 nm diameter to demonstrate the generality of the Hall device fabrication process. Figure A2.3a and inset show the cross-section and perspective schematics for a finished cylindrical NW device fabricated using the same procedure described in Figure 4.1a-c in the main text. Figure A2.3b shows the SEM of a representative finished device using a silicon NW with circular cross-section and the desired device geometry.

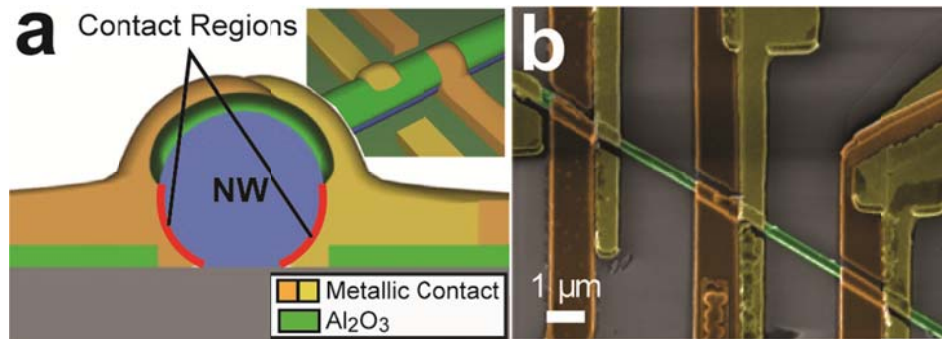


Figure A2.2. a) Schematic cross-section and perspective (inset) views of completed cylindrical Hall NW device. b) False color SEM of final cylindrical NW Hall effect device (fabricated from a 100 nm diameter Si NW for demonstration).

A2.4 Additional Hall Device Comparisons

The scattered plots of the Hall coefficient and Hall mobility determined from Hall measurements at 295 K in correlation with various parameters for 23 devices are collected in Figure A2.2. The Hall coefficient and Hall mobility determined from Hall measurements do not correlate with any geometrical or measurement parameters that might convolute the comparison of different device morphologies (i.e. FeS₂ nanowires versus nanorods and nanoplates).

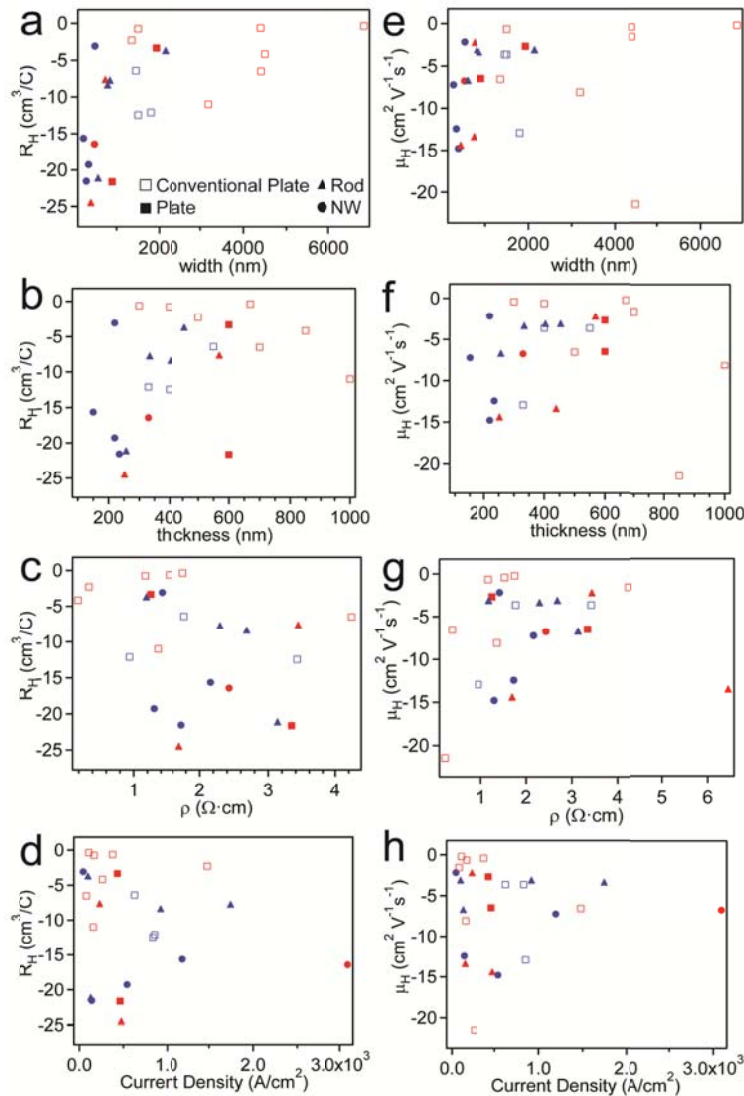


Figure A2.3. Additional data plots for 23 FeS₂ Hall devices showing the (lack of) correlation of Hall coefficient and Hall mobility determined from Hall measurements with various parameters. a-d) The calculated Hall coefficient is plotted versus device width, thickness, resistivity and current density to show the absence of correlation. e-h) The calculated Hall mobility is plotted versus device width, thickness, resistivity and current density to show the absence of correlation. Blue symbols correspond to 10 devices also presented in Table 4.1 (main text) and represent the highest quality (low noise) data sets. Red symbols are extracted from 13 additional device sets.

A2.5 Additional MnSi NW Hall Device

An additional MnSi NW device is included here to demonstrate the generality of the qualitative features observed for MnSi NWs. For this particular MnSi NW device, the Hall resistivity is only shown up to 2.0 T, but the “knee” features mentioned in the main text still are clearly seen in the 28 K (purple) and 20 K (red) traces at approximately the same field values.

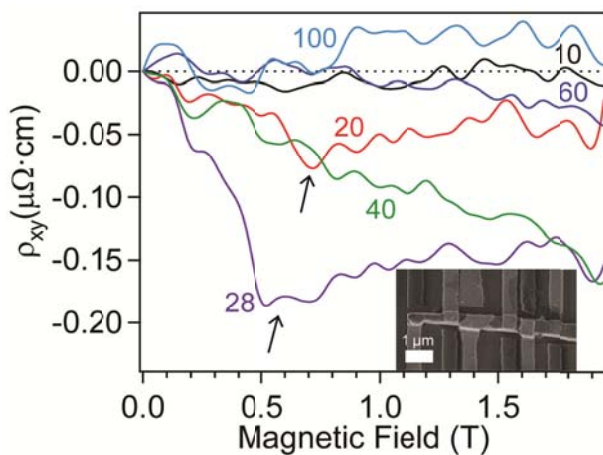


Figure A2.4. Hall resistivity (ρ_{xy}) versus applied magnetic field at several temperatures for a MnSi NW Hall device with a rhombohedra cross-section measuring $420 \text{ nm} \times 240 \text{ nm}$ (SEM image of the finished device shown as inset). Arrows indicate the “knee” feature of the anomalous Hall effect signal.

A2.6 Bulk MnSi Hall Resistivity Data

The bulk MnSi Hall resistivity data from Lee et al.¹ and Neubauer et al.² showing the anomalous Hall effect are reproduced below in Figure A2.5 for comparison to our result for a MnSi NW Hall device (shown in Figure 4.5 in the main text) to demonstrate qualitatively similar behavior.

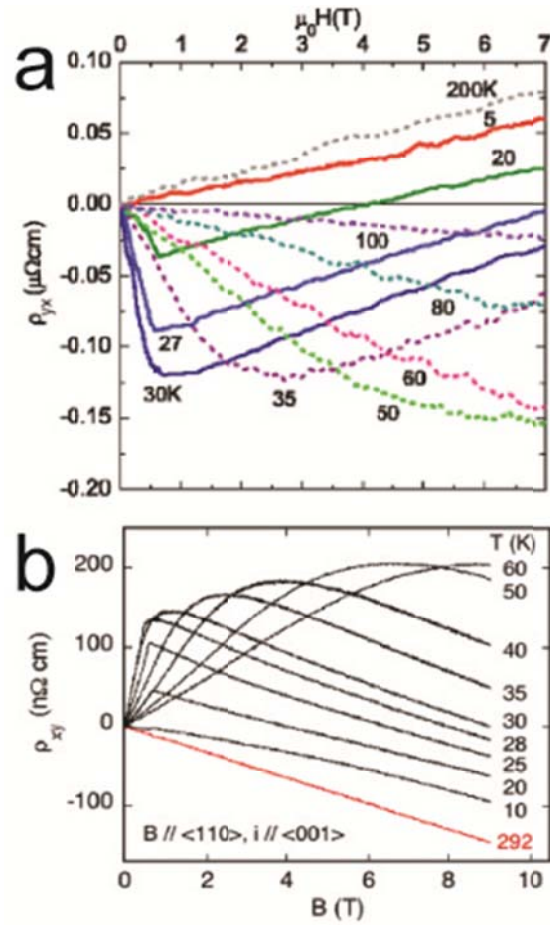


Figure A2.5. Previously reported Hall resistivity for bulk MnSi versus applied magnetic field from a) Lee et al.¹ and b) Neubauer et al.²

A2.7 References

1. Lee, M.; Onose, Y.; Tokura, Y.; Ong, N. P. *Phys. Rev. B* **2007**, *75*, 172403-1/172403-4.
2. Neubauer, A.; Pfleiderer, C.; Binz, B.; Rosch, A.; Ritz, R.; Niklowitz, P. G.; Boni, P. *Phys. Rev. Lett.* **2009**, *102*, 186602-1/186602-4.

APPENDIX 3

Supporting Information for CHAPTER 5

Topological Hall Effect from Skyrmion Domains

in MnSi Nanowires at Large Current Densities

A3.1 Joule Heating Effect and “2-level” Jumping in a MnSi Nanowire Devices

As was discussed in Chapter 5, the MnSi nanowire (NW) devices are subject to Joule heating caused by the DC current and contact resistance associated with the electron-beam lithography and metal deposition technique used to fabricate the NW device. In Figure A3.1a we have plot the symmetric magnetoresistance for a representative MnSi NW device at $T = 26.0$ K that shows the clear indication of this local Joule heating effect, namely, the magnetic field value of the transition from the conical state to the field-polarized ferromagnetic state (H_c) changes with applied current (this has been highlighted with colored arrows in Figure A3.1b). Additionally, Figures A3.1a,b show that if the applied current is too small, the measurement becomes noticeably less precise since we are approaching the noise floor of the experimental voltage detection setup. Figure A3.1c shows a more drastic example of the local Joule heating effect at $T = 20.0$ K where a DC current of $100 \mu\text{A}$ (green curve) has locally increased the temperature of the device above T_c and the kink associated with H_c can no longer be identified. Lastly, the black arrows in Figure A3.1c show the presence of the 2-level jumping discussed in

the main text of Chapter 5 in which the MnSi NW device appears to switch to a higher resistance state for a short period of time, and then switches back to the lower resistance state. This effect was found to occur at all temperatures, and across the entire field range studied. We could find no correlation between this 2-level jumping phenomenon and the skyrmion lattice phase.

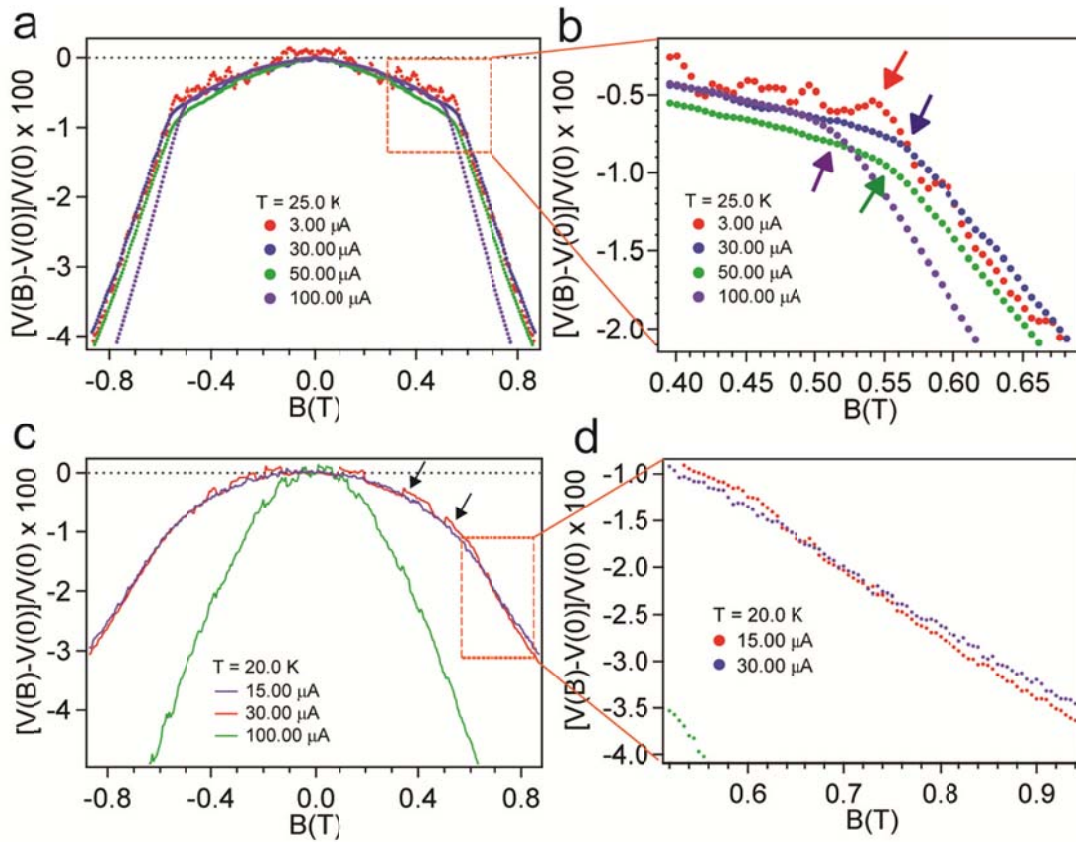


Figure A3.1. Effects of various values of applied DC current in MnSi NW devices. a) Symmetric magnetoresistance versus magnetic field at $T = 25.0$ K (temperature refers to thermometer of cryogenic system and not the actual device temperature) for a representative MnSi NW device obtained by sweeping the magnetic field continuously for several different applied currents. b) Zoom-in view of panel (a) with the shifting position of H_c highlighted by the colored arrows for several different applied currents. c) An additional example of the Joule heating effect in which the device temperature appears to have been locally heated beyond T_c for a 100 μA DC current, and H_c cannot be identified. The black arrows indicate the presence of 2-level jumping that necessitated the data filtering method discussed in the main text of Chapter 5. d) Zoom-in region of panel (c) showing the different slopes of the magnetoresistance at high field due to the different applied DC current.

A3.2 Additional MnSi NW Device showing Topological Hall Signal Anomaly

In Figure A3.2 we show an additional MnSi NW device in which the topological Hall resistivity signal has been extracted. This MnSi NW device was measured by continuously sweeping the magnetic field, and no filtering or data averaging method was implemented to eliminate the 2-level jumping from the raw data, and therefore, some data points have been omitted from the plot of topological Hall resistivity versus magnetic field (where the device jumps to the higher resistance state). The dimensions of this MnSi NW device were 215 nm wide by 145 nm thick, and was measured with a DC current of 25 μA , corresponding to a current density of $j = 8.2 \times 10^8 \text{ A/m}^2$. This device also shows the clear presence of hysteresis associated with entrance into and out of the skyrmion phase depending on the magnetic field sweep direction (indicated by blue and red arrows in Figure A3.2).

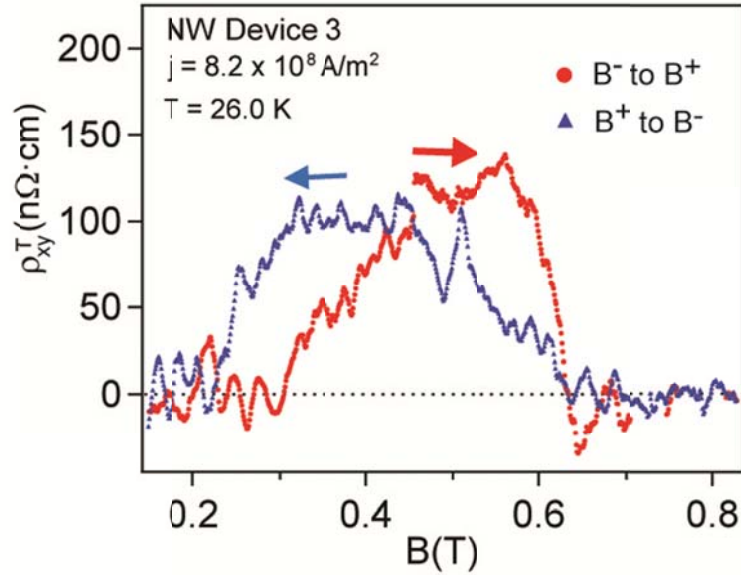


Figure A3.2. Topological Hall resistivity extracted for MnSi NW Device 3 at $T = 26.0 \text{ K}$, in which the field was swept continuously. Red and blue arrows indicate the direction in which the magnetic field was swept. The magnetic field was scanned at a rate of 20 Oe/s , and the applied DC current was $25.0 \mu\text{A}$. The magnetic field sweep direction is associated with hysteresis upon entering the skyrmion phase region which occurs roughly between 0.21 and 0.62 T for this MnSi NW device.